3-16-2017 12:00 AM

Advanced signal processing methods for plane-wave color Doppler ultrasound imaging

Omar Mansour, *The University of Western Ontario*

Supervisor: James C. Lacefield, *The University of Western Ontario*
A thesis submitted in partial fulfillment of the requirements for the Doctor of Philosophy degree
in Electrical and Computer Engineering
© Omar Mansour 2017

Abstract

Conventional medical ultrasound imaging uses focused beams to scan the imaging scene line-by-line, but recently however, plane-wave imaging, in which plane-waves are used to illuminate the entire imaging scene, has been gaining popularity due its ability to achieve high frame rates, thus allowing the capture of fast dynamic events and producing continuous Doppler data. In most implementations, multiple low-resolution images from different plane wave tilt angles are coherently averaged (compounded) to form a single high-resolution image, albeit with the undesirable side effect of reducing the frame rate, and attenuating signals with high Doppler shifts.

This thesis introduces a spread-spectrum color Doppler imaging method that produces high-resolution images without the use of frame compounding, thereby eliminating the tradeoff between beam quality, frame rate and the unaliased Doppler frequency limit. The method uses a Doppler ensemble formed of a long random sequence of transmit tilt angles that randomize the phase of out-of-cell (clutter) echoes, thereby spreading the clutter power in the Doppler spectrum without compounding, while keeping the spectrum of in-cell echoes intact.

The spread-spectrum method adequately suppresses out-of-cell blood echoes to achieve high spatial resolution, but spread-spectrum suppression is not adequate for wall clutter which may be 60 dB above blood echoes. We thus implemented a clutter filter that re-arranges the ensemble samples such that they follow a linear tilt angle order, thereby compacting the clutter spectrum and spreading that of the blood Doppler signal, and allowing clutter suppression with frequency domain filters. We later improved this filter with a redesign of the random sweep plan such that each tilt angle is repeated multiple times, allowing, after ensemble re-arrangement, the use of comb filters for improved clutter suppression.

Experiments performed using a carotid artery phantom with constant flow demonstrate that the spread-spectrum method more accurately measures the parabolic flow profile of the vessel and outperforms conventional plane-wave Doppler in both contrast resolution and estimation of high flow velocities.

To improve velocity estimation in pulsatile flow, we developed a method that uses the chirped Fourier transform to reduce stationarity broadening during the high acceleration phase of pulsatile flow waveforms. Experimental results showed lower standard deviations compared to conventional intensity-weighted-moving-average methods.

The methods in this thesis are expected to be valuable for Doppler applications that require measurement of high velocities at high frame rates, with high spatial resolution.

Keywords

Beamforming, blood flow, compounding, Doppler, high-frame-rate, plane-wave, spread-spectrum, ultrafast, ultrasound.

Co-Authorship Statement (where applicable)

Chapter 2 was published in IEEE Transactions in Ultrasonics, Ferroelectrics, and Frequency Control as: O. Mansour, T. L. Poepping and J. C. Lacefield, "Spread-Spectrum Beamforming and Clutter Filtering for Plane-Wave Color Doppler Imaging," *IEEE Transactions on Ultrasonics, Ferroelectrics, and Frequency Control,* vol. 63, no. 11, pp. 1865 - 1877, 2016. I developed the theory of the spread-spectrum method where for the first time, a random sequence of transmit angles is proposed to spread the clutter spectrum in Doppler ultrasound imaging. Additionally I proposed and justified the reshuffling clutter filter, designed the experimental validation methodology, and performed the experiments. I developed the custom C++ software that ran on the ultrasound scanner, and the matlab code that performed the processing of the acquired data and implemented the method. I have also performed the statistical analysis, interpreted the results, and wrote the manuscript. These activities were performed under the supervision of J. C. Lacefield. T. L. Poepping and J. C. Lacefield contributed to the review of the final manuscript.

Chapter 3 is in preparation for publication in IEEE Transactions in Ultrasonics, Ferroelectrics, and Frequency Control. I developed and justified the concept of using a segmented random sweep and comb filters for improving clutter suppression of the spread-spectrum method. I also developed the experimental validation methodology, and performed the experiments. I developed the custom C++ software that ran on the ultrasound scanner, and the matlab code that performed the processing of the acquired data and implemented the method. I have also performed the statistical analysis, interpreted the results, and wrote the manuscript. These activities were performed under the supervision of J. C. Lacefield, who also contributed to the review of the manuscript.

Chapter 4 is in early preparation for publication in IEEE Transactions in Ultrasonics, Ferroelectrics, and Frequency Control. I developed and justified the concept of using the chirped Fourier transform and the method of matching pursuits to reduce the spectral bandwidth and thus the variance of estimated velocities in non-stationary blood flow.I also developed the experimental validation methodology, and performed the experiments. I developed the custom C++ software that ran on the ultrasound scanner, and the matlab code

that performed the processing of the acquired data and implemented the method. I have also performed the statistical analysis, interpreted the results, and wrote the manuscript. These activities were performed under the supervision of J. C. Lacefield, who also contributed to the review of the manuscript.

Table of Contents

List of Tables (where applicable)

List of Figures (where applicable)

List of Symbols

μ   mean value

σ standard deviation

θ angle between ultrasound transducer's axis and flow direction

c average speed of sound in soft tissue (chapters 1,2 and 3) or chirp-rate (ch. 4)

f_0 ultrasound excitation frequency

List of Acronyms & Abbreviations

BMF   blood mimicking fluid

CSR   clutter-to-signal ratio

CFT   chirped Fourier transform

dB   decibels

DFT   discrete Fourier transform

FIR   finite impulse response

FT   Fourier transform

FFT   fast Fourier transform

HRI   high resolution image

Hz   hertz

I/Q   in-phase and quadrature modulated data samples

IIR   infinite impulse response

LRI   low resolution image

PRCF   periodic reshuffling clutter filter

PNR   peak-to-noise-ratio $= 20\log(\frac{fft\ peak\ value}{fft\ median\ value})$

PRF   pulse repetition frequency

PRI   pulse repetition interval

RCF   reshuffling clutter filter

RF   radio frequency

SNR   signal-to-noise ratio

TMM   tissue mimicking material

TPF   true positive fraction

Chapter 1

1   Introduction

1.1   Conventional ultrasound imaging

Ultrasound is a medical imaging modality in which an acoustic wave is transmitted towards the region of interest and the received echo is used in constructing an image that highlights the structure of the imaged scene [1]. Pulse-echo ultrasound relies on echo reflections that occur due to impedance mismatches encountered by the sound waves when crossing a region boundary, or due to scattering when the waves encounter inhomogeneity in the acoustic impedance such as the case when imaging sub-resolution scatterers whose dimensions are much smaller than the wavelength of the ultrasound pulses (e.g. red blood cells). The amplitude of scattered echo thus gives an indication of the density of red blood cells, while the time it takes for the echo to reach the transmission source (*i.e.*, the transducer) indicates the axial distance of scatterers from the transducer surface. In clinical ultrasound, the excitation frequency typically ranges from 2 to 12 MHz.

When ultrasound waves encounter a moving scatterer, echoes are received at a frequency that is offset from the transmitted frequency due to the Doppler effect. If an ultrasound pulse is transmitted with a frequency f_0 and encounters a scatterer whose velocity is v, then the received echo shall have a frequency that is offset from f_0 by [1]:

$$f_D = \frac{2vf_0\cos(\theta)}{c} \tag{1.1}$$

where θ is the angle between the direction of motion and the ultrasound beam and c is the speed of sound.
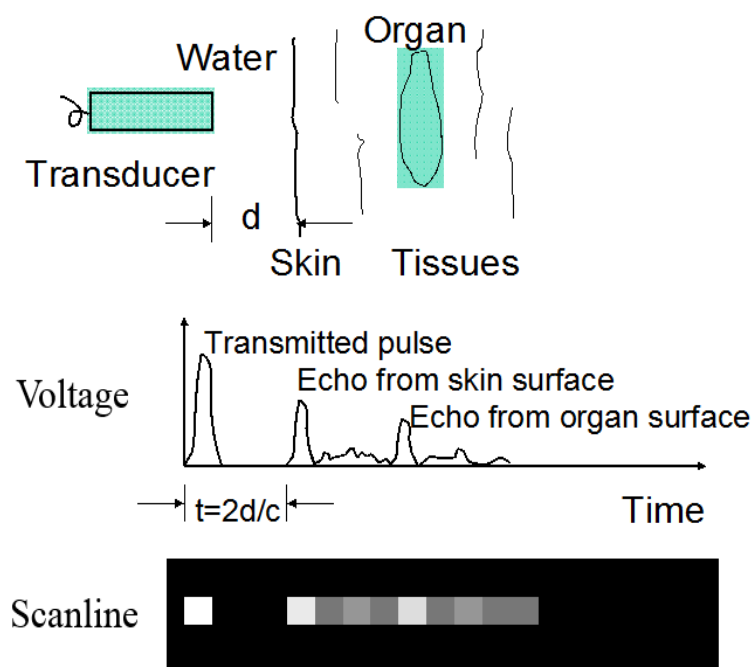
Figure 1.1: Formation of a B-mode scanline.

In pulsed wave (PW) ultrasound, the same transducer is used for transmission and reception and it may be a mechanically scanned single element, or an electronically scanned transducer array with multiple elements. The construction of an ultrasound image is dependent on the mode of operation. In two-dimensional B-mode imaging, each pulse emitted by the transducer transmits a focused beam to illuminate a narrow region of the imaging scene. Focusing is also used in reception to accept echoes from a similarly narrow region and the received echoes are converted to an electrical signal as shown in Figure 1.1. The echo's time delay indicates the depth or axial distance from the transducer, and its amplitude indicates the density of scatterers. The voltage signal is then converted into a scanline where amplitudes are mapped to gray levels and time is quantized to represents the pixel's depth. The full B-mode image is formed of multiple scanlines that cover the entire imaging scene. B-mode images are typically displayed such that the scanlines are oriented vertically as opposed to horizontally as shown in Figure 1.1, where the image is displayed as multiple adjacent vertically oriented scanlines.

Scanning may be performed mechanically as in single element transducers, or electronically as in array transducers. In linear arrays, the element centers are separated by a distance (pitch) that is roughly equal to the wavelength (λ). For each scanline, only a subset of the elements is used for producing a focused narrow beam, and that subset is then shifted by one element to produce the next scanline, till the end of the array is reached and the entire rectangular shaped B-mode image is produced. Phased arrays typically use fewer elements, with a pitch of $\lambda/2$, and all elements are used in every transmit and receive, but instead of scanning right and left as in linear arrays, scanning is done by electronically changing the tilt angle of the narrow beams, thus producing cone shaped B-mode images. In either case, transmit focusing is achieved by delaying the pulses emitted from each of the array elements such that they reach the focus at the same time, and in a reciprocal manner the received samples are delayed such that echoes from a scatterer at the focus reaches all elements at the same time. Once the transmit event has taken place, it is not possible to separate the signals arising from each of the transmitting elements and thus their relative transmit delays can only produce one transmit focal point, and a different transmit event is needed for obtaining a new focal point. Unlike in transmission however, each element has a separate received signal and thus the relative receive delays may be retrospectively adjusted to produce multiple receive focal points per transmit event, thus implementing dynamic receive focus for every pixel on the scanline.
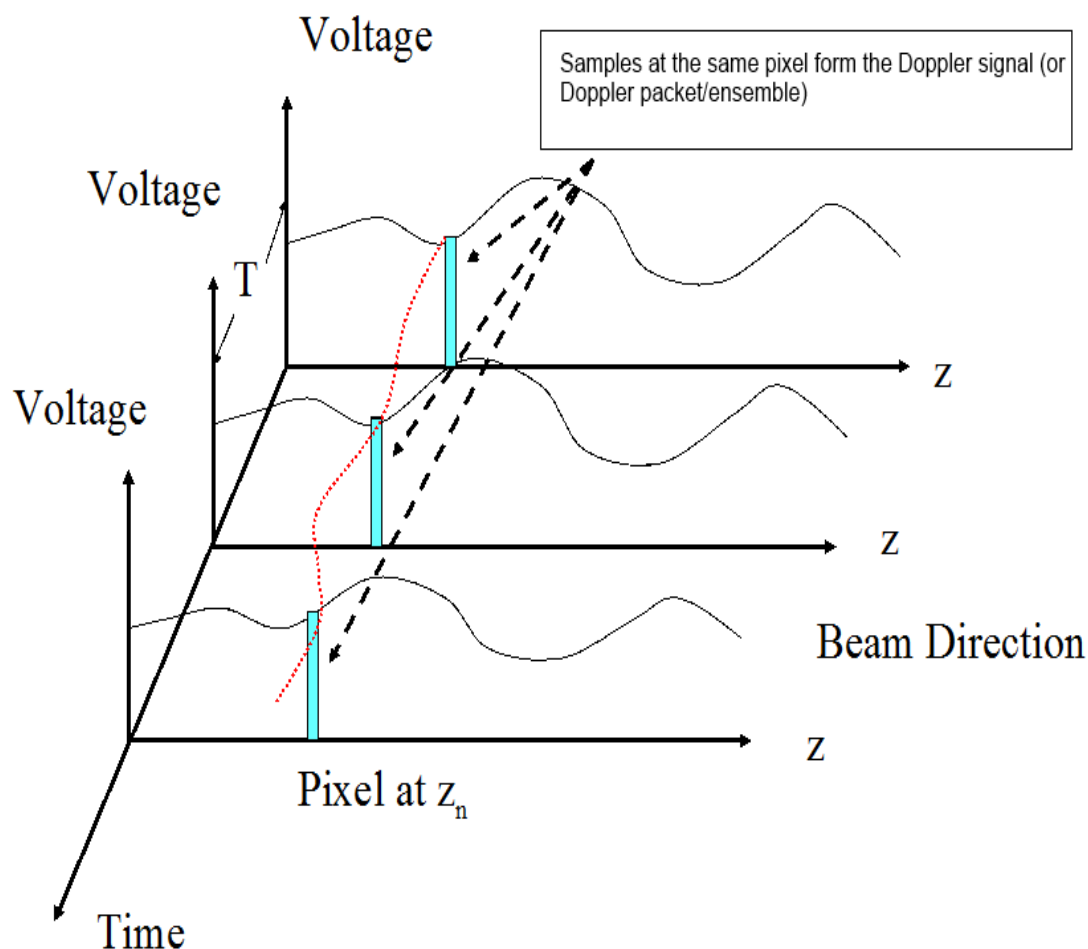
Figure 1.2: Formation of a Doppler ensemble.

In color Doppler flow imaging, the Doppler frequency is used to estimate the blood velocity based on Eq. (1.1), and may be estimated by repeating each scanline multiple times in a short period of time as demonstrated in Figure 1.2, where each ultrasound pulse emitted in a scanline produces a beamformed RF signal that is a function of time (fast-time or z-axis in Figure 1.2) and the succession of transmitted pulses forms a two-dimensional signal in fast-time (z-axis) and slow-time ('Time' axis). If quadrature demodulation is then performed, in-phase (I) and quadrature (Q) data samples are thus produced, and an ensemble of such samples corresponding to the same depth or fast-time forms the Doppler ensemble that is used for estimating Doppler frequency shifts. Since each scanline is the result of a single transmit pulse, the pulse repetition frequency (*PRF*), which is also the sampling frequency for the Doppler signal, must be at least twice the

maximum Doppler frequency shift expected within a pixel to avoid aliasing in accordance with the Nyquist criteria. Similarly, the Doppler ensemble must be long enough to achieve reasonable frequency resolution. After a high-pass filter is applied to the I/Q samples that form the Doppler ensemble (or the slow time signal), each pixel's velocity estimate is then quantized and converted into a color shade, with positive velocities represented in shades of red and negative velocities in shades of blue. In color Doppler imaging, pixels holding non-zero velocity information are overlaid over B-mode images.

Power Doppler images are formed in the same manner as in color Doppler flow, except that after applying the high-pass filter, each pixel's power (squared magnitude) is computed as the sum of the squared amplitudes of its Doppler samples, and displayed instead of mean velocity estimates. The high-pass filter is essential for removing echoes from stationary scatterers such as vessel wall or tissue, and is hence commonly referred to as the clutter or wall filter. Without proper clutter filtering, blood velocity and power may not be accurately estimated.

A drawback in conventional focused-beam imaging is that only one transmit focal point per firing or scanline can be achieved, since it is not possible to readjust the transmit timing delays of the array elements retrospectively. With a single focus, the image quality varies depending on the depth, and the user has to manually adjust the focus to obtain the best image quality at the desired region of interest.

One shortcoming in conventional Doppler imaging is the need to repeat each scanline multiple times before moving to the next one, in order to form a slow-time Doppler signal where the phase progression and thus the Doppler frequency shift can be measured, thereby increasing the total amount of time needed to produce one Doppler image and reducing the frame rate. Another drawback is that the slow time signals are acquired in bursts of samples since each scanline is repeated multiple times (to form its Doppler ensembles) but is then followed by an idle period where other scanlines are being acquired. The emission of transmit pulses in bursts and irregular slow-time sampling

makes the clutter filter design more complex since it has to operate only on one ensemble at a time, with data lengths that are typically 8-16 samples [2].

1.2   High-frame-rate Doppler ultrasound imaging

High-frame-rate imaging has been a focus of significant research in the past few years and is desirable for its ability to address some of the shortcomings of focused-transmit-beam imaging that were discussed in the previous section. That includes the ability to produce high frame rates that enable acquisition of fast dynamic events, the availability of continuous Doppler slow time samples that enable better clutter filtering and signal processing, and the ability to implement dynamic transmit focusing thereby improving the image quality due to higher spatial resolution and signal-to-noise ratio (SNR).
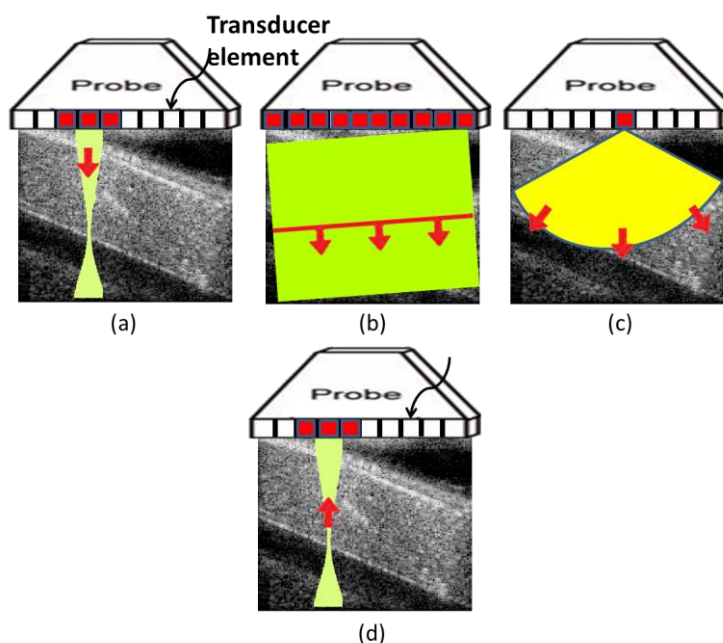
Fig. 1.3: (a) conventional narrow-beam transmission, (b) plane-wave transmission, (c) divergent-beam transmission for synthetic aperture and (d) narrow-beam reception used for all 3 methods. In each panel, the array elements highlighted in red are used to produce the transmit beam.

High-frame-rate imaging may be realized by using synthetic aperture methods, where diverging beams, whose wave-front travels cylindrically in 2D as shown in Fig. 1.3c, are transmitted. Multiple narrow beams are used simultaneously for reception, as shown in

Fig. 1.3d, to produce a single low resolution image frame. If every transmission event uses a different array element, and multiple low resolution frames corresponding to the different array elements are coherently compounded (i.e. summed), a higher resolution image is formed [3]. Alternatively, high-frame rate may be realized by transmitting plane-waves whose wave-front travels in a straight line in 2D as demonstrated in Fig. 1.3b. Multiple narrow beams are used simultaneously for reception, as shown in Fig. 1.3d, to produce a single low resolution image frame. If each transmission event uses a different plane-wave tilt angle, and multiple low resolution frames corresponding to the different tilt angels are coherently compounded, a higher resolution image is formed [4].

As compared to conventional narrow-beam transmissions, in which an image is formed line-by-line (Fig. 1.3a), diverging and plane-waves can produce an image for every transmit event, albeit at a lower resolution, and thus compounding is needed to increase the image resolution, and hence a compromise exists between frame-rate and image resolution.

Although many of the methods proposed in the next few chapters are applicable to both high-frame-rate implementations, the main focus of this thesis is plane-wave imaging.
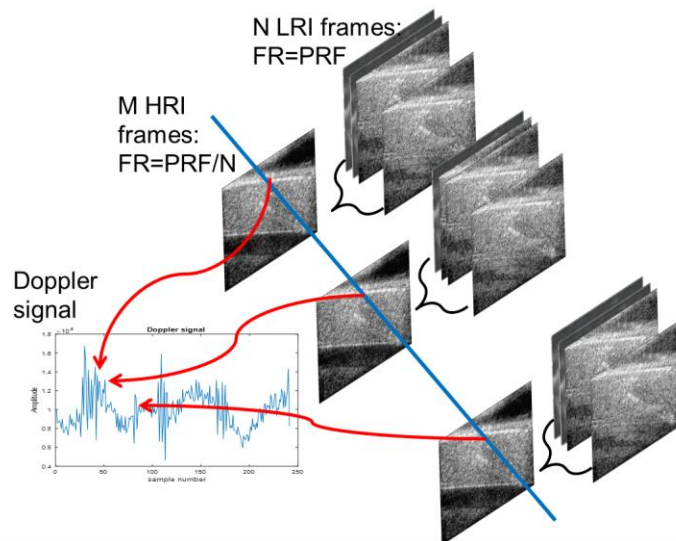
Figure 1.4: Construction of a high resolution image and a Doppler ensemble.

1.2.1 Plane-wave imaging

The first experimental ultrasound plane-wave imaging system was reported in 1979 by Delannoy *et al.* [5], where analog electronics were used. In this system, a single acoustic pulse is emitted to illuminate the 2D imaging scene, and only 20 receive channels were used due to hardware limitations, resulting in large array pitch and thus grating lobes in the receive beamformer. The scanner was capable of reaching a frame rate of 1000 images per second however. In 1984, Von Ramm and his group at Duke University used a wide acoustic transmit beam that enabled the simultaneous acquisition of four narrow receive beams per transmit pulse [6], thus increasing the frame-rate by a factor of 4. This approach was called "explososcan", and the proof of concept was validated *in vivo*. They envisioned that this method may be extended such that a single transmit pulse fully illuminates the entire 2D imaging scene, enabling simultaneous acquisition and processing of the entire set of possible receive beams, thus setting the stage for plane-wave imaging.

In 1997, Jian-yu Lu from the University of Toledo (Toledo, OH) has successfully used plane-wave imaging to achieve a frame-rate of 3750 frames per second [7], whereas in 1999, Fink and co-authors [8] were able to reach 5000 frames per second using plane-waves for the purpose of imaging the transient propagation of shear mechanical waves in human tissue in real-time.

In 2006, Jian-yu Lu's group proposed, for the first time [9], the use of plane-wave transmit pulses from multiple steering angles where each transmit pulse is used to illuminate the entire imaging scene while simultaneously receiving from all transducer elements, thus allowing dynamic receive focusing to produce a low resolution image (LRI) as demonstrated in Fig. 1.3b. Multiple LRI frames are acquired using a sequence of tilt angles at a frame rate equals to the PRF and coherent compounding (i.e. averaging) of N LRI frames is then performed to produce high resolution images (HRI) with a frame rate of *PRF/N* as shown in Figure 1.4. The resulting HRI frames have SNRs and resolution that are higher than the original LRI frames. In 2009, Fink's group was able to utilize the same method to improve the spatial resolution for transient elastography [4]
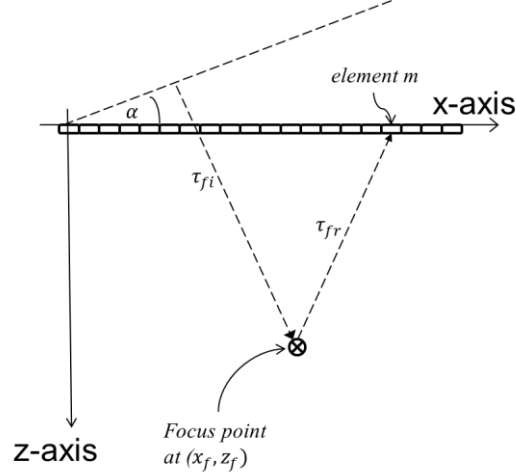
Figure 1.5: Delay alignments prior to compounding.

The reason behind the improved beam profile and SNR is that, unlike in conventional narrow-beam imaging, which is only capable of a single transmit focal point per scanline and requires firing the scanline multiple times if multiple transmit foci are needed, Plane-wave imaging is capable of synthesizing multiple transmit focal points retrospectively [4]. Synthetic transmit focus at a point (x_f, z_f) shown in Figure 1.5, is implemented by ensuring that echoes from a scatterer located at that point exhibit the same delay and are thus coherently summed despite being insonated from different tilt angles. This is achieved by extracting and summing samples received at an array element m that correspond to time delay:

$$\tau = \tau_{fi} + \tau_{fr} = \frac{z_f cos\alpha + x_f sin\alpha}{c} + \frac{\sqrt{(x_f - md)^2 + z_f^2}}{c} \qquad (1.2)$$

where τ_{fi} is the transit time for the incident pressure wave to reach the focal point at (x_f, z_f) as shown in Figure 1.5, τ_{fr} is the transit time for the scattered wave to reach the transducer element m, c is the speed of sound, α is the tilt angle, $x_f = ld$, d is the array's element pitch, l is the scanline, $l = 0$ denotes the leftmost scan line, and placing the summation at location (x_f, z_f) of the resulting image. Repeating the process for all the pixels yields the compounded image.
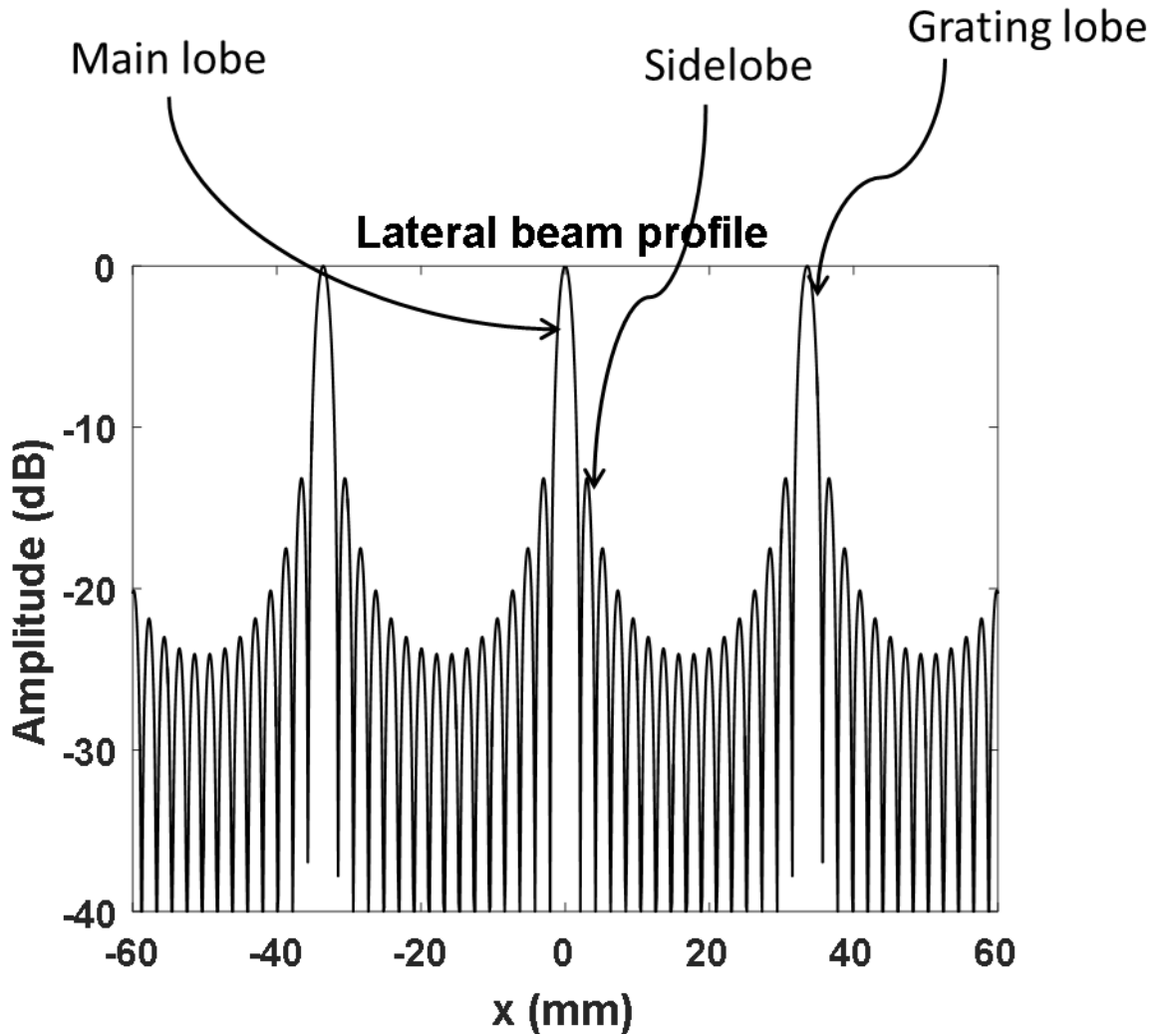
Figure 1.6: Compounded lateral (x-direction) transmit beam profile demonstrating the existence of grating lobes when the transmit angle increment is too small.

Figure 1.6 shows a synthetic transmit beam profile (after compounding) demonstrating the sidelobes, and the existence of grating lobes, i.e. the repetition of the beam pattern multiple times, when the transmit angle increment is smaller than a certain limit. This is somewhat analogous to electronic signal aliasing due to under-sampling, which has been pointed out by Denari *et al.* [10]. The minimum transmit angle increment to avoid grating lobes has been discussed by Denari *et al.* as well as by us in section 2.2.3, where we have reproduced similar results.

Because signals for different transmit angles are separable and can be delayed and summed (or compounded) retrospectively, compounded plane-wave imaging enables retrospective transmit and receive beamforming that significantly improves resolution for stationary scatterers, but it represents a process of low-pass filtering in which the compounded echoes from fast-moving objects are attenuated. Ekroll *et al*. [10] have shown the attenuating effect of this filtering on high-velocity scatterers and the resulting bias on velocity estimates. An additional drawback of compounding is that the HRI frame rate is reduced to *PRF/N*, thereby reducing the (slow-time) Nyquist frequency limit, so frequency aliasing can also occur for high velocity scatterers. Compounding is nevertheless necessary to improve the beam profile of the LRI frames in order to suppress off-focus or out-of-cell echoes and produce high-resolution frames. If the total transmit angle swing is α_{swing}, then the angle increment is α_{swing}/N. Increasing *N* reduces the angle increment, thereby improving the beam profile, but it reduces the slow-time sampling rate and hence the unaliased Doppler frequency limit. Hence, a tradeoff exists between the unaliased Doppler limit and the beam resolution (i.e. width of its mainlobe and/or height of its sidelobes).

1.2.2   Synthetic transmit aperture imaging

Synthetic aperture techniques were originally conceived for radar systems in the 1950s and have made significant advances in the late 1980s [11]. In radar systems, synthetic aperture employs a single transmitter-receiver pair is employed at a time, and the aperture is synthesized by moving the antenna over the region of interest in an airplane or satellite. In medical ultrasound however, the array has a fixed number of elements and is usually stationary, and synthetic aperture is performed by acquiring data from all transmit-receive combinations to achieve both transmit and receive focusing at any desired location within the image grid. In 1992, the first direct attempt to implement synthetic aperture for medical ultrasound was described by O'Donnell and Thomas [12] and was intended for intravascular imaging using a circular transducer array. The application of multi-element sub-apertures to increase the SNR of synthetic aperture imaging has been investigated by Karaman *et al*. [13] and by Lockwood *et al*. [14]. In all cases, the multi-element sub-aperture was used to emulate the radiation pattern of the single element transmission

(thus creating a virtual source) by applying de-focusing delays in such a way that a spherical wave with limited angular extend was produced.

In similarity to plane-wave imaging, synthetic aperture improves the spatial resolution and contrast by compounding frames from multiple emissions, where each emission has been emitted from a unique transducer element or virtual source (Fig. 1.3c).

For each point p on the image grid, samples from a transmit element i and receive element j that correspond to delay time $\tau_{i,j}$ are summed coherently, such that:

$$\tau_{i,j} = \frac{|r_p - r_e(i)| + |r_p - r_r(j)|}{c} \qquad (1.3)$$

where r_p denotes the point in the image grid where focusing is performed upon, r_e denotes the transmit element's position, r_r denotes the receive element's position, and c denotes the speed of sound.

Because signals from the different transmit elements are separable and can be delayed and summed retrospectively, synthetic aperture enables retrospective transmit and receive beamforming that significantly improves resolution for stationary scatterers, but it represents a process of low-pass filtering in which the compounded echoes from fast-moving objects are attenuated, and hence suffers from the same limitations described for plane-wave imaging.

For further details on synthetic aperture imaging, we shall refer the reader to the excellent review paper published by Jensen *et al.* [3].

1.3 Doppler signal processing for compounded plane-wave imaging
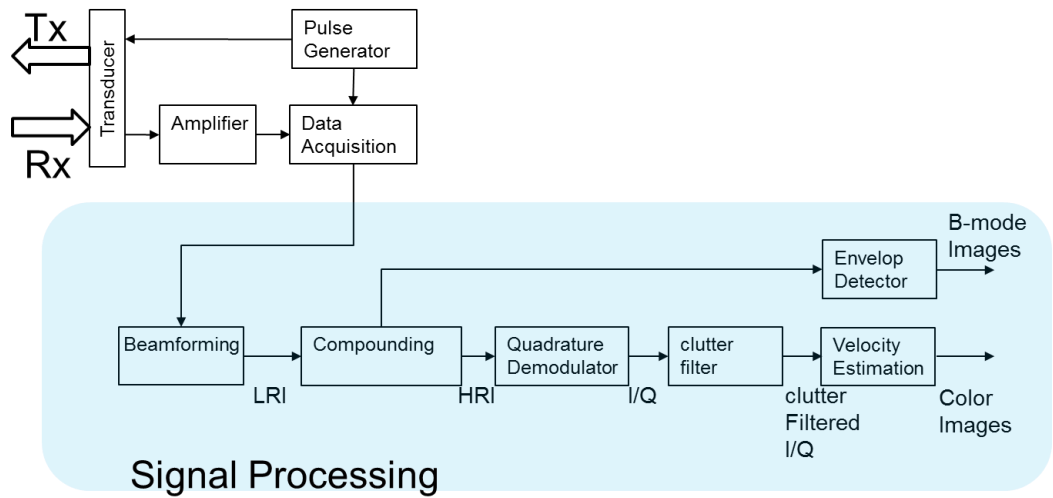
Figure 1.7: Signal processing chain.

Figure 1.7 shows a block diagram representing the Doppler signal processing chain that describes compounded plane-wave imaging used throughout this manuscript (in light blue). Below are descriptions for the individual processing blocks.

1.3.1 The pulse generator

The pulse generator provides voltage pulses to each element of the transducer array. If the tilt angle is zero, then all elements fire at the same time, otherwise each element fires a delayed version of the pulse used by its adjacent neighbor. The delay magnitude and sign depend on the plane-wave tilt angle programmed.

1.3.2 The amplifier and data acquisition module

The pulse generator also controls the amplifier and data acquisition modules such that acquisition starts at some pre-determined time delay from the transmit pulse emitted. The time offset is to avoid the initial large acoustic signals received by the transducer at the time of firing the transmit pulses and may saturate or damage the amplifier prior to analog-to-digital conversion. This control is achieved via a Transmit-Receive switch [1].

Typically, the tilt angle used for each transmit pulse is swept linearly till the full range is spanned, and this process repeats till the end of data acquisition.

1.3.3   The beamformer

Complete RF frames are thus acquired and provided to the beamformer in multiple channels, one channel per transducer element, and each channel contains an RF signal sampled at a rate that is at least twice as high as the transducer's or RF signal's bandwidth. An RF frame is produced for every transmit pulse with a tilt angle α, hence the RF frame rate is equal to *PRF*, and the time length of each channel's signal is <*1/PRF*. At each point (x_f, z_f), receive beamforming is achieved by summing samples from all the channels defining the receive aperture and correspond to time τ defined in Eq. (1.2), where each channel (or element) *m* is part of the receive aperture. Beamforming produces LRIs at a frame rate of *PRF*.

1.3.4   Compounding and I/Q demodulation

Compounding multiple LRI frames spanning the tilt angle sweep of length *N* produces HRI frames with the reduced frame rate of *PRF/N* [15]. Compounding improves the image resolution, but reduces the frame-rate. It should be noted that compounding is performed on the RF data, and is thus coherent since it uses both magnitude and phase. This is in contrast to non-coherent compounding (not used and not shown in Figure 1.7) which is performed on the amplitude of the RF and does not improve the image resolution, but rather reduces the speckle pattern that often appears on b-mode images.

I/Q frames are produced by quadrature demodulating the HRI frames using the transmitted excitation frequency. The in-phase data is applied by multiplying the RF signal by $\cos(2\pi f_0 t)$, where f_0 is the emission frequency, and t is time, followed by low-pass filtering to keep the baseband signal. Similarly, the quadrature data is obtained by multiplying the RF signal by $\sin(2\pi f_0 t)$ followed by low-pass filtering.

1.3.5   Clutter filtering

Using multiple I/Q frames, each pixel forms a slow-time Doppler signal, to which a clutter filter is applied. The clutter filter is required for suppressing wall or tissue echoes

which may reach 60 dB above blood signal levels [16] and is essential to reduce bias in mean velocity estimation [17], [18]. There exists a multitude of clutter filters developed for conventional focused-beam Doppler imaging that operate on a limited Doppler ensemble length. For plane-wave imaging, in addition to finite impulse response and infinite impulse response filters which operate on continuous slow-time data, a filter based on singular value decomposition has been proposed in [19].

1.3.6   Velocity estimation

Color flow Doppler images are formed by estimating the mean velocity at each pixel using wall filtered ensembles [15]. The commonly used method of intensity-weighted mean frequency (IWMF) [20] uses short Doppler ensembles representing 2-60 mS time windows that slide in an overlapping manner to provide high update rates. Frequency is then converted into estimated velocity using eq. (1.1).

Due to the complex nature of ultrasound scattering, ultrasound signals and their corresponding Fourier transforms, which is used in estimating mean velocities, may be modeled as stochastic. Artefacts that increase the spectral bandwidth, such as windowing, intrinsic, and non-stationarity (wide-sense) broadenings [21] may thus increase the variance of the estimated mean frequency [20], [22]. Short Doppler ensembles provides high temporal resolution, but may result in higher broadening, and lower signal-to-noise ratio (SNR), whereas long ensembles provide less broadening (and hence less variance) and higher SNR at the expense temporal resolution.

To reduce the effect of short data windows on spectral broadening, parametric spectral estimation methods such as the auto-regressive model [23], and the maximum likelihood (ML) or Capon estimator have been studied by various authors and reviewed by [24] and [25], but were found to have serious issues with the model order selection [26], [27]. Several authors have worked on reducing non-stationarity broadening; an adaptive autoregressive model was proposed in [28], while a Kalman filter in conjunction with ML estimator was suggested in [29], whereas a stationarizing technique was presented in [30].

It must be noted that despite that Doppler estimation method being very commonly used in clinical setups [31], it suffers from some limitations such as aliasing and flow angle dependency. Evans and Jensen have published a good review that surveys multiple velocity estimation methods [31] such as vector Doppler, in which multiple ultrasound beams are used to mitigate the beam-to-flow angle dependency, and the synthetic aperture approach proposed by Jensen's group [32] which takes advantage of synthetic aperture to produce beams from multiple directions, followed by the application of two-dimensional cross-correlations on the RF data to properly estimate vector flow information.

1.3.7   Envelope detection

For Duplex scanning, B-mode images are formed using the Hilbert transform [1], which extracts the amplitude of compounded RF samples in the HRI frames. Log-compressed values [1] are then displayed on the screen, and finally, the Color Doppler images overlaid on top of the B-mode images.

1.4   Ultrasound flow-phantom experiments

Experimental validation of Doppler imaging performance may be performed by using flow phantom studies. Figure 1.8 demonstrates a typical setup for such a measurement, in which a precision computer-controlled flow pump (e.g. [33]) is needed to push blood-mimicking fluid (BMF) (e.g. [34]) through a phantom that mimics blood vessels and the surrounding tissue (e.g. [35] [36]). The phantom needs to give realistic representation of the human vessel or organ that the method or system is designed to image.
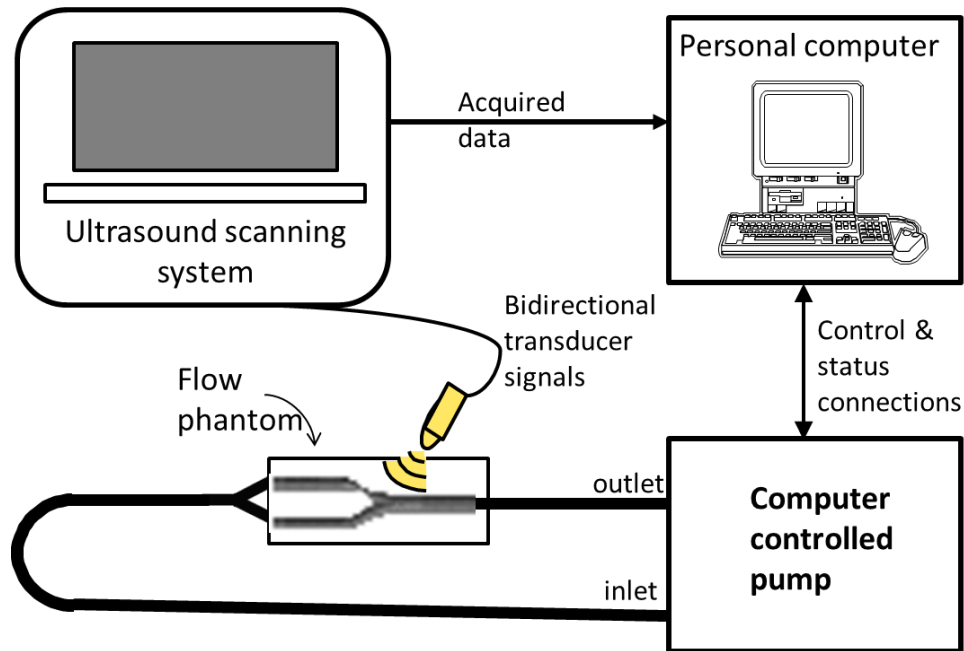
Figure 1.8: Schematic of an *in vitro* Doppler ultrasound system.

It is generally important that the physical and acoustical parameters of the tissue-mimicking material follow the guidelines for a standard flow phantom set forth by the International Electrotechnical Commission (IEC) [37]. The IEC standard specifies a tissue-mimicking material with a density of 1040 ± 100 kg/m^3, a sound speed of 1540 ± 15 m/s, and an attenuation of 0.5 ± 0.05 dB/(cm·MHz). The tissue-mimicking material (TMM) is typically composed of either an agar or gelatin base with particles added to produce scattering of the ultrasound beam.
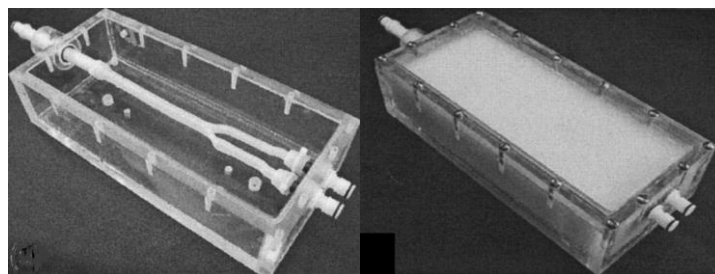
Figure 1.9: (Left) Flow phantom without tissue mimicking material, (right) flow phantom with tissue mimicking material.

A number of flow phantoms have been developed that mimic vessels comparable to those present in the human body. Figure 1.9 shows a carotid flow phantom [36] emulating the

carotid artery and bifurcation with (right) the tissue mimicking material, and without (left) to illustrate the shape of the vessel. The common carotid segment consisted of an 8-mm inner diameter and a 1-mm thick polydimethylsiloxane vessel wall surrounded by tissue-mimicking material [38]. These flow phantoms are typically capable of emulating flow rates in excess of 10 mL/s.

Wall-less flow phantoms, in which the BMF is in direct contact with the TMM, have been described in [38]. Wall-less flow phantoms were proposed to avoid distortion problems arising from the ultrasound beam propagation through the tube wall (Rickey *et al.* [39]). However, it is necessary to have a good seal between the inlet and outlet tubes and the TMM channel to prevent BMF leakage. Rickey *et al.* described a vessel seal using two cylindrical end-pieces fixed to the walls and centered over the inlet and outlet tubes. In practice, the construction is not sufficient to prevent fluid leakage because there is insufficient adhesion between the TMM and the wall. Thus, only very low flow rates can be used before leakage of the BMF out of the channel. In addition, fragility of some agar-based TMMs limits the flow rates that can be used before the TMM cracks or breaks up.

A range of different tubing materials, such as Teflon, latex, or polyvinyl alcohol may be used to mimic the blood vessel, and it may either remain inside the tissue-mimicking material or be withdrawn from the tissue-mimicking material to create a wall-less vessel cavity [39].

The Doppler signal is produced by the motion of red blood cells, so it is important that the properties of the blood-mimicking fluid precisely match the viscous and acoustic properties of blood. The properties of the blood-mimicking fluid should follow the guidelines set forth by the IEC standard [37], which specifies a density of 1050 ± 100 kg/m3, a sound speed of 1570 ± 30 m/s, an attenuation of < 0.1 dB/(cm· MHz), and a viscosity of 4 ± 0.4 mPa· s. Furthermore, the blood-mimicking fluid must contain scatterers that are comparable in diameter to red blood cells, 7.5 μm [1], and it is important that these particles be neutrally buoyant within the blood-mimicking fluid. A well-characterized and widely used blood-mimicking fluid that closely matches the IEC

standard has been developed in [34]. This blood-mimicking fluid uses 5-µm diameter nylon particles to simulate the presence of red blood cells.

A precision flow pump is required if the accuracy of the velocity estimation method or system needs to be characterized. Additionally, to test the performance in non-stationary flow conditions, the pump needs to allow programmable pulsatile flow profiles. One such pump is Compuflow1000 precision pump (Shelley Medical Imaging Technologies, London, ON) which was initially proposed in [33].

1.5 Hypothesis and objectives

The overall hypothesis of this thesis is that in plane-wave color Doppler imaging, the currently existing compromise between spatial resolution and the unaliased Doppler limit may be circumvented by using advanced signal processing methods in conjunction with a reorganization of the angle sweep sequence. The long-term objective is to produce color flow Doppler images with optimal spatial, temporal and frequency resolutions for cardiovascular imaging, thus enabling the formation of spectral Doppler data at every point within the image grid without compromising the spatial resolution.

Conventional narrow-beam line-by-line ultrasound scanners can either provide full quantitative Doppler information on a limited sample volume (spectral Doppler), or mean velocity estimates on a large region of interest (Doppler flow imaging) [1]. The proposed spread-spectrum method enables the acquisition of unaliased spectral Doppler data and mean velocity estimates at every point within the imaging scene with high spatial and temporal resolutions simultaneously, thus facilitating improved visualization and detection of flow abnormalities for all points within the image grid simultaneously. For detecting flow abnormalities such as turbulence, this translates to reduced exam time, user variability and errors, since the sonographer doesn't need to acquire multiple regions of interest. The detection of turbulence is particularly important as studies have shown that turbulent blood flow can lead to significant thrombus production [40], and when near a plaque surface may also result in plaque rupture, leading to stroke [41]. Early detection of stroke vulnerability by accurately measuring the turbulence intensity would be beneficial as it is the third major cause of death in industrialized nations [42].

The following specific hypotheses were set to investigate the main hypothesis:

1. Using a sequence of randomized plane-wave tilt angles (aka spread-spectrum sweep) provides high spatial resolution without the need for frame compounding, thereby increasing the maximum unaliased Doppler frequency to *PRF/2* instead of the traditional *PRF/2N* in compounded plane-wave imaging, where *N* is the number of compounded frames.

2. Using a segmented randomized plane-wave angle sweep plan significantly improves the clutter filter performance.

3. The signal-to-noise ratio and standard deviation of mean velocity estimates may be improved by using the chirped Fourier transform.

We conceived the basic concept behind the spread-spectrum method after observing that prior to frame compounding, demodulated slow-time I/Q signals of stationary scatterers outside a resolution cell (out-of-cell scatterers) follow a linear phase progression as a result of the linear transmit angle sweep, and thus appear as complex sinusoids in the time domain. Stationary scatterers from within the resolution cell however (in-cell scatterers) exhibit constant phase as the linear transmit angle sweep progresses due to the fact that transmit delays are adjusted (retrospectively albeit) to make echoes from multiple transmit angles within the sweep arrive at the same time and with equal phase at the resolution cell of interest. Coherent compounding is a summation process and may be viewed, in the context of signal processing, as a low pass filter that suppresses out-of-cell echoes to improve the image resolution. For Doppler imaging, compounding is necessary when using linear sweeps since otherwise out-of-cell scatterers appear as tones on the spectrum and disturb the Doppler frequency estimation. Compounding *N* frames however has the negative side effect of reducing the frame rate by a factor of *N* however. By further developing our initial observation, it is easy to determine that to separate the out-of-cell tones (phase progression is a function of the transmit angle sweep) from the in-cell Doppler tones (phase progression is a function of time) without frame compounding, perhaps the transmit angle sweep need not follow a linear progression in time. We thus developed the random transmit angle sweep, which converts out-of-cell tones into a

signals with randomized phase, and are thus spectrally spread and appear noise-like in the frequency domain, and hence do not affect the frequency estimation.

1.6 Thesis outline

Chapter 2 introduces a new plane-wave Doppler technique invented for this thesis, called spread-spectrum Doppler. The spread-spectrum method uses a sequence of randomized plane-wave tilt angles to spread the frequency spectrum of out-of-cell scatterers while keeping that of the in-cell scatterers intact. The spreading causes suppression of the out-of-cell scatterers in the frequency domain without the need for compounding or reducing the frame rate, and since most velocity estimation methods take place in the frequency domain, velocity estimates are improved due to the higher spatial resolution. Since no compounding is performed, the frame rate is not reduced, and higher velocities may be measured without aliasing concerns. Experiments using a carotid artery phantom with constant flow are presented to demonstrate that the spread-spectrum method more accurately measures the parabolic flow profile of the vessel and outperforms conventional plane-wave Doppler in both spatial resolution and estimation of high flow velocities. The spread-spectrum method however changed the clutter filter processing mechanism in a way that made the tissue clutter rejection suboptimal.

Chapter 3 seeks to improve the clutter filter performance with the aid of a segmented plane-wave tilt angle sweep and a periodic reshuffling clutter filter to improve tissue suppression as well as vessel wall clutter. Additionally, the new segmented sweep plan allows retrospective selection of the Doppler ensemble size for velocity estimation. Field II [43], [44] simulations are presented and demonstrate the improvements in Doppler SNRs. Additionally, carotid phantom experiments were conducted and also demonstrate improved Doppler SNR, but point to the need for further improvement to match clutter filtering in compounded plane-wave imaging.

Chapter 4 explores mean velocity estimation methods using chirps, when applied to compound plane-wave imaging of pulsatile flow. Two methods are proposed; the chirped Fourier transform (CFT), and the Matching Pursuits decompositions using a chirplet basis. Field II simulations and Carotid phantom experiments are presented and they

demonstrate reduced standard deviations at areas of high acceleration, when using the CFT as opposed to the conventional IWMF method.

References

[1] K. K. Shung, Diagnostic Ultrasound, Boca Raton, FL: CRC press - Taylor & Francis Group, 2006.

[2] S. Bjærum, H. Torp and K. Kristoffersen, "Clutter Filter Design for Ultrasound Color Flow Imaging," *IEEE Transactions on Ultrasonics, Ferroelectrics and Frequency Control,* vol. 48, no. 2, pp. 204-216, 2002.

[3] J. A. Jensen, S. I. Nikolov, K. L. Gammelmark and M. H. Pedersen, "Synthetic aperture ultrasound imaging," *Ultrasonics,* vol. 44, pp. e5-e15, 2006.

[4] G. Montaldo, M. Tanter, J. Bercoff, N. Benech and M. Fink, "Coherent Plane-Wave Compounding for Very High Frame Rate Ultrasonography and Transient Elastography," *IEEE Transactions on Ultrasonics, Ferroelectrics, and Frequency Control,* vol. 56, no. 3, pp. 489-506, March 2009.

[5] B. Delannoy, R. Torgue, C. Bruneel, E. Bridoux, J. M. Rouvaen and H. LaSota, "Acoustical image reconstruction in parallel-processing analog electronic systems," *Journal of applied physics,* vol. 50, pp. 3153-3159, 1979.

[6] D. Shattuck, M. Weinshenker, S. Smith and O. Von Ramm, "Explososcan: A parallel processing technique for high speed ultrasound imaging with linear phased arrays," *Journal of acoustic society,* vol. 75, no. 4, pp. 1273-1282, 1984.

[7] J. Y. Lu, "2-D and 3-D high frame rate imaging with limited diffraction beams," *IEEE Transactions on Ultrasonics, Ferroelectrics and Frequency Control,* vol. 44, pp. 839-856, 1997.

[8] L. Sandrin, S. Catheline, M. Tanter, X. Hennequin and M. Fink, "Time resolved

pulsed elastography with ultrafast ultrasonic imaging," *Ultrasonic Imaging,* vol. 21, pp. 259-272, 1999.

[9] J. Cheng and J. Y. Lu, "Extended high frame rate imaging method with limited diffraction beams," *IEEE Transactions on Ultrasonics, Ferroelectrics and Frequency Control,* vol. 53, pp. 880-899, 2006.

[10] I. K. Ekroll, M. M. Voormolen, O. K.-V. Standal, J. M. Rau and L. Lovstakken, "Coherent compounding in Doppler imaging," *IEEE Transactions on Ultrasonics, Ferroelectrics and Frequency Control,* vol. 62, no. 9, pp. 1634-1643, 2015.

[11] M. H. Soumek, Synthetic Aperture Radar. Signal Processing with MATLAB Algorithms, New York: John Wiley and Sons, 1999.

[12] M. O'Donnell and L. Thomas, "Efficient Synthetic Aperture Imaging from a Circular Aperture with Possible Application to Catheter-based Imaging," *IEEE Transactions on Ultrasonics, Ferroelectrics and Frequency Control,* vol. 39, pp. 366-380, 1992.

[13] M. Karaman and M. O'Donnell, "Subaperture Processing for Ultrasonic Imaging," *IEEE Transactions on Ultrasonics, Ferroelectrics and Frequency Control,* vol. 45, pp. 126-135, 1998.

[14] G. Lockwood, J. Talman and S. Brunke, "Real-time 3-D Ultrasound Imaging Using Sparse Synthetic Aperture Beamforming," *IEEE Transactions on Ultrasonics, Ferroelectrics and Frequency Control,* vol. 45, pp. 980-988, 1998.

[15] J. Bercoff, G. Montaldo, T. Loupas, D. Savery, F. M'ezi'ere, M. Fink and M. Tanter, "Ultrafast compound Doppler imaging: Providing full blood flow characterization"," *IEEE Transactions on Ultrasonics, Ferroelectrics, and Frequency Control,* vol. 58, pp. 134-147, 2011.

[16] A. Heimdal and H. Torp, "Ultrasound Doppler measurements of low blood flow: Limitations due to clutter signals from vibrating muscles," *IEEE Transactions on*

Ultrasonics, Ferroelectrics, and Frequency Control, vol. 44, no. 4, pp. 873-881, 1997.

[17] J. C. Willemetz, A. Nowicki, J. J. Meister, F. D. Palma and G. Pante, "Bias and variance in the estimate of the Doppler frequency induced by a wall motion filter," *Ultrasonic Imaging,* vol. 11, no. 3, pp. 215-225, 1989.

[18] C. Tysoe and D. H. Evans, "Bias in mean frequency estimation of Doppler signals due to wall clutter filters," *Ultrasound in Medicine and Biology,* vol. 21, no. 5, pp. 671-677, 1995.

[19] C. Demené, T. Deffieux, M. Pernot, B.-F. Osmanski, V. Biran, J.-L. Gennisson, L.-A. Sieu, A. Bergel, S. Franqui, J.-M. Correas, I. Cohen, O. Baud and M. Tanter, "Spatiotemporal Clutter Filtering of Ultrafast Ultrasound Data Highly Increases Doppler and fUltrasound Sensitivity," *EEE TRANSACTIONS ON MEDICAL IMAGING,* vol. 34, no. 11, pp. 2271-2285, 2015.

[20] B. Angelsen, "Instantaneous frequency, mean frequency, and variance of mean frequency estimators for ultrasound blood velocity Doppler signals," *IEEE Transcations on Biomedical Engineering,* vol. 28, pp. 733-741, 1981.

[21] C. A. C. Bastos, P. J. Fish and F. Vaz, "Spectrum of Doppler Ultrasound Signals from Nonstationary Blood Flow," *ieee transactions on ultrasonics, ferroelectrics, and frequency control,,* vol. vol. 46, no. 5, pp. 1201-1217, 1999.

[22] R. Willink and D. H. Evans, "Statistical bias and variance in blood flow estimatin by spectral analysis of Doppler signals," *Ultrasound in Medicine and Biology,* vol. 21, pp. 919-935, 1995.

[23] S. M. Kay and S. L. Marple, "Spectrum analysis - a modern perspective," *Proceedings of the IEEE,* vol. 69, no. 11, pp. 1380-1419, 1981.

[24] P. J. Vaitkus and R. S. C. Cobbold, "A comparative-study and assessment of

Doppler ultrasound spectral estimation techniques. 1. Estimation methods," *Ultrasound in Medicine and Biology,* vol. 14, no. 8, pp. 661-672, 1988.

[25] P. Vaitkus and R. Cobbold, "A comparative-study and assessment of Doppler ultrasound spectral estimation techniques. 2. Methods and results," *Ultrasound in Medicine and Biology,* vol. 14, no. 8, pp. 673-688, 1988.

[26] K. Kaluzynski, "Order selection in Doppler blood flow signal spectral analysis using autoregressive modelling.," *Med. Biol. Eng. Comput.,* vol. 27, pp. 89-92, 1989.

[27] F. Shlindwein and D. Evans, "Selection of the order of autoregressive models for spectral analysis of Doppler ultrasound signals," *Ultrasound in medicie and biology,* vol. 16, pp. 81-91, 1990.

[28] A. Herment and J. Giovannelli, "An adaptive approach to computing the spectrum and mean frequency of Doppler signals," *Ultrasonics Imaging,* vol. 17, pp. 1-26, 1995.

[29] H. Talhami and K. R.I., "Maximum likelihood frequency tracking of audio pulsed Doppler ultrasound signal using a kalman filter," *Ultrasound in Medicine and Biology,* vol. 14, pp. 599-609, 1988.

[30] Y. Wang and P. J. Fish, "Correction for Nonstationarity and Window Broadening in Doppler Spectrum Estimation," *IEEE SIGNAL PROCESSING LETTERS,* vol. 4, no. 1, pp. 18-20, 1997.

[31] D. H. Evans, J. A. Jensen and M. B. Nielsen, "Ultrasonic color Doppler imaging," *Interface Focus,* vol. 1, no. 4, pp. 490-502, 2011.

[32] J. A. Jensen and N. Oddershede, "Estimation of velocity vectors in synthetic aperture ultrasound imaging," *IEEE Transactions on Medical Imaging,* vol. 25, no. 12, pp. 1637-1644, 2006.

[33] D. Holdsworth, D. Rickey, M. Drangova, D. Miller and A. Fenster, "Computer-controlled positive displacement pump for physiological flow simulation," *Medical and biological engineering,* vol. 29, pp. 565-570, 1991.

[34] K. V. Ramnarine, N. D. K., P. R. Hoskins and J. Lubbers, "Validation of a new blood-mimicking fluid for use in Doppler flow test objects," *Ultrasound in Medicine and Biology,* vol. 24, pp. 451-459, 1998.

[35] T. L. Poepping, H. N. Nikolov, R. N. Rankin, M. Lee and D. W. Holdsworth, "An in vitro system for Doppler ultrasound flow studies in the stenosed carotid artery bifurcation," *Ultrasound in Medicine and Biology,* vol. 28, no. 4, pp. 495-506, 2002.

[36] T. L. Poeping, H. N. Nikolov, M. L. Thorne and D. W. Holdsworth, "A thin-walled carotid vessel phantom for Doppler ultrasound flow studies," *Ultrasound in Medicine and Biology,* vol. 30, no. 8, pp. 1067-1078, 2004.

[37] *IEC 61685, "Ultrasonics - Flow measurement systems - Flow test object,",* Geneva: International Electrotechnical Commission, 2001.

[38] K. V. Ramnarine, T. Anderson and P. R. Hoskins, "Construction and geometric stability of physiological flow rate wall-less stenosis phantoms," *Ultrasound in Medecine and Biology ,* vol. 27, no. 2, p. 245–250, 2001.

[39] R. D.W., P. P.A., C. D.A. and F. A., "A Wall-less Vessel phantom for Doppler ultrasound studies," *Ultrasound in Medicine and Biology,* vol. 21, pp. 1163-1176, 1995.

[40] H. Yip, C. Lu, C. Yang, H. Chang, W. Hung, C. Cheng, S. Chen and C. Wu, "Levels and value of platelet activity in patients with severe internal carotid artery stenosis," *Neurobiology,* vol. 66, pp. 804-808, 2006.

[41] D. Tang, J. Yang and C. K. D. N. Yang, "A nonlinear axisymmetric model with

fluid-wall interactions for steady viscous flow in stenotic elastic tubes," *Journal of Biomechanics Engeineering,* vol. 121, pp. 494-501, 1999.

[42] K. Nandalur, E. Baskurt, K. Hagspiel, M. Finch, C. Philips, S. Bollampally and C. Kramer, "Carotid artery calcification on CT may independently predict stroke risk," *American Journal of Roentgenology,* vol. 186, pp. 547-552, 2006.

[43] J. Jensen and N. Svendsen, "Calculation of pressure fields from arbitrarily shaped , apodized, and excited Ultrasound transducers," *IEEE Transactions on Ultrasonics, Ferroelectrics and Frequency Control,* vol. 39, pp. 262-267, 1992.

[44] J. Jensen, "FIeld: A program for simulating Ultrasound systems," *Medical and Biological Engineering and Computing,* vol. 34, pp. 351-353, 1996.

Chapter 2

2 Spread-spectrum beamforming and clutter filtering for color Doppler plane-wave imaging

© 2016 IEEE. Adapted and reprinted, with permission, from Omar Mansour, Tamie L. Poepping and James C. Lacefield, "Spread-spectrum beamforming and clutter filtering for color Doppler plane-wave imaging, " IEEE Transactions on Ultrasonics, Ferroelectrics, and Frequency Control, vol. 63, no. 11, pp. 1865–1877, 2016.

2.1 Introduction

Plane-wave imaging achieves high frame rates, enabling the capture of fast dynamic events required in various ultrasound applications. In conventional plane-wave imaging with coherent compounding [1], plane-wave pulses are transmitted using a linear sequence of N tilt angles, producing N low-resolution image (LRI) frames at a frame rate equal to the pulse repetition frequency (PRF). Summation is then performed along the N LRI frames to produce a single compounded high-resolution image (HRI), thereby implementing dynamic transmit focusing and achieving beam profiles similar to those in conventional narrow-beam transmit modes.

Frame compounding enables retrospective transmit and receive beamforming that significantly improves resolution for stationary scatterers, but it represents a process of low-pass filtering in which the compounded echoes from fast-moving objects are attenuated. Ekroll *et al*. [2] have shown the attenuating effect of this filtering on high-velocity scatterers and the resulting bias on velocity estimates. An additional drawback of compounding is that the HRI frame rate is reduced to PRF/N, thereby reducing the (slow-time) Nyquist frequency, so velocity aliasing can occur for the already attenuated fast objects. Compounding is nevertheless necessary to improve the beam profile of the LRI frames in order to suppress off-focus or out-of-cell echoes and produce high-resolution frames. If the total transmit angle swing is α_{swing}, then the angle increment is α_{swing}/N. Increasing N reduces the angle increment, thereby improving the beam profile, but it reduces the slow-time sampling rate and hence the unaliased Doppler frequency limit.

Hence, a tradeoff exists between the unaliased Doppler limit and the beam profile. This paper proposes a method that eliminates this tradeoff.

Previous attempts have been made to overcome the compromise between aliasing and resolution. For Doppler flow imaging, Bercoff *et al*. [3] reduced the number of compounded frames to three. Using a 20 kHz PRF, their theoretical HRI frame rate was 6.667 kHz, but due to practical limitations, the actual frame rate was 3.33 kHz. This frame rate allowed the carotid artery to be imaged with Doppler shifts up to 1.667 kHz. However, the lateral beam profile was degraded due to the large transmit angle increments that resulted in higher side-lobe levels. For elastography, Denarie *et al*. [4] used motion compensation to overcome the suppression of fast-moving tissue due to compounding and studied the effect of using alternating-polarity versus linear tilt angle sweeps. Their approach used LRI frames from different transmit angles to estimate the tissue motion, but they indicated the difficulty of differentiating between phase shifts due to tissue motion and due to the different diffraction patterns from the various LRI transmit angles. Porée *et al.* [5] developed a motion compensation method that uses a triangular tilt angle sweep and used it for cardiac tissue-Doppler imaging. Gammelmark *et al*. [6] resolved the diffraction pattern issue for synthetic aperture imaging by using a short sequence for motion detection such that the LRI frames from the same array elements repeat rapidly enough to detect the tissue motion. This short sequence is interleaved with a longer sequence that produces the high-resolution fast B-mode images. However, the Denarie *et al.*, Porée, *et al.*, and Gammelmark *et al*. methods were developed for tissue motion and did not address blood-flow imaging. Posada *et al.* [7] proposed a de-aliasing method that uses multiple staggered PRFs and can be used for imaging blood flow; however, the method did not perform frame compounding and so presumably sacrificed spatial resolution and contrast.

In this paper, we introduce an approach that uses a spread-spectrum technique instead of compounding to achieve dynamic transmit beamforming, thus eliminating the compromise between the maximum unaliased Doppler frequency and the beam profile characteristics. In contrast to conventional plane-wave imaging, where M HRI frames are used to estimate the Doppler parameters (velocity or power) and each of the HRI frames

is formed by coherently compounding N LRI frames for a total of $N \times M$ plane-wave transmissions, we propose transmitting plane waves using an $N \times M$ sequence of random steering angles, and hence, for each point in the image, the Doppler parameters are computed using $N \times M$ samples acquired at the PRF without the use of compounding. Consequently, the maximum unaliased Doppler shift is limited by the PRF, not PRF/N as in conventional plane-wave imaging, and the transmit angle increment is $\alpha_{swing}/(MN)$ instead of α_{swing}/N. As a result, the compromise between the maximum unaliased Doppler frequency and the beam profile is avoided.

The spread-spectrum technique was originally developed for wireless communications to mitigate multi-path fading [8]. It spreads the frequency spectrum of a signal by multiplying the signal with a pseudo-random noise sequence, whose length dictates the frequency spreading factor. The new signal has the same total power as the original narrowband signal, but spread over a wider bandwidth and, hence, the power per frequency bin is much lower than that of the original signal. Spread-spectrum has been previously used in medical ultrasound to increase the transmit power without reducing the axial resolution in phased-array systems [9], [10], and it has also been used in synthetic aperture systems as a form of code division multiple access (CDMA) to enable transmission from multiple transducer elements simultaneously and to separate their corresponding received signals [11] [12].

This paper presents analytic and flow-phantom results that demonstrate the potential of the proposed spread-spectrum plane-wave color Doppler method. The analysis in sections 2.2 and 2.3 shows that, for each point in the field of view, stationary scatterers inside the resolution cell produce echoes that have consistent phase at each transmit angle, whereas scatterers outside the resolution cell produce echoes with random phase due to the random sequence of transmit steering angles. This random phase spreads the spectrum of the echoes from off-focus objects, thereby suppressing those objects and eliminating their effect from the Doppler signal parameter estimates. In contrast, the linear sweep of transmit angles used in conventional plane-wave imaging results in off-focus scatterers producing slow-time signals with frequencies that depend on their lateral position. These off-focus tones make compounding necessary to suppress them. In Sections 2.4 and 2.5,

the proposed spread-spectrum method is compared to conventional plane-wave color Doppler in flow-phantom experiments. The results demonstrate the ability of the spread-spectrum method to accurately image high velocities (up to 400 mm/s) with better vessel delineation and contrast resolution than conventional plane-wave Doppler imaging.

2.2 Theoretical background

2.2.1 Echoes from a Single Plane-Wave Pulse

If we insonify the image scene with a single plane-wave pulse, the pressure waveform transmitted from the transducer array will be:

$$p_0(t) = G(t)\cos(\omega t) = G(t)\frac{e^{j\omega t}+e^{-j\omega t}}{2}, \tag{2.1}$$

where $\omega = 2\pi f$ is the angular frequency, $G(t)$ is the pulse envelope (e.g. a Gaussian window), and the $t = 0$ time reference is taken with respect to the middle of the pulse envelope emitted from the element on the left edge of the array (Fig. 2.1). The positive frequency component of p_0 can be written as:

$$p_0^+(t) = G(t)e^{j\omega t}, \tag{2.2}$$

where the factor of ½ in Eq. (2.1) has been absorbed into $G(t)$. For simplicity of notation, we shall only examine the positive-frequency component, knowing that the negative-frequency component will be conjugate symmetric to the positive-frequency component. Using the coordinate system defined in Fig. 2.1, the normalized pressure (i.e. ignoring signal attenuation due to tissue absorption and scattering) incident from a tilt angle α at a scatterer located at a point (x, z) is:

$$p(\alpha, x, z, t) = G(t - \tau_i(\alpha))e^{j\omega(t-\tau_i(\alpha))}, \tag{2.3}$$

where $\tau_i(\alpha, x, z) = \frac{z\cos\alpha + x\sin\alpha}{c}$ is the transit time for the incident pressure wave to reach the scatterer in a medium with sound speed c. The radio-frequency (RF) signal received by transducer element m due to the single scatterer is:

$$RF(\alpha, m, t, x, z) = G(t - \tau_i(\alpha, x, z) - \tau_r(m, x, z))e^{j\omega(t-\tau_i(\alpha,x,z))}e^{-j\omega\tau_r(m,x,z)}, \tag{2.4}$$

where $\tau_r(m, x, z) = \frac{\sqrt{(x-md)^2+z^2}}{c}$ is the transit time for the scattered wave to reach the transducer element, $m = 0$ denotes the leftmost element, and d is the array's element pitch. Note that the scattering coefficient of the point scatterer has been absorbed, without any loss of generality, into $G(t)$.
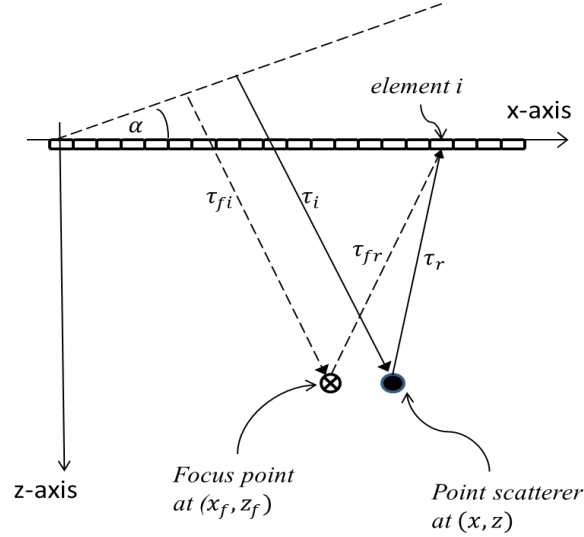
Fig. 2.1: Imaging geometry showing the array transducer transmitting a plane wave at an angle α, an off-focus point scatterer, and the receive focal point. The lengths of the rays along transmit and receive directions represent the one-way transit times for an in-focus echo (dashed lines, τ_{fi} and τ_{fr}) and an off-focus echo (solid lines, τ_i and τ_r), respectively.

In delay-and-sum beamforming with a linear array, receive focusing at a point (x_f, z_f) is achieved by retrospectively delaying the RF signals received at elements of an aperture centered at position $(x_f, 0)$ such that echoes from a scatterer at the focus are received by all of the elements at the same time. Similarly, transmit alignment is achieved by retrospectively delaying the RF signals from multiple tilt angles such that echoes from a scatterer at the focal point are received at the same time, and hence if compounding is performed, echoes may be summed coherently. After delaying the echoes for transmit and receive focusing, samples are then placed at $t = 2z_f/c$. Hence, the RF signal at each element m is delayed by:

$$\tau_f(\alpha, m, x_f, z_f) = \tau_{fi}(\alpha, x_f, z_f) + \tau_{fr}(m, x_f, z_f) - 2z_f/c, \qquad (2.5a)$$

where

$$\tau_{fi}(\alpha, x_f, z_f) = \frac{z_f cos\alpha + x_f sin\alpha}{c}, \text{ and} \tag{2.5b}$$

$$\tau_{fr}(m, x_f, z_f) = \frac{\sqrt{(x_f - md)^2 + z_f^2}}{c}. \tag{2.5c}$$

The first component of Eq. (2.5a) represents transmit alignment, the second component represents receive focusing delays, and the third part is a space-to-time conversion for placing samples at the correct location in time. Hence, the output of the receive beamformer is:

$$RF_{bf}(\alpha, x_f, z_f, x, z, t) = e^{j\omega t}e^{-j\omega(\tau_i - \tau_{fi} + 2z_f/c)} \times$$

$$\sum_{m=l-a}^{l+a} G\left(t - \tau_i - \tau_r + \tau_{fi} + \tau_{fr} + \frac{2z_f}{c}\right)e^{-j\omega(\tau_r - \tau_{fr})}, \tag{2.6}$$

where $x_f = ld$, l is the scanline, $l = 0$ denotes the leftmost scan line, and $2a + 1$ is the number of elements in the receive aperture. The quadrature demodulated baseband signal is then:

$$IQ_{bb}(\alpha, x_f, z_f, x, z, t) = e^{-j\omega(\tau_i - \tau_{fi} + 2z_f/c)} \times$$

$$\sum_{m=l-a}^{l+a} G(t - \tau_i - \tau_r + \tau_{fi} + \tau_{fr} + 2z_f/c)e^{-j\omega(\tau_r - \tau_{fr})}. \tag{2.7}$$

A low-resolution image can be reconstructed from the baseband signals by applying the receive focusing delay at every pixel in the image and sampling at $t = 2z_f/c$:

$$LRI(\alpha, x_f, z_f, x, z) = B(\alpha, x_f, z_f, x, z)e^{-j\omega(\tau_i - \tau_{fi})}, \tag{2.8}$$

where the term inside the summation and the $e^{2z_f/c}$ term have been both absorbed into the function B, which represents the beam profile at (x_f, z_f). Substitution for τ_i and τ_{fi} in Eq. (2.8) yields:

$$LRI\big(\alpha, x_f, z_f, x, z\big) =$$

$$B\big(\alpha, x_f, z_f, x, z\big)e^{-jk[(z-z_f)\cos\alpha+(x-x_f)\sin\alpha]}, \tag{2.9}$$

where $k = \omega/c$ is the wave number).

2.2.2   Echoes from Multiple Plane-Wave Pulses

If N plane-wave pulses are emitted at a pulse-repetition interval, PRI, such that each emission has a tilt angle $\alpha(n)$ drawn from a sequence $\{\alpha_{-N/2}, \dots \alpha_{-1}, \alpha_0, \alpha_1, \dots \alpha_{N/2-1}\}$, and if the point scatterer is moving with a velocity (v_x, v_z), then its displacement from the focal point is $(x_0 + nPRIv_x, z_0 + nPRIv_z)$, where n is the pulse number and spans the range $-N/2$ to $N/2$, and (x_0, z_0) is the scatterer's position relative to the focus at the middle of the sweep, $i.e.$, $x_0 = [x - x_f]_{\alpha=\alpha_0}$ and $z_0 = [z - z_f]_{\alpha=\alpha_0}$. Under these conditions, Eq. (2.9) becomes:

$$LRI\big(\alpha(n), x_f, z_f, x, z\big) = B\big(\alpha(n), x_f, z_f, x, z\big)e^{-jk[(z_0+nPRIv_z)\cos\alpha(n)+(x_0+nPRIv_x)\sin\alpha(n)]}.$$

$$\tag{2.10}$$

For small tilt angles, the approximations $\cos(\alpha) \approx 1$ and $\sin(\alpha) \approx \alpha$ apply, hence the term $e^{-jkz_0\cos(\alpha(n))} \approx e^{-jkz_0}$, which is a constant, and:

$$LRI\big(\alpha(n), x_f, z_f, x, z\big) =$$

$$C\big(\alpha(n), x_f, z_f, x, z\big)e^{-jk(nPRIv_z+x_0\alpha(n)+nPRIv_x\alpha(n))}, \tag{2.11}$$

where $C = Be^{-jkz_0}$. For the case of a linear transmit angle sweep, $\alpha(n) = n\delta$, where $\delta = \alpha_{swing}/N$ is the transmit angle increment, and Eq. (2.11) becomes:

$$LRI\big(\alpha, x_f, z_f, x, z\big) =$$

$$C\big(\alpha, x_f, z_f, x, z\big)e^{-jkPRIv_z n}e^{-jkx_0 n\delta}e^{-jkPRIv_x n^2\delta}. \tag{2.12}$$

Note that in Eqs. (2.10) to (2.12), α, x and z are functions of n; hence, C is also a function of n [13], [14]. Qualitatively, the received echo magnitude decreases as the scatterer's

instantaneous position is offset from the focal point. The amplitude reduction occurs in both the axial and lateral directions due to receive beamforming. Since the instantaneous position of a moving scatterer is a function of time, *i.e.*, the slow-time sample or pulse number n, the beamforming function also becomes a function of n and acts as a time windowing function. If the scatterer's position in the middle of the angle sweep was at the focus, then the window function would be centered and symmetric about the middle of the slow-time signal.

2.2.2.1 Case I: Stationary Scatterers

For stationary objects, substitution of $v_x = 0$ and $v_z = 0$ into Eq. (2.12) yields:

$$LRI\big(\alpha(n), x_f, z_f, x, z\big) = C\big(\alpha(n), x_f, z_f, x, z\big)e^{-jkx_0n\delta}. \tag{2.13}$$

Equation (2.13) shows that when a linear sweep is used without compounding, the slow-time signal from an off-focus stationary scatterer will be sinusoidal, with a frequency that increases with the object's lateral distance from the focus, and that frequency aliasing occurs for scatterer positions far off axis, such that:

$$x_0 \geq \frac{2\pi}{k\delta} = \frac{\lambda}{\delta}. \tag{2.14}$$

Hence, to ensure the grating lobes are outside the imaging scene, whose width is the same as the array width L, the angle step, δ, must be smaller than L/λ, where λ is the wavelength.

(a)

(b)

(c)

(d)
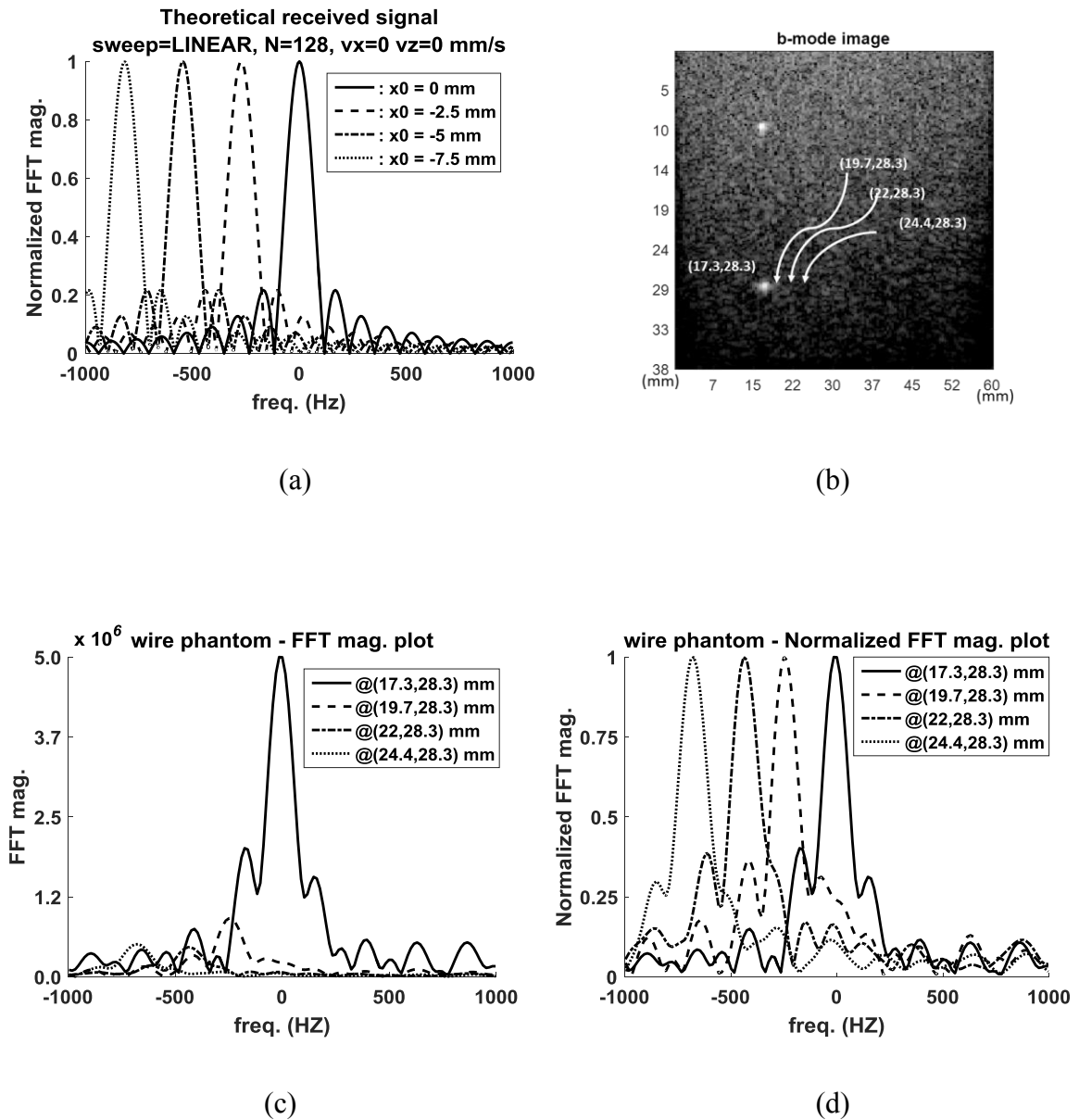
Fig. 2.2: (a) Theoretical normalized FFT plots of Eq. (2.13) for a linear sequence of plane-wave tilt angles with center frequency f_0= 5 MHz, PRF = 15 kHz, transmit angles $-8.192° \leq \alpha < 8.192°$, transmit angle step $\delta = 0.128°$, and ensemble length of N = 128. Waveforms represent signals from point scatterers at different lateral positions relative to the focus point. (b) B-mode image of a wire phantom showing the location of a wire at (17.3, 28.3) mm and the locations of three other pixels displayed for comparison in panels (c) and (d). The sweep used the same parameters as in the theoretical plot (a). The B-mode image was formed by averaging 128 low-resolution frames. The upper wire at approximate depth 10 mm is not used in this experiment (c) FFT of slow-time signals for the 4 pixels shown in (b). The signal level decays as the sample position moves away from the wire due to the receive beam pattern. (d) Normalized FFT of the slow-time wire phantom signals, which removes the signal level decay for better visualization

Fig. 2.2a shows the theoretical normalized magnitude spectra of the slow-time signal *LRI* of Eq. (2.13) for four stationary scatterers when using a linear transmit sweep without compounding. The scatterers are laterally displaced from the focal point by different distances. The slow-time signal of Eq. (2.13) represents samples from LRI frames produced from a linear sequence of transmit tilt angles. This result is in contrast to slow-time signals from conventional plane-wave imaging that are formed after compounding, where each slow-time sample is from a compounded HRI frame. In essence, Eq. (2.13) demonstrates what happens if compounding is avoided and how that affects the resulting spectra of the slow-time signal. Because of transmit alignment, a scatterer at the focal point would have a constant phase throughout the slow-time ensemble, whereas an off-focus scatterer would have a path difference that is a function of the tilt angle, resulting in a linear phase progression as shown in Eq. (2.13). That phase term creates a sinusoidal oscillation in the slow-time signal. The sinc-function appearance of the spectra is the result of spectral broadening created by the finite ensemble length. The receive beamforming contribution, which produces the windowing function $C\big(\alpha(n), x_f, z_f, x, z\big)$, has been neglected in Fig. 2.2a. Note that in conventional plane-wave imaging with coherent compounding, the summation acts as a low-pass filter that suppresses these slow-time tones.

Fig. 2.2b shows an experimental B-mode image of a general-purpose urethane ultrasound phantom containing wire targets (Model 042, Computerized Imaging Reference Systems Inc., Norfolk, VA) imaged using the same sweep parameters as in Fig. 2.2a. The phantom's HRI frame was produced using standard coherent compounding by summing LRI frames from all 128 tilt angles. Fig. 2.2c shows the FFT of slow-time signals from different lateral focus positions in the phantom, the first being the exact position of the wire. The FFT magnitude of the slow-time signal decreases as the focus moves away from the wire's position due to the receive beamforming. Fig. 2.2d shows a normalized plot that removes the beamforming attenuation for better visualization of the spectral peaks.
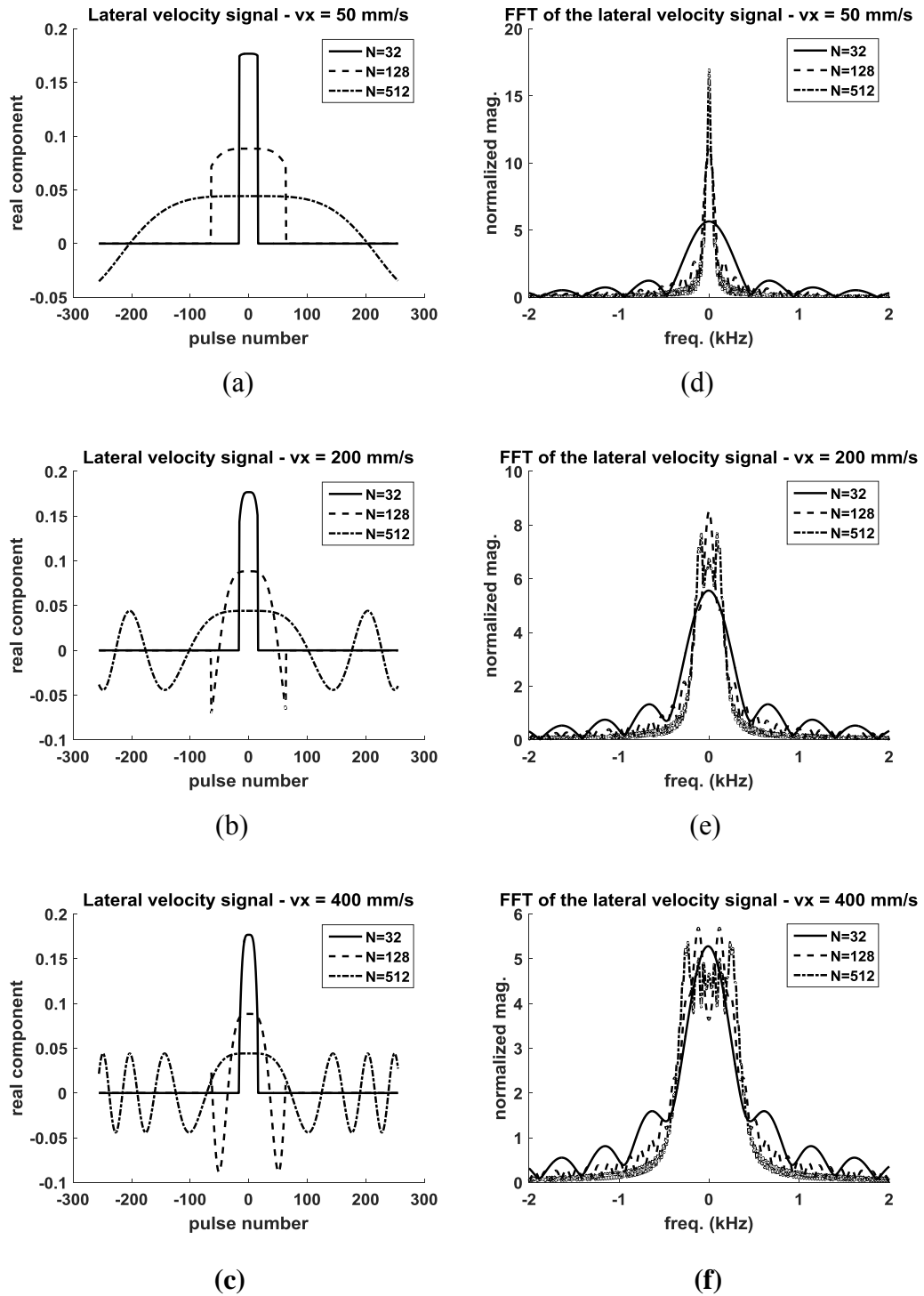
Fig. 2.3: Theoretical normalized lateral velocity signal components (left column) and corresponding Doppler spectra (right column) for 3 different scatterer velocities: (a, d) 50 mm/s, (b, e) 200 mm/s and (c, f) 400 mm/s, each measured with sweep lengths of 32, 128, and 512 pulses. Plots were generated by evaluating Eq. (2.12) for $\alpha_{swing} = [-8.192, 8.192]$, $\delta = 0.512°, 0.128°$, and $0.032°$, and ensemble lengths of N = 32, 128, and 512.

2.2.2.2   Case II: Moving Scatterers

For moving objects, Eq. (2.12) applies. The expression is a product of three exponential components and can be viewed as three separate signals that are inter-modulated. The first signal represents a tone with a Doppler-shifted frequency that is a function of the scatterer's axial velocity, v_z. The second signal represents a tone whose frequency is a function of the scatterer's lateral position, x_0. The third signal has a quadratic term inside the argument of the exponential and represents a chirp that is a function of the scatterer's lateral velocity, v_x. The Fourier transform of the combined signal is hence expected to be that of a time-windowed chirp that is frequency shifted due to the Doppler and lateral position frequency shifts.

Fig. 2.3 shows a plot of the lateral velocity (chirp) signal only using the same transmit parameters as Fig. 2.2, but for different values for N and δ. Note that the signals are normalized to have unit power, so the shorter transmit sequences have larger amplitudes in the time domain. Even for high lateral velocities of 400 mm/s, which can be reached inside the aorta or carotid arteries [15] [16], increasing the number of plane wave angles, N, does not significantly change the bandwidth of the chirp signal, but rather reduces the signal strength, and makes the shape of the spectrum more complex. The bandwidth is primarily dictated by the lateral velocity. By comparing Fig. 2.3f to Fig. 2.2a, we conclude that, for this example's transmit parameters, the lateral velocity component has a less significant effect on the central frequency of the slow-time signal than does the lateral position component. Note that all sweeps in these examples have the same transmit angle swing $\alpha_{swing} = \alpha_{max} - \alpha_{min}$, so the angle increment $\delta = \alpha_{swing}/N$ is smaller for the longer sequences.

2.2.3   Clutter Filtering

To increase the image resolution and form an HRI frame, echoes from off-focus scatterers (*i.e.*, clutter) need to be suppressed. For stationary or slow-moving objects, the in-focus signal is mostly comprised of the lateral position tone, which is at or close to 0 Hz, whereas the off-focus echoes have a frequency that increases with the scatterer's

lateral position relative to the focus as illustrated in Fig. 2.2a. Clutter filtering can be defined in the context of beamforming as the suppression of signals from scatterers that are outside the resolution cell (off-focus) [17] and can be achieved by coherently summing the N LRI frames to form a single HRI frame. For the monochromatic, or narrowband case, applying this process of compounding to (2.13) yields:

$$HRI(x_f, z_f, x, z) = \sum_{n=-\frac{N}{2}}^{\frac{N}{2}-1} C\big(\alpha(n), x_f, z_f, x, z\big) e^{-jkx_0 n\delta}$$

$$\approx C\big(\alpha_0, x_f, z_f, x, z\big) e^{jk\delta x_0/2} \frac{\sin(\frac{\pi x_0 N\delta}{\lambda})}{\sin(\frac{\pi x_0 \delta}{\lambda})}. \tag{2.15}$$

where in Eq. (2.15), we have assumed that the magnitude of the windowing function C does not change much with the tilt angle α, whereas the same assumption cannot be made for the phase of the exponential term. For scatterer positions near the focus, Eq. (2.15) can be approximated by:

$$HRI(x_f, z_f, x, z) \approx C\big(\alpha_0, x_f, z_f, x, z\big) N e^{jk\delta x_0/2} \mathrm{sinc}(\frac{\pi x_0 N\delta}{\lambda}),$$

$$\tag{2.16}$$

which is the response of a decimating mean filter applied to the slow-time signal from (x, z). This filter keeps the tone corresponding to $x_0 = 0$ while suppressing all the other tones that constitute the clutter. The numerator of Eq. (2.15) shows that the resolution is improved (*i.e.*, the main lobe width becomes narrower) by increasing the angle swing $\alpha_{swing} = N\delta$, whereas the denominator and Eq. (2.14) show that grating lobes get closer by increasing the angle step δ, thus raising the sidelobes. A similar result has been previously shown by Denarie *et al.* [4] for the monochromatic case.

For moving scatterers, the in-focus slow-time signal is shifted away from 0 Hz due to the Doppler frequency shift. Suppression and aliasing of the slow-time signal from a moving scatterer may occur when the Doppler shift is above the Nyquist limit, which is half the HRI frame rate. This issue has been studied in more detail by Ekroll *et al.* [2]. Hence,

with current methods, a trade-off exists between improved beam profiles using a large number of plane-wave angles and higher unaliased Doppler frequencies from the use of higher HRI frame rates, which require a lower number of transmit angles.

It should be emphasized that this section considers specifically the contribution of off-focus stationary scatterers when a linear transmit sweep is used without compounding. Such scatterers would generate both B-mode clutter (from off-focus echoes, Eq. (2.16)) and Doppler clutter (via the lateral position component of off-focus echoes in the Doppler signal, Eq. (2.12)). The spread-spectrum method reduces the contributions of those scatterers to the B-mode image by enabling improved transmit beamforming using a smaller transmit angle increment, and from the color Doppler image by spreading the Doppler tone that would otherwise arise from the lateral position signal. A clutter filter is still required to eliminate in-focus echoes from stationary scatterers from the Doppler signal

2.3 Methods

In this section, we propose a method of spreading the clutter spectrum such that it appears as random noise, thereby reducing its peak power, while keeping the in-focus signal intact. When the spreading is sufficient, it can eliminate the need for compounding, and as a result high spatial resolution and high unaliased Doppler frequencies can be obtained simultaneously.

2.3.1   Spread-Spectrum Method

If we use a uniformly distributed pseudo-random sequence $PN(n)$ drawn from the range $[-N/2, N/2 - 1]$ to select the plane-wave transmit angles, then $PN(n)$ is also a pseudo-random sequence:

$$\alpha(n) = PN(n)\delta. \tag{2.17}$$

The pseudo-random sequence may be generated using a linear feedback shift register [18] [19]. Substitution for $\alpha(n)$ in Eq. (2.11) yields:

$$LRI\big(\alpha(n), x_f, z_f, x, z\big) =$$

$$C\left(x_f, z_f, x, z\right)e^{-jkPRIv_z n}e^{-jkx_0\delta PN(n)}e^{-jkPRIv_x\delta PN(n)n} \tag{2.18}$$

Since the system is linear, Eq. (2.18) can be applied individually to in-focus and clutter scatterers. Fig. 2.4 shows an overlaid plot of Eq. (2.18) for two objects, an in-focus scatterer and an off-focus (clutter) object located a lateral distance of 3 mm from focus. The left column shows the signal components for a 512-pulse linear sweep, while the right column shows the signal components for an equal length random sweep using the same transmit parameters as in Fig. 2.2 and Fig. 2.3. The Doppler component is not plotted since it is a single tone that is similar among sweeps.

As can be seen in Eq. (2.18) and Fig. 2.4d, the lateral position component of the slow time signal has a high degree of spectral spreading for clutter scatterers, so it is readily suppressed, whereas the in-focus scatterers produce an intact tone. Comparing Fig. 2.4a and Fig. 2.4d, a linear sweep (Fig. 2.4a) requires that the clutter be suppressed by some additional means such as a low-pass filter (compounding), while a random sweep (Fig. 2.4d) requires no compounding since the off-focus clutter is already spectrally spread and thus suppressed. The suppression occurs because the clutter's lateral position component represents a pseudo-random noise sequence whose symbol rate is equal to the slow-time sample rate (also the PRF); therefore, the clutter spectrum is spread over the entire digital bandwidth, and the clutter power per frequency bin is significantly reduced and becomes noise-like in the frequency domain, which is where most velocity estimators operate. For linear sweeps, the clutter is usually at a higher frequency than the in-focus signal; nevertheless, frequency-domain filters (such as compounding) may not achieve good separation of signal from clutter when the Doppler shift of the in-focus signal is too close to the clutter's lateral position frequency shift, as illustrated in Fig. 2.4c.
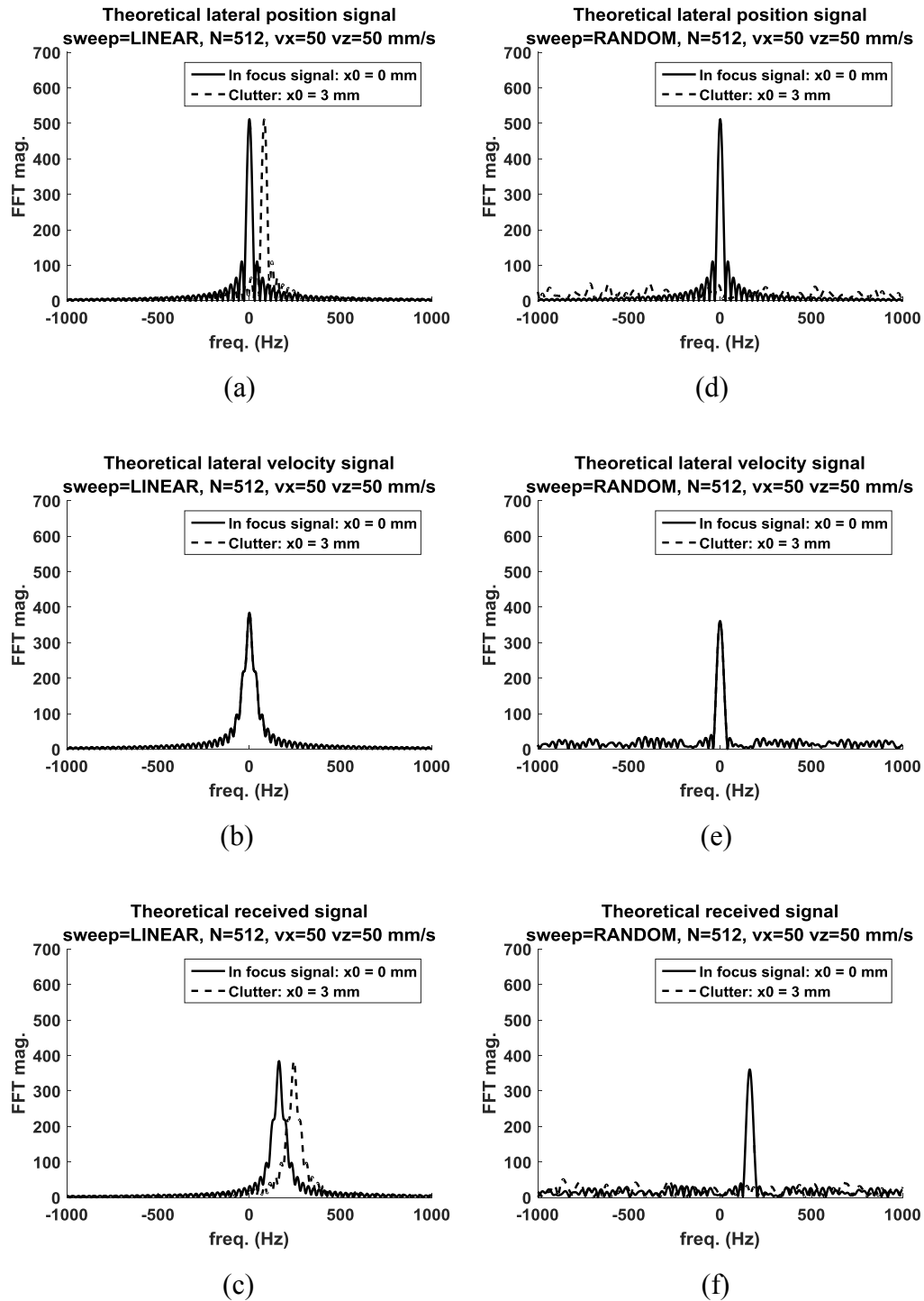
Fig. 2.4: Theoretical Doppler spectra obtained using a 512-pulse transmit-angle sweep using a linear (left column) and random (right column) sequence. Panels show spectra of corresponding lateral position components of in-focus (solid line) and clutter (dashed line) signals (a, d), spectra of lateral velocity component of in-focus and clutter signals (b, e), and complete Doppler spectra of in-focus and clutter signals (c, f)

Fig. 2.4e shows that the lateral velocity component will have some amount of spreading for both in-focus and clutter signals. The degree of spreading depends on the lateral velocity and is a drawback for the random sweep since the spreading degrades the signal magnitude; however, the degradation is usually small for the typical velocities and sweep lengths of interest. Note that in Fig. 2.4e, the lateral velocity component for the in-focus and off-focus scatterers are identical and hence overlaid on top of one another. The same can be said for Fig. 2.4b.

2.3.2   Spread-Spectrum Clutter Suppression

Randomizing the phase of the lateral position signal is responsible for spreading its spectrum, and for maximum spread, the transmit angles should map to a phase variation that is an integer multiple of 2π to produce uniformly distributed random phase for each sample in the slow-time signal. In this case, the frequency spectrum has a signal suppression ratio of $\sqrt{N}$ (the power suppression ratio N is commonly referred to as the processing gain [19] [18]). Hence, maximum spectral spreading of the lateral position component, and accordingly maximum clutter suppression is achieved when:

$$kx_0 N\delta = 2\pi g,$$
(2.19)

or

$$x_0 = \frac{\lambda}{N\delta}g,$$
(2.20)

where g is an integer. Note that these values of x_o are also the lateral position nulls of Eq. (2.15).

2.3.3   Additional Clutter Filtering via Time Shuffling

Since the maximum spread-spectrum suppression gain is equal to $\sqrt{N}$, it amounts to only 27 dB of suppression for a sweep of 512 transmit angles. On the other hand, vessel wall clutter can be 60 dB above the blood signal [20] [21], so spreading the clutter spectrum may not be sufficient to adequately suppress the vessel wall echoes. A method for additional clutter filtering is therefore proposed in this section. Conventional tissue or

wall clutter filters are based on the hypothesis that the clutter signal has somewhat compact support in the frequency domain, thus enabling the application of conventional high-pass finite impulse response (FIR), infinite impulse response (IIR) filters, or alternatively adaptive filters such as the singular value decomposition based filter proposed by Demene *et al.* [22] for ultrafast imaging. In the spread-spectrum method however, the clutter is spread throughout the entire frequency spectrum and an alternative approach needs to be realized for clutter suppression; If, after acquiring data with a random sequence of transmit angles, the ensemble of slow-time samples is reordered such that the transmit angles follow a linear sequence instead of the random one, the samples of the slow-time signal are now time shuffled. This reordering process is a linear operation, so the in-focus and clutter signals can still be analyzed individually. After time shuffling, Eq. (2.18) becomes:

$$LRI\big(\alpha(n), x_f, z_f, x, z\big) =$$

$$C\big(x_f, z_f, x, z\big) e^{-jkPRIv_z PN(n)} e^{jkx_0 \delta n} e^{jkPRIv_x \delta PN(n)n}. \qquad (2.21)$$

Time shuffling spreads the Doppler component and compacts the lateral position component, while the lateral velocity component remains unchanged. For stationary or slow-moving clutter such as echoes from the vessel wall, the Doppler shift is small, so Eq. (2.21) predicts a somewhat compact tone with only a small spread due to the lateral velocity component. At the same time, the in-focus signal is spread approximately uniformly across the spectrum.

To clarify this concept, consider a sine wave representing the in-focus slow-time signal from a random-sweep acquisition and a shuffled sine wave representing clutter. If the slow-time samples are reordered based on Eq. (2.21), then the stationary clutter becomes a single tone, whereas the in-focus signal is now shuffled and has a spectrum like white noise. The wall clutter can then be eliminated by zeroing the first few FFT coefficients above a threshold, with very little effect on the in-focus signal since its spectrum is spread over the entire frequency range. Unshuffling the resulting spectrum returns the signal to the form of Eq. (2.18), but with the wall clutter signal removed. Experimental

results presented in the following sections show that this clutter filter produces images of reasonable quality.

Following the time-shuffling clutter filter, FFT based denoising was performed to reduce the effect of noise in biasing the Kasai [23] average velocity estimates. This bias is particular to the spread-spectrum method since the signal bandwidth occupies a very small percentage of the overall bandwidth (as shown empirically in the Results section), and we observed that this biases the Kasai estimator. Denoising was performed by clearing all frequency bins whose magnitude was less than twice the median magnitude. As part of the denoising process, FFT bins above 1500 Hz and below −1500 Hz were also cleared since 1.5 kHz is the highest expected Doppler shift in the flow-phantom experiments. Other velocity estimation methods that do not require this filtering [24] [25] [26] may be explored in future work.

2.3.4   Flow-Phantom Experiments

Experiments were performed using a custom carotid artery flow phantom [27]. The common carotid segment, which was imaged in this study, consisted of an 8-mm inner diameter and a 1-mm thick polydimethylsiloxane vessel wall surrounded by tissue-mimicking material [28]. Constant flow of the blood-mimicking fluid [29], prepared in house, was controlled using a Compuflow1000 precision pump (Shelley Medical Imaging Technologies, London, ON). A Sonix RP scanner (Ultrasonix Inc., Richmond, BC), equipped with a Sonix DAQ data acquisition module and a 60-mm, 128-element linear-array transducer (L14-5W/60) was used to acquire pre-beamformed channel data sampled at 40 MHz with 12-bit quantization. A longitudinal view of the phantom's common carotid artery was imaged using a 5 MHz center frequency, 2-cycle transmit pulse, and a 15 kHz PRF. The transducer was oriented so the long axis of the vessel formed an 18° angle with the lateral dimension of the image. Post processing was performed using MATLAB (version R2015b, The MathWorks, Inc., Natick, MA).

Table 2.1 shows the four different sweep plans used in the experiments. A random angle sweep that implements the spread-spectrum method (RAND512) was compared against two linear sweep plans. All plans have approximately the same number of LRI frames.

Table 2.1: Sweep plans compared in the flow-phantom experiments

Sweep name	LIN5	LIN17	RAND512	RAND512A
Sweep type	Linear	Linear	Random	Random
Number of angles in sweep (N)	5	17	512[*]	512
Doppler ensemble length (M)	100	32	512	512
	(100 sweeps)	(32 sweeps)	(1 sweep)	(1 sweep)
Total number of frames	500	544	512	512
Tilt angle range α_{min}: α_{max} (degrees)	−8.192 to 8.192			
Tilt angle step (δ) (degrees)	4.096	1.024	0.128[*]	0.032

Each angle repeats randomly within the sequence.

The RAND512 and RAND512A plans used a single randomly sequenced sweep to acquire both the B-mode and color Doppler images, so 512 LRI frames were coherently summed to produce each B-mode image and the length of the Doppler ensemble used for velocity estimation was 512 samples. For the LIN5 plan, five LRI frames were acquired by stepping through the transmit steering angles in ascending order and those images were compounded to produce an HRI frame, which was used to form the B-mode image. One hundred HRI frames were constructed by repeating this procedure to yield a Doppler ensemble of length 100 samples. The LIN17 plan was implemented analogously to the LIN5 plan. For each plan, color Doppler images were constructed using a lag-one autocorrelation method [23] for velocity estimation, so the RAND512 and RAND512A plans used all 511 pairs of temporally adjacent plane-wave transmissions for velocity estimation, whereas the linear sweep plans had a much smaller number of consecutive HRI frames available for velocity estimation. The two linear-sweep plans had higher B-mode frame rates than the random-sweep plans, but the color Doppler frame rates of the four plans were similar.

Five experiments were performed. The first four used 10 ml/s flow with each of the four sweep plans described in Table (2.1) (2 linear sweeps and 2 random sweeps), while the

fifth experiment used 5 ml/s flow with the RAND512 plan, for a total of 3 random sweep experiments. Note that in each of the three random sweep experiments, 8 Doppler images were averaged to form the flow profiles, for a total of 24 spread-spectrum Doppler images presented. The difference between the two random-sweep plans is that in RAND512, 128 different tilt angles were used such that each angle is repeated four times in random order, whereas in the RAND512A plan, 512 tilt angles were used without repetition.

2.4 Results

Fig. 2.5 shows color Doppler high-resolution images of 10 ml/s flow produced using two linear and one random (RAND512) sweep plans. The RAND512A image is not displayed as it looks similar to the RAND512 image. For the linear sweep plans, a color pixel is displayed if the power of the slow-time wall-filtered signal is above the 90th percentile, whereas for the random sweep plan, a color pixel is displayed when the Doppler spectra's peak-to-noise ratio (PNR) is above the 90th percentile. The PNR of the spread-spectrum Doppler signal is defined as the ratio between the peak FFT magnitude and the estimated noise level at the same frequency bin as the peak. The median magnitude across all FFT bins is used as the estimated noise level because, in our experiments, there is a strong but sparse (with respect to the 15 kHz sampling rate) Doppler signal spectra that renders the mean magnitude a biased estimator of the noise level. The different processing of the random-sweep images was necessary as a side effect of spreading the clutter over the entire bandwidth, which resulted in different background levels inside and outside the vessel. In the LIN5 image (Fig. 2.5a), the color pixels extend outside the lumen more than in the other images. Velocity aliasing and suppression of higher velocities is evident in the LIN17 image (Fig. 2.5b), with some areas near the center of the lumen showing no flow at all.
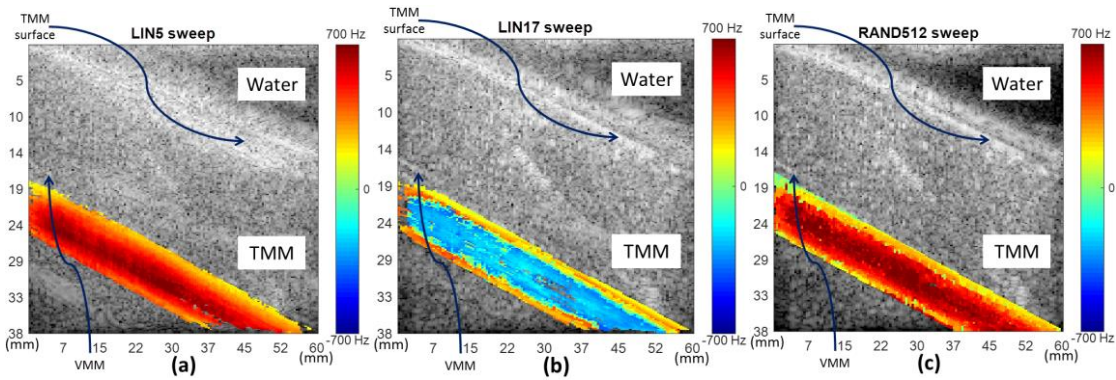
Fig. 2.5: Color Doppler images of a thin-walled vessel phantom for 3 sweep plans defined in Table 2.1: (a) LIN5, (b) LIN17, and (c) RAND512. Images are spatially and temporally processed to improve clarity. The phantom's tissue-mimicking material (TMM) and vessel-mimicking material are described in [27]. All gray-scale images are displayed using 60 dB dynamic range.
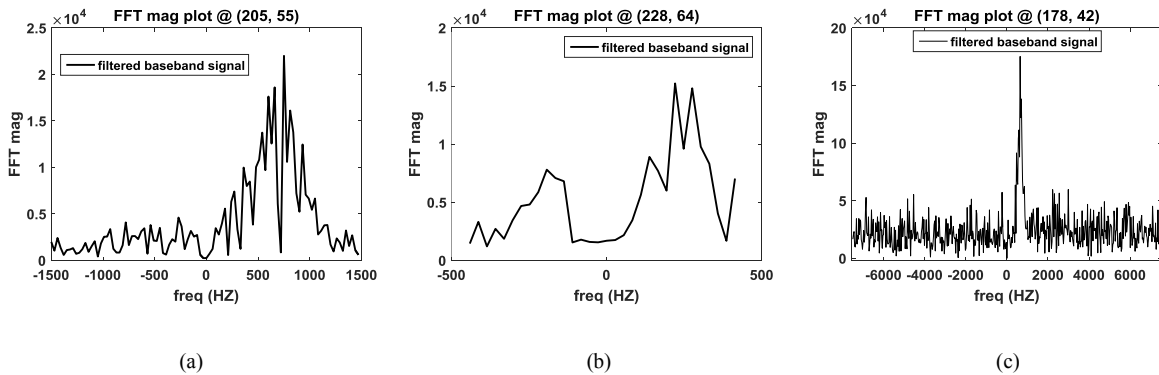
Fig. 2.6: Doppler spectra showing the FFT magnitude for a Doppler ensemble for 3 sweep plans defined in Table 2.1, demonstrating the effective slow-time sampling frequencies, 3 kHz, 0.882 kHz, and 15 kHz, respectively for the (a) LIN5, (b) LIN17, and (c) RAND512 sweep plans. Data were acquired from the flow-phantom images shown in Fig. 2.5.

Fig. 2.6 shows the FFT of the slow-time signals from a representative color pixel for each of the three different sweep plans in Fig. 2.5. The RAND512A Doppler spectrum (not shown) is similar to the RAND512 spectrum (Fig. 2.6c), except for subtle differences in realizations of the noise. Note that the sampling frequencies for the slow-time signals are 3 kHz, 882 Hz, and 15 kHz for the LIN5, LIN17, and RAND512 sweeps, respectively. In the LIN5 and RAND512 data, the selected signal was from a pixel near the center of the

vessel, but a signal was selected near the bottom of the vessel for the LIN17 image to avoid pixels that produced aliased velocity estimates.

(a)   (b)   (c)
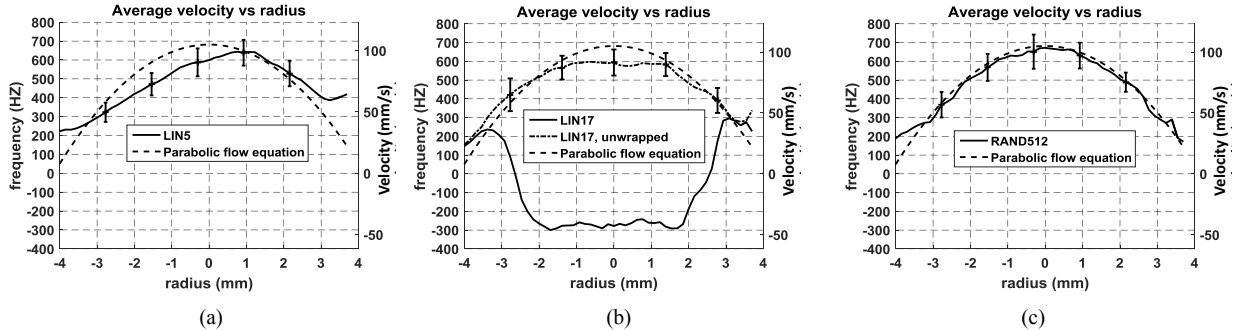
Fig. 2.7: Measured average velocity profiles (as Doppler frequency shift) across the diameter of the flow-phantom vessel using 10 ml/s flow and three sweep plans defined in Table 2.1: (a) LIN5, (b) LIN17, and (c) RAND512. The LIN17 profile in (b) is shown before and after unwrapping the aliased Doppler frequencies. Vertical bars indicate the standard deviation (σ) of the mean velocity estimates among the 8 Doppler ensembles. Length of vertical bars is 2σ.

For each of the sweep types in Fig. 2.5, mean Doppler frequencies were computed as a function of radius, r, creating one profile for each cross-section of the vessel, and then the profiles were averaged from all cross-sections within the vessel and across eight Doppler images. Fig. 2.7shows the mean velocity estimates (displayed as Doppler frequencies) for each sweep plan overlaid against the ideal parabolic flow profile, $v(r) = v_0[1 - \left(\frac{r}{r_0}\right)^2]$, where r_0 is the vessel radius (4.3 mm when distended), r is the radial position of the velocity estimate within the vessel, and v_0 is the axial velocity at the center of the vessel (105 mm/s, computed based on 10 ml/s flow and an 18° vessel inclination angle). The velocity profile estimated using the LIN5 images (Fig. 2.7a) is flatter and also shifted to the right compared to the ideal profile. This may be attributed to the elevated side-lobes in the LIN5 beam pattern, which produced equal but elevated contributions from scatterers on either side of the focal point. In this image, scatterers on the right side contribute more signal power due to lower attenuation since their echoes travel through more transducer coupling fluid (water) and less tissue-mimicking fluid, thereby skewing the profile. In the LIN17 profile (Fig. 2.7b), aliasing occurs because the effective slow-time sampling rate (PRF/N) is 882 Hz compared to a maximum Doppler
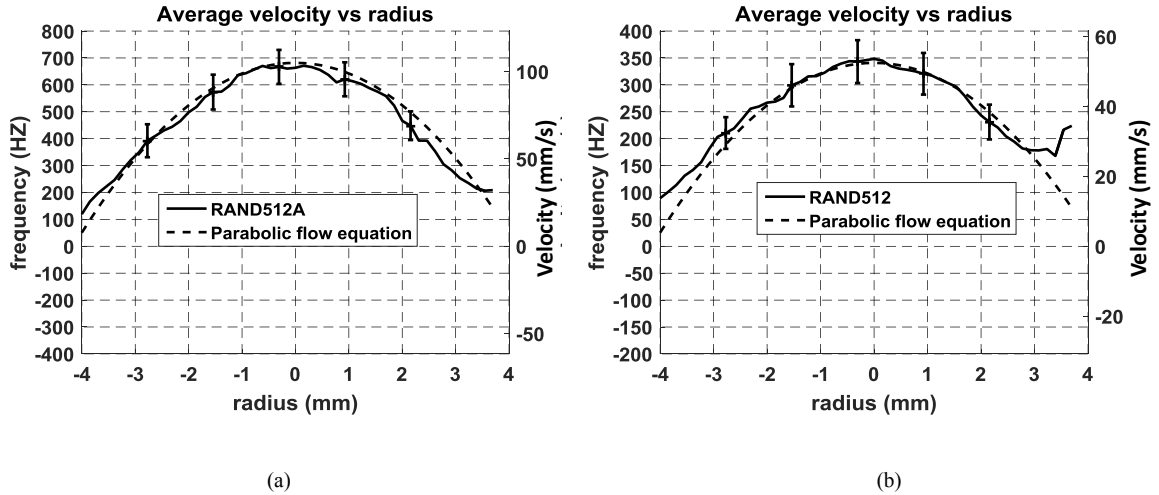
Fig. 2.8: Measured average velocity profiles (as Doppler frequency shift) across the diameter of the flow-phantom vessel for (a) 10 ml/s flow imaged with the RAND512A sweep plan and (b) 5 ml/s flow imaged with the RAND512 sweep plan. Vertical bars indicate the standard deviation (σ) of the mean velocity estimates among the 8 Doppler ensembles. Length of vertical bars is 2σ.

frequency of 700 Hz. Therefore, negative velocities were estimated, and even after velocity unwrapping by adding the slow-time sampling frequency to any negative frequency, the profile plateaus prior to reaching the maximum Doppler frequency of 700 Hz. In contrast, the RAND512 profile (Fig. 2.7c) is closest to the ideal parabolic profile.

Fig. 2.8 shows additional averaged Doppler frequency profiles for 10 ml/s flow imaged using the RAND512A sweep plan and 5 ml/s flow imaged using the RAND512 sweep plan. These profiles also closely follow the ideal parabolic profile, thereby illustrating that the spread-spectrum method performs consistently for different realizations of the transmit angle random sequence and for imaging different flow rates.

The standard deviations (error bars in Fig. 2.7 andFig. 2.8) of the mean Doppler shift averaged over 8 Doppler ensembles were estimated to be 65 Hz for the four 10 ml/s experiments (with all four sweep plans) and 32 Hz for the 5 ml/s experiment in Fig. 2.8b. As shown by Willink *et al.* [30], due to the stochastic nature of the Doppler signal, the standard deviation may be 10% of the mean value when using a single mean velocity estimate, but can be reduced by averaging estimates from multiple ensembles. B-mode contrast was measured in decibels as $C = 20log_{10}(\mu_2/\mu_1)$, where μ_1 is the average gray

level within a triangular area in the water region outside the phantom at the top right corner of the field of view and μ_2 is the average gray level of the tissue-mimicking material at a similar depth. The B-mode contrast was 12.0 dB for the LIN5 images of 10 ml/s flow (Fig. 2.5a), 16.5 dB for the 10 ml/s LIN17 images (Fig. 2.5b), 30.8 dB for the 10 ml/s RAND512 images (Fig. 2.5c), 33.6 dB for the 10 ml/s RAND512A images, and 31.1 dB for the 5 ml/s RAND512 images. The CNR results demonstrate the improved contrast as a result of the finer tilt angle steps that was made possible by using a random sequence.

2.5 Discussion

The conceptual basis of the spread-spectrum method can be understood by considering the slow-time signal produced by a point scatterer insonified from multiple plane-wave transmit angles from the perspective presented in Sect. 2.2. This analysis, which was confirmed by a wire target experiment, demonstrates that off-focus strong scatterers, such as the vessel wall, produce echoes whose phase is a function of the incident plane-wave direction. If the transmit angle is varied in a linear sequence and if compounding is not performed, an off-focus strong scatterer produces a narrowband tone in the resulting Doppler spectrum (Fig. 2.2). Therefore, plane-wave compounding improves image contrast and resolution by first causing off-focus scatterers to have a linearly increasing phase due to the linearly increasing transmit tilt angles, thus producing narrowband tones in the slow time signal, followed by attenuation of these tones via coherent compounding, which essentially acts as a low pass filter. The spread-spectrum method instead suppresses the Doppler signal from an off-focus scatterer by randomizing its phase, thereby rendering compounding unnecessary. The spread-spectrum method thus incorporates an initial clutter-reduction operation into a beamforming procedure for high-frame-rate imaging. The time-shuffling method of clutter filtering introduced in Sect. 2.3.3 makes additional use of the clutter-filtering function of the spread-spectrum method.

The spread-spectrum method is designed to circumvent the tradeoff between beam quality, particularly side-lobe and grating-lobe levels, and maximum unaliased and

unattenuated Doppler frequency that is present in current plane-wave Doppler imaging methods. The flow-phantom experiment was intended to illustrate this capability by comparing the spread-spectrum method to an implementation of a compounding-based method that emphasizes beam quality at the expense of maximum Doppler frequency (LIN17) and a second approach (LIN5) that makes the opposite compromise. The numbers of sweep angles used in the two linear-sweep plans are representative of typical implementations of plane-wave color Doppler [2] [3]. Aliasing and attenuation of Doppler frequencies > 441 Hz is visually apparent in the LIN17 image (Fig. 2.5b). The corresponding estimated Doppler frequency profile (Fig. 2.7b) highlights the consequences of LIN17's relatively low slow-time sampling rate because it was not possible to correct the Doppler estimates near the center of the vessel by unwrapping the aliased frequencies. This outcome, which was previously demonstrated by Ekroll *et al.* [2], was predictable because compounding acts as a low-pass mean filter that has a null at the sampling frequency and because a conventional clutter filter further suppresses signals whose power is concentrated near integer multiples of the sampling frequency.

The differences in beam quality among the linear and random transmit sweep plans is also easily recognized by observing the difference in contrast in the B-mode image data (Fig. 2.5) between the tissue-mimicking material and the water used for acoustic coupling. The spread-spectrum image (Fig. 2.5c) is noticeably superior in this regard to the images produced using the two linear sweep plans (Fig. 2.5a-b). Close inspection of the linear-sweep images also reveals subtle blooming artifacts just outside the vessel wall in the phantom, whereas the vessel boundary is more sharply delineated in the spread-spectrum color Doppler image, which indicates that the spread-spectrum method also provides higher spatial resolution.

The implementation of the proposed method with a sweep length of 512 pulses is perhaps not suitable for pulsatile flow due to its temporal resolution of 32 ms, and hence it is desirable to reduce it to a range of 8 to 16 ms. In the current implementation, the large sweep length was chosen to spread the wall clutter enough to bring it below the background noise level in the Doppler spectrum. In addition, 512 LRI frames were compounded to produce the B-mode images; however, we could have used a different

random sequence that consists of smaller sub-sequences, each spanning the entire tilt angle swing, and used the smaller sub-sequences for compounding and producing B-mode images at a higher frame rate.

It should be emphasized that the spread-spectrum method reduces out-of-cell or off-focus clutter and, as such, it will be effective for imaging velocities where the vessel walls lay outside the main lobe of the beam, without the need for a high-pass wall filter. However, a slow-time high-pass clutter filter is still required to image small vessels where both the lumen and wall are within the main lobe of the beam.

The performance of conventional plane-wave compounding is known to be more sensitive to the accuracy of the assumed speed of sound than is delay-and-sum beamforming (see, for example, Fig. 11 in [31]). The spread-spectrum method should have the same sensitivity to speed of sound as that of conventional plane-wave compounding.

The spread-spectrum method is expected to be best suited for Doppler imaging in areas with high velocity, such as heart chambers, aortic arch, carotid artery, and other large vessels. High impact can be anticipated when imaging areas where the Doppler angle spans a large range, such as the aortic arch, or in cases of stenosis and turbulent flow. In such cases, aliasing is more likely to occur due to the increased likelihood of flow being parallel to the transducer axis, thereby resulting in higher Doppler shifts. In addition, the method may be adapted to suit other applications, such as synthetic aperture and elasticity imaging. This technology may be of particular interest for three-dimensional (3-D) Doppler imaging using synthetic aperture due to its potential to reduce the number of transmissions per frame, which is ordinarily squared when moving from two-dimensional to 3-D imaging.

2.6   Conclusions

The spread-spectrum method for high-frame-rate color Doppler imaging is capable of producing high-spatial-resolution images that also have high maximum unaliased Doppler frequencies. The proposed method employs a random sequence of plane-wave

transmit steering angles, which was shown to distribute the off-focus clutter signal power across the entire Doppler spectrum, thereby suppressing the clutter and alleviating the need for compounding and high-pass clutter filtering. Experimental results obtained from a carotid artery flow phantom demonstrate that the spread-spectrum method eliminates the tradeoff between beam quality, Doppler aliasing, and frame rate that is encountered in current plane-wave Doppler methods. The spread-spectrum method is expected to be valuable for applications that demand imaging of high velocities at high temporal resolution and may also be applicable to synthetic aperture imaging methods.

References

[1] G. Montaldo, M. Tanter, J. Bercoff, N. Benech and M. Fink, "Coherent Plane-Wave Compounding for Very High Frame Rate Ultrasonography and Transient Elastography," *IEEE Transactions on Ultrasonics, Ferroelectrics, and Frequency Control,* vol. 56, no. 3, pp. 489-506, March 2009.

[2] I. K. Ekroll, M. M. Voormolen, O. K. -V.Standal, J. M. Rau and L. Lovstakken, "Coherent compounding in Doppler imaging" *IEEE Transactions on Ultrasonics, Ferroelectrics, and Frequency Control,* vol. 62, no. 9, pp. 1634-1643, 2015.

[3] J. Bercoff, G. Montaldo, T. Loupas, D. Savery, F. M'ezi'ere, M. Fink and M. Tanter, "Ultrafast compound Doppler imaging: Providing full blood flow characterization"," *IEEE Transactions on Ultrasonics, Ferroelectrics, and Frequency Control,* vol. 58, pp. 134-147, 2011.

[4] B. Denarie, T. A. Tangen, I. K. Ekroll, N. Rolim, H. Torp, T. Bjastad and L. Lovstakken, "Coherent Plane wave Compounding for Very High Frame Rate Ultrasonography of Rapidly Moving Targets," *IEEE Transactions on Medical Imaging,* vol. 7, pp. 1265-1276, 2013.

[5] J. Porée, D. Posada, A. Hodzic, F. Tournoux, G. Cloutier and D. Garcia, "High-frame-rate echocardiography using coherent compounding with Doppler-based

motion-compensation," *IEEE Transacations on Medical Imaging,* vol. XX, no. X, January 2016.

[6]   K. L. Gammelmark and J. A. Jensen, "2-D Tissue Motion Compensation of Synthetic Transmit Aperture Images," *IEEE Transactions on Ultrasonics, Ferroelectrics, and Frequency Control,* vol. 61, pp. 594-610, 2014.

[7]   D. Posada, J. Porée, A. Pellissier, B. Chayer, F. Tournoux, G. Cloutier and D. Garcia, "Staggered multiple-PRF ultrafast color Doppler," *IEEE Transactions on Medical Imaging,* vol. XX, no. X, 2016.

[8]   R. Price and P. Green, "A Communication Technique for Multipath Channels," *Proceedings of the International Radio Engineers,* vol. 46, no. 3, pp. 555-570, 1958.

[9]   V. L. Newhouse, D. Cathignol and J. Y. Chapelon, "Introduction to ultrasonic pseudo-random code systems," *Progress in Medical Imaging,* pp. 215-226, 1988.

[10] T. X. Misaridis and J. A. Jensen, "An efective coded excitation scheme based on predistorted FM signal and an optimized digital filter," *IEEE Ultrasonics Symposium,* pp. 1589-1593, 1999.

[11] R. Y. Chiao and L. J. Thomas, "Synthetic transmit aperture imaging using orthogonal Golay coded excitation," *IEEE Ultrasoncis Symposium,* pp. 1677-1680, 2000.

[12] K. L. Gammelmark and J. A. Jensen, "Multielement synthetic transmit aperture imaging using temporal encoding," *IEEE Transactions on Medical Imaging,* vol. 22, no. 4, pp. 552-563, 2003.

[13] A. C. H. Yu, A. H. Steinman and R. S. C. Cobbold, "Transit-Time Broadening in Pulsed Doppler Ultrasound: A Generalized Amplitude Modulation Model," *IEEE transactions on Ultrasonics, Ferroelectrics, and Frequency Control,* vol. 53, no. 3, 2006.

[14] G. GUIDI, C. LICCIARDELLO and S. FALTERI, "“Intrinsic spectral broadening (ISB) in ultrasound Doppler as a combination of transit time and local geometrical broadening," *Ultrasound in Medicine and Biology,* vol. 26, pp. 853-862, 2000.

[15] W. M. Blackshear, D. J. Philips, P. M. Chidos, J. D. Harley, B. K. Thiele and D. E. Strandness, "Carotid artery velocity patterns in normal and stenosed vessels," *Stroke,* vol. 11, no. 1, pp. 67-71, 1980.

[16] L. Segadal and K. Matre, "Blood velocity distribution in human ascending aorta," *Circulation,* vol. 76, no. 1, pp. 90-100, 1987.

[17] M. A. Lediju, M. J. Pihl, J. J. Dahl and G. E. Trahey, "Quantitative Assessment of the Magnitude, Impact and Spatial Extent of Ultrasonic Clutter," *Ultrasonic Imaging,* vol. 30, pp. 151-168, 2008.

[18] R. L. Pickholtz, D. L. Schilling and L. B. Milstein, "Theory of Spread-Spectrum communications - A tutorial," *IEEE Transactions on Communications,* vol. 30, no. 5, pp. 855-884, 1982.

[19] R. L. Peterson, R. E. Ziemer and D. E. Borth, Introduction to Spread-spectrum Communications, Prentice Hall, 1995.

[20] L. Thomas and A. Hall, "An improved wall filter for flow imaging of low velocity flow," *IEEE Ultrasonics Symposium,* pp. 1701-1704, 1994.

[21] A. Heimdal and H. Torp, "Ultrasound Doppler measurements of low blood flow: Limitations due to clutter signals from vibrating muscles," *IEEE Transactions on Ultrasonics, Ferroelectrics, and Frequency Control,* vol. 44, no. 4, pp. 873-881, 1997.

[22] C. Demené, T. Deffieux, M. Pernot, B.-F. Osmanski, V. Biran, J.-L. Gennisson, L.-A. Sieu, A. Bergel, S. Franqui, J.-M. Correas, I. Cohen, O. Baud and M. Tanter,

"Spatiotemporal Clutter Filtering of Ultrafast Ultrasound Data Highly Increases Doppler Ultrasound Sensitivity," *IEEE TRANSACTIONS ON MEDICAL IMAGING,* vol. 34, no. 11, pp. 2271-2285, 2015.

[24] S. M. Kay and S. L. Marple, "Spectrum analysis - a modern perspective," *Proceedings of the IEEE,* vol. 69, no. 11, pp. 1380-1419, 1981.

[25] P. J. Vaitkus and R. S. C. Cobbold, "A comparative-study and assessment of Doppler ultrasound spectral estimation techniques. 1. Estimation methods," *Ultrasound in Medicine and Biology,* vol. 14, no. 8, pp. 661-672, 1988.

[26] P. Vaitkus and R. Cobbold, "A comparative-study and assessment of Doppler ultrasound spectral estimation techniques. 2. Methods and results," *Ultrasound in Medicine and Biology,* vol. 14, no. 8, pp. 673-688, 1988.

[27] T. L. Poepping, H. N. Nikolov, M. L. Thorne and D. W. Holdsworth, "A thin-walled carotid vessel phantom for Doppler ultrasound flow studies," *Ultrasound in Medicine and Biology,* vol. 30, pp. 1067-1078, 2004.

[28] K. V. Ramnarine, T. Anderson and P. R. Hoskins, "Construction and geometric stability of physiological flow rate wall-less stenosis phantoms," *Ultrasound in Medecine and Biology ,* vol. 27, no. 2, p. 245–250, 2001.

[29] K. V. Ramnarine, N. D. K., P. R. Hoskins and J. Lubbers, "Validation of a new blood-mimicking fluid for use in Doppler flow test objects," *Ultrasound in Medicine and Biology,* vol. 24, pp. 451-459, 1998.

[30] R. Willink and D. H. Evans, "Statistical bias and variance in blood flow estimation by spectral analysis fo Doppler signals," *Ultrasound in Medicine and Biology,* vol. 21, no. 7, pp. 919-935, 1995.

[31] D. Garcia, L. Le Tarnec, S. Muth, E. Montagnon, J. Porée and G. Cloutier, "Stolt's f-k Migration for Plane Wave Ultrasound Imaging," *IEEE Transactions on*

Ultrasoncis, Ferroelectrics, and Frequency Control, vol. 60, no. 9, pp. 1853-1867, 2013.

Chapter 3

3 A periodic reshuffling clutter filter for spread-spectrum beamforming in plane-wave color Doppler imaging

The content of this chapter is in preparation for submission to IEEE Transactions in Ultrasonics, Ferreoelectrics, and Frequency Control, with author list Omar Mansour and James C. Lacefield.

3.1 Introduction

Recent advances in compounded plane-wave imaging have enabled continuous and fast acquisition of Doppler slow time samples [1], thereby simultaneously allowing spectral analysis as well as continuous velocity estimation for color imaging. However there existed a compromise between the frame rate (and hence the maximum unaliased measureable velocity) and image resolution. Recently, we proposed a spread-spectrum method that achieves image spatial resolution and high frame rates simultaneously [2]. In this method, a random sequence of plane-wave angles is transmitted to form a Doppler ensemble and as a result, out-of-cell clutter is spectrally spread, thereby significantly reducing its effect on Doppler frequency estimations and effectively achieving high image resolution.

It has been shown that due to strong tissue or vessel wall echoes, clutter-to-signal (CSR) ratios may exceed 60 dB [3] inside blood vessels, which dictates the need for effective wall filtering prior to velocity estimation, even in the presence of high spatial resolution. Clutter filtering has been an active area of research for Doppler ultrasound with conventional focused beams for many years. A major challenge in clutter filtering with focused beam scanning is the limited Doppler ensemble size (8-16 samples []), which makes conventional finite and infinite impulse response filters (FIR, IIR) [4], [5] less effective than their theoretical limits since they were originally developed for steady state response, whereas the Doppler ensemble is too short for higher order filters to reach steady state without consuming a large portion of the ensemble samples. Projection-initialized IIR [6] filters have shown some success in countering this issue. Other filters

that are not based on FIR or IIR, were designed to function with short ensembles, such as the regression filters proposed in [7], down-mixing filters in [8] and [9], and Eigen/Singular value decomposition (SVD) based filters in [10] and [11].

For compounded high-frame-rate imaging, the ensemble size limit has been eliminated in the context of wall filtering, making a continuous stream of Doppler samples available, which allows efficient use of FIR/IIR filters, however they do not adapt to changing clutter conditions that occur in pulsatile flow. A singular-value decomposition based filter that is adaptive to dynamic clutter conditions was proposed in [12]. All previously mentioned filters work well for compounded high-frame-rate imaging, but none are designed for the spread-spectrum beamforming method.

We have previously developed the Reshuffling Clutter Filter (RCF) [2] for rejecting stationary clutter in spread-spectrum Doppler beamforming. In the original RCF method, data is acquired using a random sequence of plane-wave tilt angles to form a time-ordered Doppler ensemble whose frequency spectrum has the in-cell echoes represented with compact bandwidth and its out-of-cell clutter echoes spread over the entire spectrum and look noise-like. The ensemble is then reordered to form an angle-ordered signal, *i.e.* samples are the result of a linearly increasing plane-wave tilt angle, and hence the timing of each sample is now shuffled and thus randomized. As a result, the clutter is spectrally compacted whereas the in-cell echoes are spectrally spread. The RCF method then uses thresholds in the frequency domain of the angle-ordered signal to remove large compact spectral lines, thereby suppressing clutter, and finally re-ordering the samples back to form the time-ordered filtered signal ensemble. In spread-spectrum Doppler beamforming, if the clutter is not properly suppressed, it manifests itself as higher noise in the frequency domain, and may obscure the Doppler signal and result in a pixel within the blood vessel not properly detected as a color pixel.

When we observed color pixel sparsity within the blood vessel during the first series of experiments, we did not know the reason was higher levels of clutter so we addressed it with spatial and temporal filters. After identifying the issue, we addressed it in this manuscript. We hypothesize the root cause of the less than expected clutter suppression is

that tissue clutter did not manifest as compact components in the angle-ordered spectrum and thus not properly suppressed with the thresholding mechanism. In contrast, we believe the vessel wall clutter appeared as two compact spectral components and is properly removed with thresholding.

In this paper we propose a segmented plane-wave tilt angle sweep plan for spread-spectrum Doppler beamforming, and a periodic reshuffling clutter filter (PRCF) for suppressing all types of stationary echoes such as vessel wall or tissue clutter. As in the original spread-spectrum method with RCF, the PRCF method uses a random sequence of plane-wave tilt angles to form a Doppler ensemble, but it divides the sequence into smaller segments, all using the same set of tilt angles, but each with its own unique random sub-sequence. As a result, the angle-ordered ensemble of stationary signals is periodic and occupies discrete spectral components at well-defined locations, which can be cleared without the need for thresholds or threshold calibration. The suppression of discrete spectral components minimally affects the in-cell or blood Doppler signal since it is spread over the entire angle-ordered spectrum. Additionally, the new segmented sweep allows retrospective selection of the Doppler ensemble size for velocity estimation.

In section 3.2, the method and the experimental setup are thoroughly described. Field II [13], [14] simulations and carotid phantom experiments that demonstrate the efficacy of the proposed filter are presented in section 3.3. Section 3.4 discusses the results of 4 different experiments and a field simulation study. Finally, we summarize the filter performance and limitations, and possible future development in section 3.5.

3.2 Methods

3.2.1 The segmented sweep
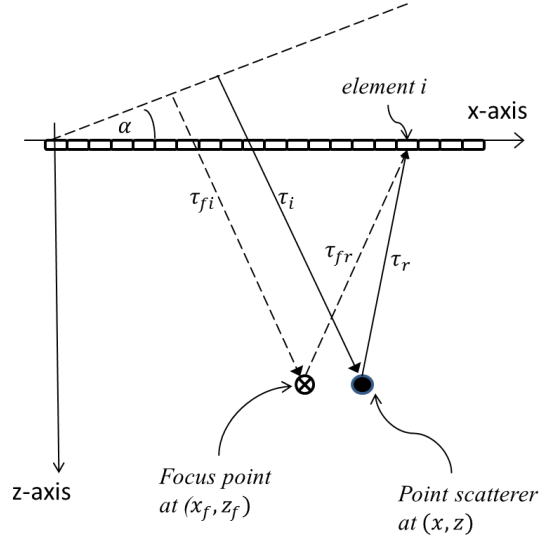
Fig. 3.1: Imaging geometry showing the array transducer transmitting a plane wave at an angle α, an off-focus point scatterer, and the resolution cell center or focal point. The lengths of the rays along transmit and receive directions represent the one-way transit times for an in-focus echo (dashed lines, τ_{fi} and τ_{fr}) and an off-focus echo (solid lines, τ_i and τ_r), respectively.

We have shown in [2] that the slow time Doppler signal at a given pixel or focal point (x_f, z_f) as a result of insonating a point scatterer located at (x, z) as illustrated by the imaging scene in Fig. 3.1, using a sequence of N plane-wave tilt angles is:

$$S_{x_f,x_f}(n) = B_{x_f,x_f}(x(n), z(n))e^{-jk[(z(n)-z_f)\cos\alpha(n)+(x(n)-x_f)\sin\alpha(n)]}. \tag{3.1}$$

where n is the firing pulse number and spans the range $[-N/2, N/2-1]$, (x, z) is the scatterer's position at pulse n, $\alpha(n)$ is the tilt angle used for firing the pulse, and B_{x_f,x_f} is the receive beamforming function at position (x_f, z_f). If the scatterer is moving with constant velocity (v_x, v_z), and was at displacement (x_0, z_0) from the focus at time $n=0$ (the mid pulse within the sweep), then its position at any pulse n is $(x_0 + nPRIv_x, z_0 + nPRIv_z)$, where PRI is the pulse repetition interval, hence,

$$S_{x_f,x_f}(n) = B(n)e^{-jk[(z_0+nPRIv_z)\cos\alpha(n)+(x_0+nPRIv_x)\sin\alpha(n)]} \tag{3.2}$$

For small tilt angles, the approximations $\cos(\alpha) \approx 1$ and $\sin(\alpha) \approx \alpha$ apply, hence the term $e^{-jkz_0\cos(\alpha(n))} \approx e^{-jkz_0}$, is a constant, and absorbed into the beamforming function. If we sweep using a tilt angle sequence such that $\alpha(n) = P(n)\delta$, where $P(n)$ is a pseudo-random noise sequence spanning the range $[-N/2,N/2-1]$ and δ is the angle step size, then,

$$S_{x_f,x_f}(n) = B(n)e^{-jkPRIv_zn}e^{-jkx_0\delta P(n)}e^{-jkPRIv_x\delta P(n)n} \tag{3.3}$$
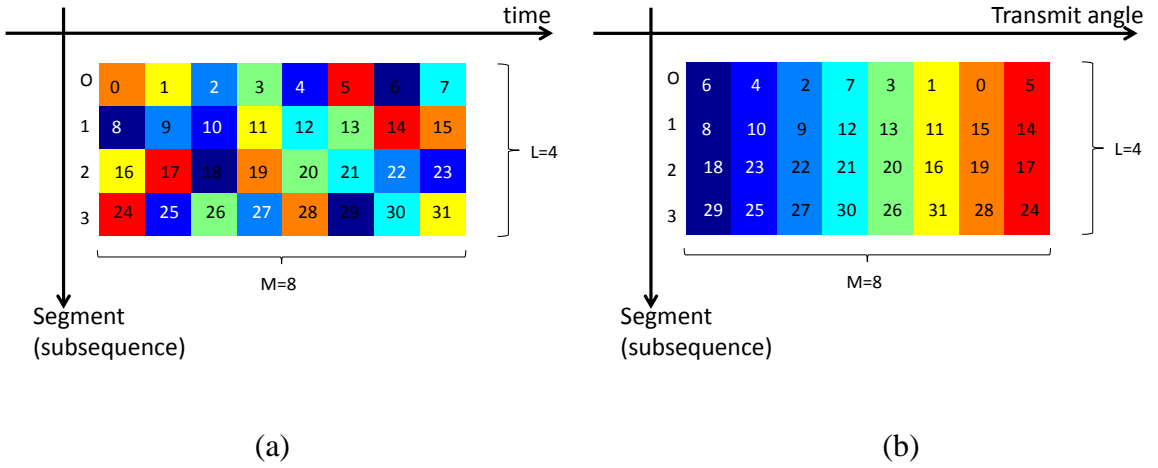
Fig. 3.2: Angle sweep plan for L=4 segments and M=8 tilt angle firings per segment, with the y-axis representing the segment number, color-coded squares representing the tilt angles, and the numbers overlaid on color-coded squares representing the pulse number, demonstrating (a) time ordered sequence, and (b) angle ordered sequence. Observe that only 8 color shades exist, each representing a different value _m_.

where the term e^{-jkz_0} has also been absorbed into _B(n)_.

In the proposed method, we shall further define the random angle sequence _P(n),_ of length _N,_ as a concatenation of _L_ unique uniformly distributed random subsequences or segments, each of length _M_ and spanning the range _[-M/2,M/2-1]_. Fig. 3.2a demonstrates this concept for the case of L=4 and M=8 and displays the time sequence _n_ overlaid on top of the angle sequence _P(n)_, where the tilt angles are represented by color-coded squares. Note that the figure shows the time sequence as spanning the range _[0,N-1]_ instead of _[–N/2,N/2-1]_for ease of viewing. In Fig. 3.2, it can be observed that each color,

representing a different tilt angle, is repeated only once per segment, and if we unfold the time sequence to make it linear instead of two-dimensional, unfolded larger sequence is still random, but with fewer unique tilt angles than the sequence length. This is in contrast to our previous implementation in which *P(n)* was a single sequence of length N, with no repeating numbers, and spanning all entries in the range [*-N/2,N/2*].

One possible implementation is using a linear feedback shift register (LFSR) of length M to produce a segment of length (M-1), and then randomly placing the '0' entry. By using different taps and starting phase, we can produce *L* different random segments, each is unique, uniformly distributed, and has non-repeating numbers, and the larger sequence is also random, uniformly distributed, but with each of the numbers repeating *L* times.

The transmit beam formation now uses *N/L* unique tilt angles instead of *N*, but this should not affect the beam resolution and sidelobes as long as *N/L* exceeds or is close to the limit described in [15], which is typically between 60 and 70 tilt angles. Spread-spectrum suppression is expected to remain as $\sqrt{N}$ [16] since that is the total length of the random sequence.

 The advantage of this arrangement is twofold; First, it allows the retrospective selection of the Doppler ensemble's length so that it may assume any value from the set $\{M, 2M, 3M, ... ML\}$, since each would still be a random sequence. Second, since each tilt angle repeats *L* times, it is possible to view each sequence of similar tilt angles as an independent signal on which conventional clutter filters may be applied, as we shall see in the next section.

3.2.2   The Periodic Reshuffling Clutter Filter

3.2.2.1   Frequency domain formulation

$P(n)$ is a mapping from time index n spanning N values to angle index m spanning M values as shown in Fig. 3.2a, *i.e.* $m = P(n)$. Also, since *P(n)* is a many-to-one mapping (*M<N*), then a different inverse function $P_l^{-1}(m)$ exists for each segment, and it defines a mapping from angle index *m* to time index *n* within each segment *l*. If we wish to

rearrange the signal in Eq. (3.3) such that it is angle ordered, then we need to perform index substitution, i.e. we need to compute

$$S_{x_f,x_f}(m + lM + M/2) = B\left(P_l^{-1}(m)\right)e^{-jkPRIv_zP_l^{-1}(m)}e^{-jkx_0\delta m}e^{-jkPRIv_x\delta mP_l^{-1}(m)} \quad (3.4)$$

where m spans the range [-$M/2$,$M/2$-1] and l spans [-$L/2$,$L/2$-1], $j = \sqrt{-1}$, and k is the wave-number. Fig. 3.2b shows the angle ordered sequence, and demonstrates how the color-coded angles follow a sequential order while the associated (overlaid) time sequence is shuffled and is random since $P_l^{-1}(m)$ is also a random sequence.

In this method we only address stationary clutter, and since reordering is a linear transformation, we can examine the stationary clutter and the Doppler signals individually, knowing that the total signal is the superposition of the two. For a stationary clutter scatterer located at (x_c, z_c), whether wall or tissue, its contribution is obtained by substituting $v_x = v_z = 0$ in Eq. (3.4), hence

$$S_{c,x_f,x_f}(m + lM + M/2) = B(x_c, z_c)e^{-jkx_0\delta m} \quad (3.5)$$

which is a complex sinusoidal function of m, and $B(x_c, z_c)$ is constant for stationary scatterers. Additionally, irrelevant to frequency of the complex sinusoid, the signal in Eq. (3.5) is periodic with period M since l is not a variable inside the exponential. In other words Eq. (3.5) can be written in the form $S_{c,x_f,x_f}(index) = S_{c,x_f,x_f}(index + M)$. Furthermore, since the signal in Eq. (3.5) has an ensemble length N that is an integer multiple of M, i.e. $N=ML$, then the FFT of Eq. (3.5) has coefficients that occur only at bins that are multiples of $N/M=L$.

The signal from a moving blood scatterer shall have a nonzero axial velocity however, and hence according to Eq. (3.4), its rearranged frequency spectrum will not be periodic and will be spread. So, in essence the reshuffling causes the rearranged frequency spectrum of blood echoes to spread and that of stationary clutter to compact or de-spread and only occupy few equally-spaced bins in the FFT.

Zeroing every L^{th} bin in the FFT of the reordered signal removes the stationary part of the signal in Eq. (3.4) which represents stationary clutter (wall or tissue), but keeps non-stationary components which are not periodic and represent blood echoes. In section 3.3, field simulations and experimental results will present examples and FFT plots of the reordered signal before and after the filtering to further illustrate this method.

3.2.2.2   Time domain formulation

An alternative derivation for the PRCF may be obtained by performing the analysis in the time domain; if we rearrange the signal to the form in Eq. (3.4), and examine its representation in Fig. 3.2b, it is easy to imagine multiple mean filters, each operating on a unique tilt angle, i.e. each operating on one column with unique color shade. Stationary clutter may then be estimated as the mean value, and subtracted from the signal. Alternatively, we can run a single mean filter whose impulse response may be written as;

$$h(i) = \frac{1}{L}\sum_{l=0}^{L-1} \delta(i - lM) \tag{3.6}$$

where $h(i)$ is the impulse response and i is the sample index. If this filter is applied to the signal in Eq. (3.5) using circular convolution, then it effectively computes the average for each tilt angle (or shade in Fig. 3.2b). This impulse response represents a pulse train with period M, and hence its FFT will also be a pulse train with period $N/M=L$.

Subtracting the signal in Eq. (3.5) from the mean can be achieved by circular convolution with:

$$h(i) = \delta(i) - \frac{1}{L}\sum_{l=0}^{L-1} \delta(i - lM) \tag{3.7}$$

which has zero-valued FFT bins at multiples of L. Hence zeroing the reordered signal's FFT bins at multiples of L is effectively filtering it with the impulse response of Eq. (3.7), which may be viewed as a multi-tap comb filter. Furthermore, this filter may be implemented in the time domain without the need of reordering by averaging samples of similar tilt angles and using that as the estimate of DC clutter and subtracting it from the corresponding sample, however, the FFT zeroing implementation described in section

3.2-B1 is usually more computationally efficient than circular convolution for large ensembles.

3.2.3   Field Simulations

Synthetic images were produced using Field II [13], [14] simulations running on MATLAB software (version R2016b, The MathWorks, Inc., Natick, MA) with the parallel processing toolbox, and with the parameters shown in Table 3.1. The Scatterers were placed randomly throughout the imaging scene, and then three different scatterer populations were formed for blood, tissue, and wall echoes according to the relative magnitudes in Table 3.1. At each time step equal to $1/FR$, where FR is the frame rate, blood scatterers were allowed to move with constant velocity using a parabolic flow profile in the form $v = V_0[1 - (r/R)^2]$, where V_0 is the maximum frequency, r is the scatterer's radial position within the vessel, and R is the vessel's inner radius. At every time step, the Field II program is run using plane-wave excitation with tilt angles obtained from a predetermined sweep plan as shown in Table 3.2. The random angle sweeps (RAND512 and RAND64x8) implement a random sequence of plane-wave angles and use spread-spectrum beamforming [2], while the LIN1 plan implements a single plane-wave tilt angle and hence does not implement retrospective transmit beamforming. Frame compounding is not performed in any of the sweep plans. The LIN1 plan was selected since it does not require any compounding, and hence does not reduce the frame rate thereby allowing a comparison of its Doppler spectrum to those of the other two random sweep plans. This comparison includes measuring the Doppler peak and noise levels without aliasing concerns.

Receive beamforming was applied to RF data acquired by the field simulations, and the resulting beamformed RF image frames were quadrature demodulated to produce I/Q samples that form Doppler ensembles of length 512, corresponding to 512 acquired frames. Three simulations were run for the different sweep plans of Table 3.2. For clutter

rejection, the LIN1 plan used a 100 Hz high-pass FIR filter, the RAND512 plan used the RCF method, and finally the RAND64x8 plan used the PRCF method proposed in this paper.

A pixel is deemed to be a color pixel if its frequency lies between 50 and 1500 Hz, its Doppler signal's peak-to-noise ratio (PNR) exceeds the 80th percentile PNR of all pixels within the image, and its b-mode level is below the 50th percentile. The PNR is defined in [2] as the ratio of peak FFT magnitude of the Doppler slow time signal to its median magnitude.

Table 3.1: Field II setup parameters

Number of Scatterers per resolution cell	20
Imaging scene (depth, width, thickness) in mm	80, 60,1
Wall-to-blood ratio (linear)	100
Tissue-to-blood ratio (linear)	40
Vessel tilt angle (from horizontal)	20^0
Velocity profile	parabolic
Maximum velocity V_0	400 mm/s
Vessel's inner diameter	8 mm
Frame rate (*FR*)	15 kHz
Excitation frequency	5 MHz
Number of cycles per pulse	2
Tilt angle sweep plan	LIN1, RAND512, an RAND64x8
Total number of firings	512

Transducer type	Linear array
Number of elements	128
Element Pitch	0.472 mm
Element kerf	0.025 mm
Element height	4 mm

Table 3.2: Sweep parameters

Sweep name	LIN1	RAND512	RAND64x8
Sweep type	Linear	Random	Random
Number of unique tilt angles in sweep (M)	1	512	64
Doppler ensemble length (N)	512	512	512
Tilt angle range $\alpha_{min}: \alpha_{max}$ (degrees)	0	-8.192^0 to 8.192^0	
Tilt angle step (δ) (degrees)	0	0.032^0	0.256^0

3.2.4   Experimental setup

Experiments were performed using a custom carotid artery flow phantom [17]. The common carotid segment, which was imaged in this study, consisted of an 8-mm inner diameter and a 1-mm thick polydimethylsiloxane vessel wall surrounded by tissue-mimicking material [18]. Constant flow of blood-mimicking fluid [19], prepared in house, was controlled using a Compuflow1000 precision pump (Shelley Medical Imaging Technologies, London, ON). A Sonix RP scanner (Ultrasonix Inc., Richmond, BC), equipped with a Sonix DAQ data acquisition module and a 60-mm, 128-element linear-array transducer (L14-5W/60) was used to acquire pre-beamformed channel data sampled at 40 MHz with 12-bit quantization.

A longitudinal view of the phantom's common carotid artery was imaged using a 5 MHz center frequency, 2-cycle transmit pulse, and a 15 kHz PRF. Two different transducer orientations were tested; the high tilt orientation, where the transducer was oriented so the long axis of the vessel formed a 20.5° angle with the lateral dimension of the image, and the low tilt orientation with a 10^0 angle. Additionally, two constant flows were tested; 10 mL/s and 5 mL/s, for a total of four distinct experiments, and each experiment had 8 independent Doppler image frames.

Three different sweep plans (Table 3.2) were used in the experiments in a manner similar to that described in section 3.2.3 and the same post processing steps used in the Field II simulations were also used with experimental data.

It should be noted that despite using 64 transmit angles in the RAND64x8 sweep, as compared to 512 transmit angles in the RAND512 plan, similar beam profiles may be obtained, since it has been shown by Montaldo *el al.* [15] that the number of transmit angles required to fully synthesize a focused beam from using multiple transmit plane-waves is $L/(\lambda F)$ where L is the array length, λ is the wave length, and F is the F-number (the ratio between the focus and the active aperture length). In our case the F-number is 3, the aperture length is 60 mm, and the wavelength is 0.3 mm, resulting in 66 required transmit angles.

3.3 Results

Color image, flow=10 mL/s, LIN1 (a)

Color image, flow=10 mL/s, RAND512 (b)

Color image, flow=10 mL/s, RAND64x8 (c)

PNR image, flow=10 mL/s, LIN1 (d)

PNR image, flow=10 mL/s, RAND512 (e)

PNR image, flow=10 mL/s, RAND64x8 (f)
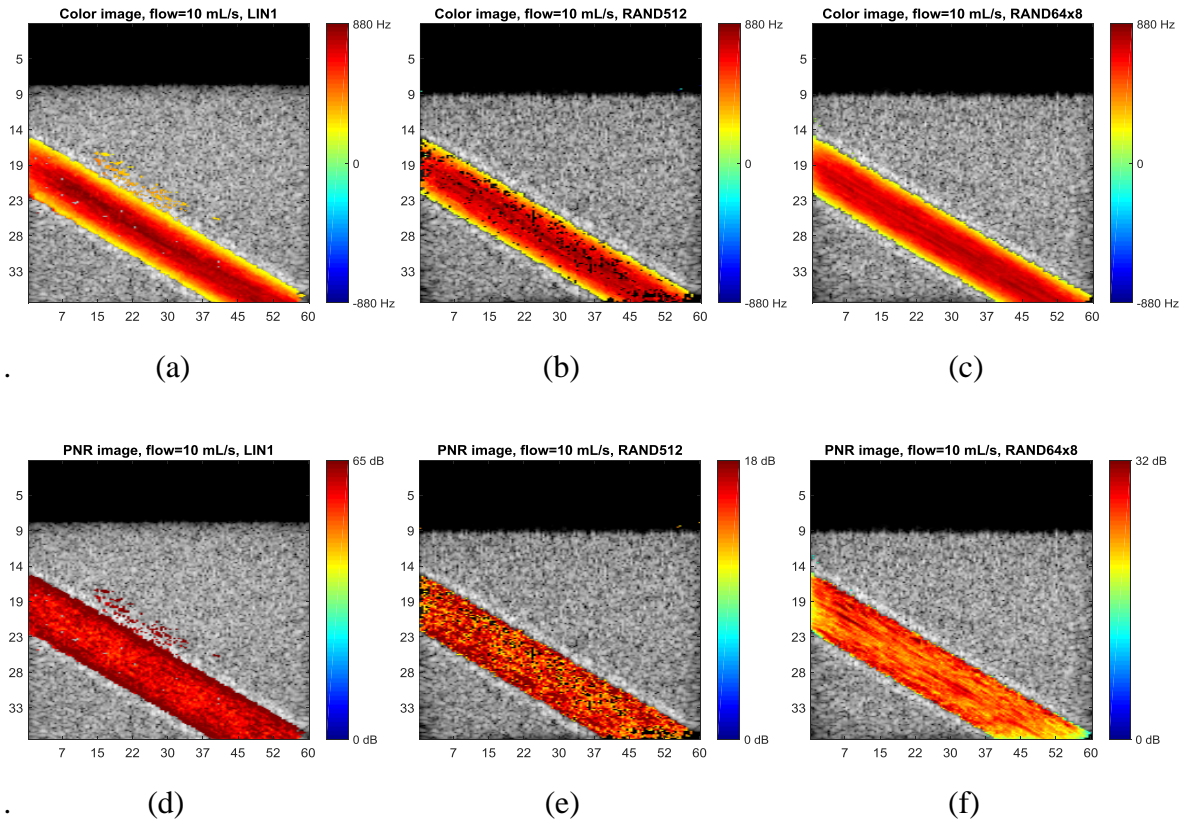
Fig. 3.3: Color flow and PNR images for a Field II simulated vessel phantom using three different sweep plans; LIN1 (a,d), RAND512 (b,e), and RAND64x8 (c,f). All images have the same tilt angle (20^0), and flow (10 mL/s).

Fig. 3.4: Field II simulations - Typical FFT of slow time (Doppler) signals demonstrating the clutter filtering chain for the three different sweep plans.
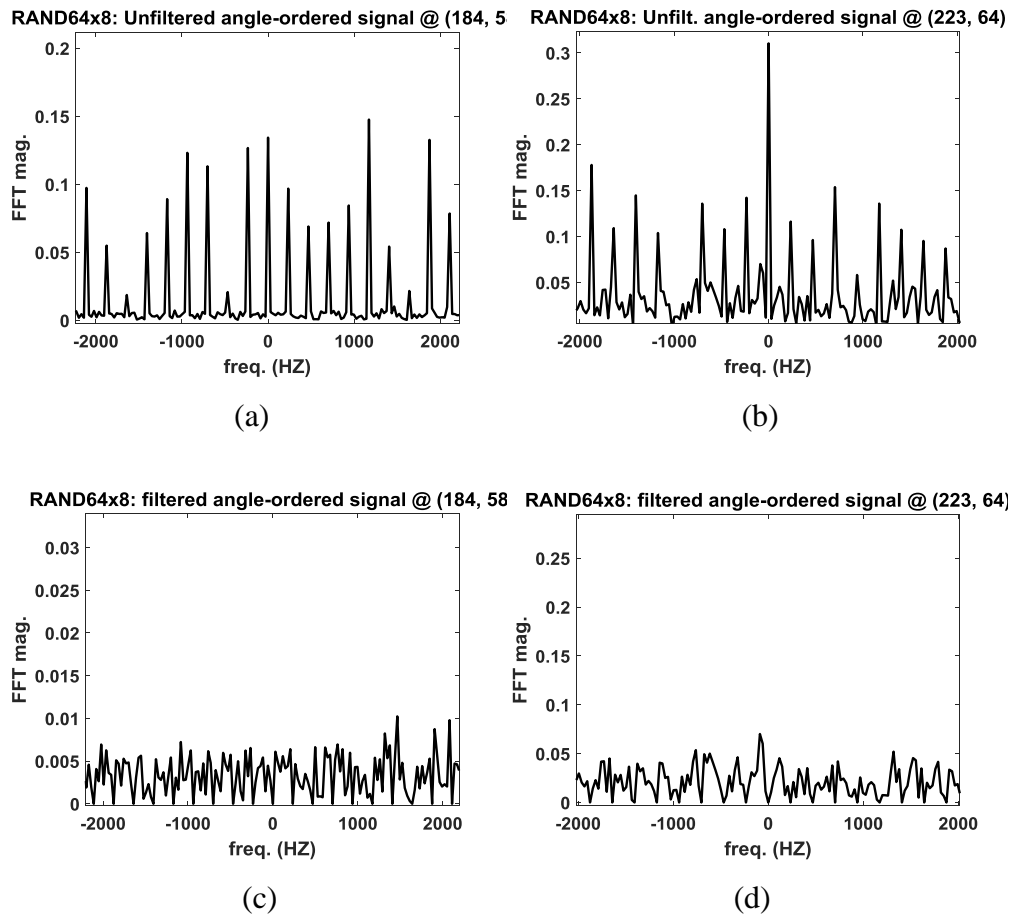
Fig. 3.5: Zoomed in plots for the FFT of the angle ordered signals demonstrating the stationary clutter spectral lines and the operation of the periodic reshuffling comb filter. (a,c): Field II simulations, (b,d): Flow phantom experiment.

Fig. 3.3 displays the color and PNR images for the field simulated vessel. The blank area on the top part of each image is due to the absence of scatterers at depths below 10 mm in order to save simulation time. The vessel fill ratio, which we define as the ratio of color pixels to the total number of pixels within the vessel, is almost 100% for all three sweep plans. The PNR images demonstrate a 14 dB PNR advantage of the RAND64x8 plan over the RAND512. Since field simulations were run without injecting noise into the RF data, the noise-like disturbance in the signal's spectrum is solely due to clutter that is spectrally spread due to the randomized angle sweep plan and made to look noise-like

and hence the difference in PNR is solely due to the improved clutter suppression in the segmented sweep. We chose not to inject noise into the RF data to ensure that the signal-to-noise-ratio (SNR) selection does not affect the PNR or obscure the clutter, hence allowing objective evaluation of each method's ability to suppress clutter. This makes the PNR of the LIN sweep look unrealistically better than it really is, since in practice there will always be some degree of noise as demonstrated later in our experimental results (Fig. 3.7h).

In section 3.2-B1 and Eq. (3.5), we have shown that the stationary clutter in the segmented sweep plan (i.e. the RAND64x8) occupies distinct bins that are multiples of L=8, and hence the only remaining source of out-of-cell clutter shall be due to other blood scatterers. By examining Fig. 3.3f and the associated color bar, we can estimate the PNR to lie mostly between 24-32 dB level, with the average value of 26 as shown in Table 3.3. If a single blood scatterer exists outside a particular resolution cell, i.e. representing beamforming clutter, then theoretically the its amplitude spectrum is spread in the frequency domain and the spread-spectrum suppression of that single scatterer due to 512 random tilt angles is $20log_{10}(\sqrt{512}) = 27$ dB suppression [2]. Since the blood vessel contains many scatterers, we can roughly approximate their combined energy outside the mainlobe of the receive beamformer to be the same as that inside the mainlobe (in-cell scatterers), then PNR values of 24-32 dB seem like a reasonable number to expect. Fig. 3.3e displays lower levels of PNR indicating inferior stationary clutter suppression (wall or tissue). In the LIN1 sweep, the PNR levels are not applicable since there is no clutter spreading and with lack of noise in the RF data, the median of the Doppler signal's FFT then only represents windowing sidelobes which are very low.

Fig. 3.4h demonstrates this point by showing the wall filtered version of the Doppler signal of Fig. 3.4a measured at a typical pixel (184th point of scanline 58). Fig. 3.4b and Fig. 3.4c show the FFT of the slow time Doppler signals for the RAND512 and RAND64x8 sweeps respectively at the same location, and demonstrate the lack of any discernible signal in either one of them prior to clutter filtering. The next row shows the FFT of the angle-ordered signals, demonstrating the existence of distinct spectral lines occurring every 8th bin in the RAND64x8 sweep plan (Fig. 3.4e) representing stationary

clutter as described in Eq. (3.5), and lack of such lines in the RAND512 sweep (Fig. 3.4d) since its clutter signal is not periodic. Additionally, it may be observed that Fig. 3.4d and Fig. 3.4e both exhibit two spectral peaks that represent echoes from the vessel walls (verified by evaluating their frequency and translating it into lateral displacement from the measured pixel using Eq. (3.4)). Moreover, the peaks of the RAND64x8 plan occur at higher frequencies ($\approx$4 kHz) than those in the RAND512 plan ($\approx$500 Hz), *i.e.* 8 times slower, which may be explained by examining the frequency of the exponential in Eq. (3.4) and recalling that the angle step δ is 0.256^0 in the RAND64x8 but 0.032^0 in the RAND512 plan, in other words, the RAND64x8 sweep goes through the entire range of tilt angles 8 times faster that the RAND512, and hence clutter appears at higher frequencies.

The next row of Fig. 3.4 and its zoomed-in version in the left panel of Fig. 3.5 demonstrates the clutter filtering method. Whereas in the RAND512 using the original RCF method, a threshold is manually calibrated as 0.1 of the peak FFT magnitude and all bins with magnitudes above that threshold are cleared, the RAND64x8 which using the PRCF method only clears FFT bins that are multiples of 8 without the need of any manually calibrated thresholds.

The bottom row of Fig. 3.4 shows the FFT magnitude of the filtered time-ordered signals. The LIN1 exhibits the higher PNR, with the reasoning previously discussed, but it has the widest bandwidth, since out-of-cell clutter from blood scatterers is not attenuated as in the other two sweep plans [2]. A comparison between Fig. 3.4(f) and (j) demonstrates the improved clutter suppression in the PRCF method.
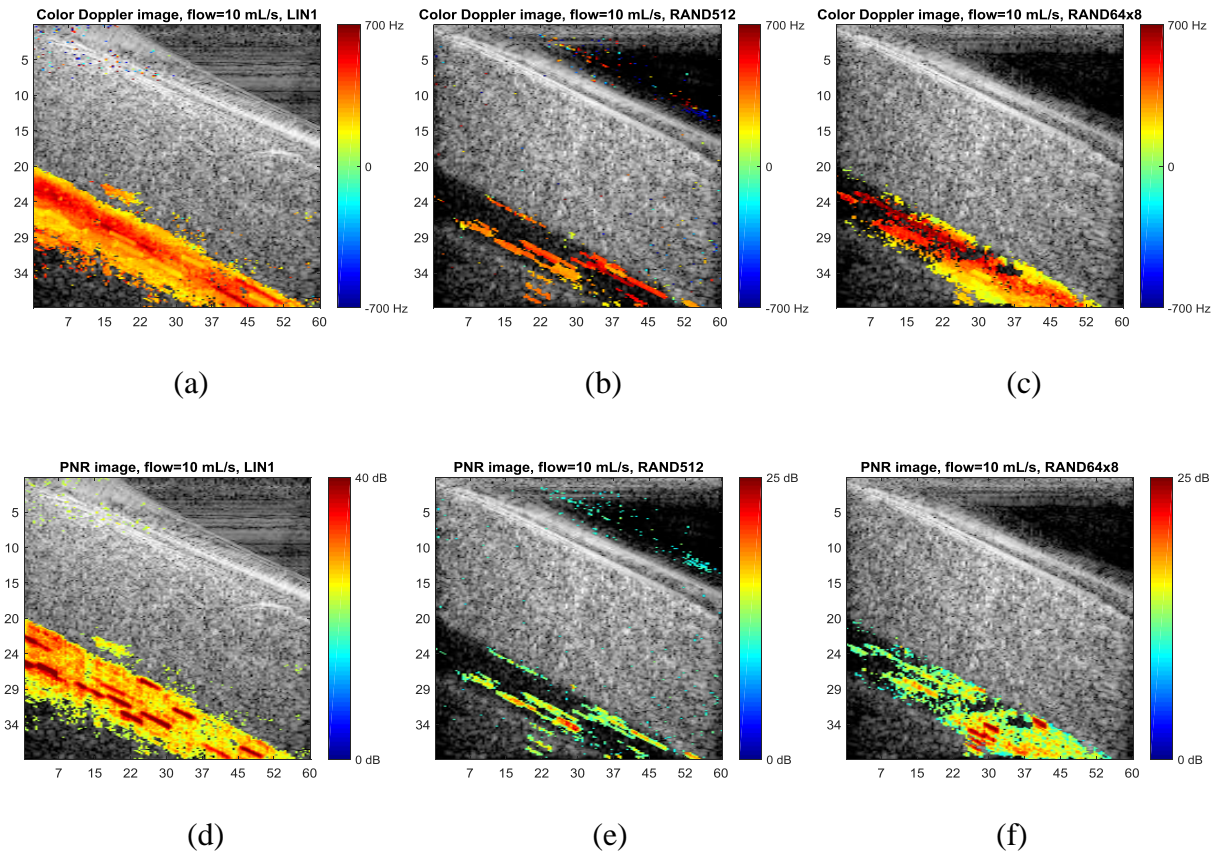
Fig. 3.6: Color flow and PNR images of a carotid flow phantom using three different sweep plans; LIN1 (a,d), RAND512 (b,e), and RAND64x8 (c,f). All images have the same tilt angle (20^0), flow (10 mL/s), and blood mimicking fluid.
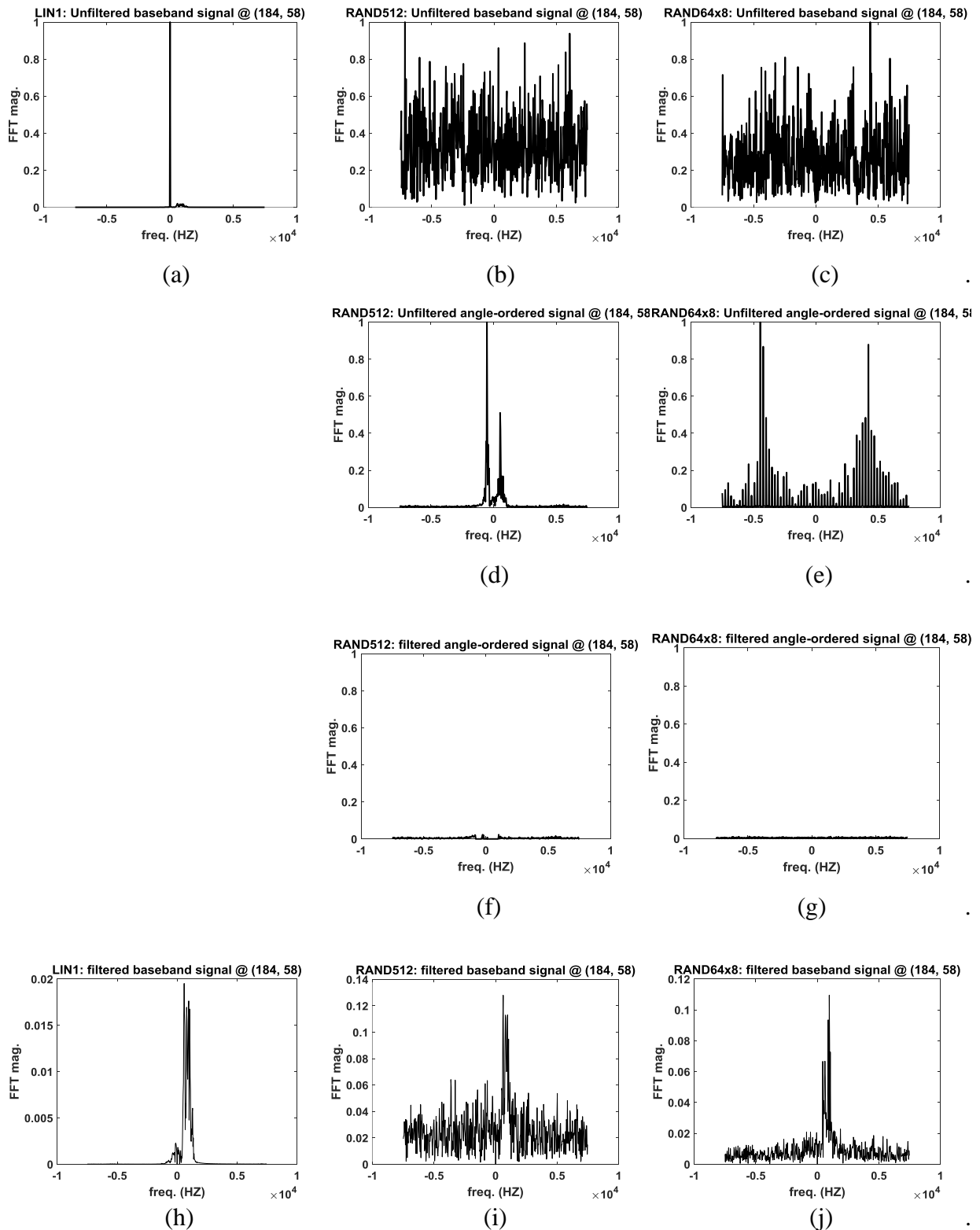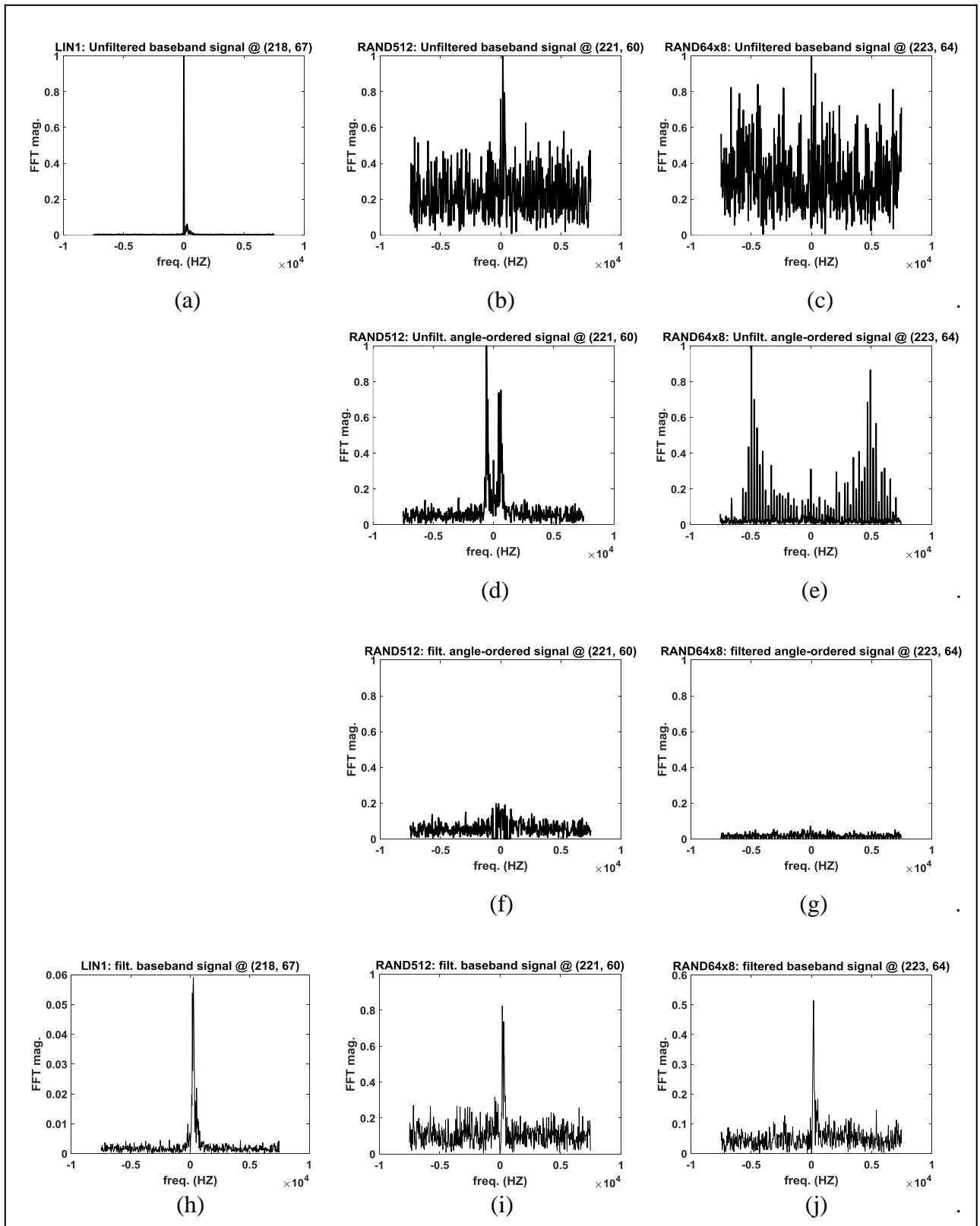
Fig. 3.7: Flow phantom experiments - Typical FFT of slow time (Doppler) signals demonstrating the clutter filtering chain for the three different sweep plans.

In Fig. 3.6, the color and PNR images of the flow phantom experiments demonstrate the improvement in vessel fill in the PRCF method (with RAND64x8 sweep) compared to the original RCF method, and also an improvement in PNR as seen in higher percentage of red and yellow colors in Fig. 3.6f compared to (6e). The vessel fill and the PNR ratios in the spread-spectrum sweeps are evidently lower than that of the LIN1 sweep, which uses a traditional 100 Hz high-pass wall filter. The right panel of Fig. 3.5b and Fig. 3.5d are zoomed-in versions of Fig. 3.6e and Fig. 3.6g.

Fig. 3.7 shows the FFT of typical Doppler signals going through the three different processing chains as in Fig. 3.4, except that a carotid flow phantom is used instead of simulation data. Fig. 3.7h demonstrates the LIN1 filtered Doppler FFT magnitude in the presence of noise, which is in contrast to Fig. 3.4h in which the Field simulated data did not model the noise, thus displaying unrealistically high PNR.

Table 3.3: FFT Peak, PNR, and bandwidth parameters

	$Peak_{av}$ (dB)			PNR_{av}(dB)			Bandwidth (σ_{av}) (Hz)		
	LIN1	RAND 512	RAND 64x8	LIN1	RAND 512	RAND 64x8	LIN1	RAND 512	RAND 64x8
Field II simulation: High tilt, 10 mL/s	117	115	116	59	16	26	179	80	93
Phantom Experiment: High tilt, 5 mL/s.	93	94	87	31	14	18	988	32	49
Phantom Experiment: High tilt, 10 mL/s.	94	96	87	33	15	17	780	46	62
Phantom Experiment: Low tilt, 5 mL/s.	98	96	89	35	14	16	735	45	41
Phantom Experiment: Low tilt, 10 mL/s.	95	95	94	33	14	15	629	65	61

Table 3.3 shows the peak, PNR, and bandwidth parameters averaged over an area of 9x9 pixels, centered at the intersection of scanline 60 and the vessel's center axis. For each sweep type, we computed average values for one Field II simulation with a single Doppler ensemble (512 frames) and four flow phantom experiments with two orientations (high and low) and two flow rates (5 mL/s and 10 mL/s).

The average peaks of the Doppler signals FFT magnitudes are presented so that they are taken into account when evaluating the PNR average measurements. The RAND64x8 using the PRCF method always outperformed the RAND512 with RCF by about 3-4 dB even though three of the four RAND64x8 experiments had lower signal peak levels. The average bandwidth in the two random sweeps is observed to be lower by a factor of 8-10 than that measured in the LIN1 sweep experiments, which is consistent with the higher sidelobe levels in the LIN1 sweep's beamformer, resulting in each image voxel having contributions from adjacent voxels, thus adding additional Doppler frequency components. The bandwidths differed in the field simulations only by a factor of 2 however, but we believe this may be due to using only a 1 mm image scene thickness.

Table 3.4: TPF measurements for the three sweep plans using four different setups

	TPF		
	LIN1	RAND512	RAND64x8
Phantom Experiment: High tilt, 5 mL/s.	0.9	0.13	0.69
Phantom Experiment: High tilt, 10 mL/s.	0.97	0.23	0.58
Phantom Experiment: Low tilt, 5 mL/s.	0.79	0.15	0.47
Phantom Experiment: Low tilt, 10 mL/s.	0.84	0.17	0.35

We measured the true positive fraction (TPF), which we define as the ratio of detected color pixels (where scatterers are deemed to be having non-zero velocities) inside the vessel to the total number of pixels within the vessel. Table 3.4 shows measured TPF values for the three different plans, using four different setups; a high tilt carotid vessel phantom (angle between vessel axis and the horizontal line is 19.5^0) with 10 and 5 mL/s

constant flows, and a low tilt (12.3^0) carotid phantom setup using 10 and 5 mL/s constant flows. For each experiment, the values were averaged over 8 independent Doppler frames. Data shows that the PRCF method (RAND64x8, third column) outperformed the original RCF method (RAND512, second column) in all experiments.

3.4   Discussion

We have shown in [2] that spread-spectrum beamforming improves spatial resolution without reducing the maximum measurable Doppler shift, thereby allowing the imaging of high flow rates with high spatial resolution. In section 3.2, we presented a frequency and time domain formulations for the PRCF method, and showed them to be equivalent. In actuality, our original intent was to develop two separate methods based on the segmented sweep and compare their performance. The frequency domain formulation was our first attempt since we wished to improve over the original reshuffling clutter filter from [2] by removing the need for thresholding and we thought that a segmented sweep that repeats the tilt angle would make stationary echoes periodic, and hence represented by subset of the FFT coefficients, thereby allowing their complete removal without the need for manual threshold calibration. After developing the segmented sweep, we then considered a second, time-domain, approach of treating each tilt angle as a separate channel, running a low pass mean filter on each, and subtracting the mean value from the original signal, since the mean value represents stationary clutter.

Even though it turned out that the two methods were mathematically identical, we chose to present them both since each added a distinct value in analyzing the performance. The frequency domain representation allowed a direct comparison to the original reshuffling clutter filter as shown in Fig. 3.4 and Fig. 3.7, and it proved in Eq. (3.5) that the stationary clutter shall be completely eliminated by clearing the appropriate FFT bins. Additionally, it also indicated that the blood signal is spread in the FFT of the angle-ordered signal, and clearing $1/L$ of its bins theoretically removes $1/L$ of its power. On the other hand, the time domain formulation provides a more intuitive view of the removal process and a comparison to the conventional high-pass filter clutter suppression methods.

To elaborate further on the frequency domain comparison, the original reshuffling clutter filter which assumed the clutter to be formed of few dominant wall echo components, each located at discrete lateral offset x_0 from the center of the resolution cell (or focus) and hence each manifesting itself as a large peak in the FFT of the overall angle-ordered signal $S_{x_f, x_f}(m)$ as seen in Fig. 3.4d and Fig. 3.7d. Our original implementation removed such peaks using manually calibrated thresholds in the FFT domain, and kept the remainder of the FFT signal representing the frequency spread blood echoes. It was not feasible to manually adjust the threshold for every pixel individually, and it is very difficult to adjust the threshold such that tissue clutter, which is not represented in the two FFT peaks, be removed. This is because tissue echoes had levels that are close to blood echoes and they may exist all lateral locations past the vessel wall, thereby not manifesting as large discrete peaks in the FFT of the angle-ordered signal.

The original Reshuffling clutter filter exhibited inferior peak-to-noise ratios compared to compounded beamforming methods, which was our motivation for developing the PRCF method. In Field II simulations, the proposed PRCF method brought the peak-to-noise ratios and vessel fill ratios to the levels expected should we have had no clutter, demonstrating the effectiveness of PRCF in removing stationary clutter. In flow phantom experiments however, the PNR and vessel fill ratios of spread-spectrum beamforming with PRCF were inferior to those obtained using conventional FIR clutter filtering with a single plane-wave tilt angle (LIN1). We have conducted a wire phantom study to compare signal-to-noise ratios (SNR) when using linear plane-wave compounding of different resolutions, and found that with a single plane-wave tilt angle, roughly a 3 dB higher SNR is seen compared to compounding 64 tilt angles, due to the more selectivity and hence less power with the 64 angles. Thus, this explains only a small portion of the PNR inferiority.

Since this inferiority was not seen in the Field II simulations, and Eq. (3.5) proves that stationary clutter may be eliminated by clearing the appropriate FFT bins, we hypothesize that there are some hardware limitations that are not accounted for, that causes stationary clutter to be viewed by the system as non-stationary in our flow phantom experiments. This may be due to sampling time jitter, offsets not properly decaying after rapid tilt

angle switching, or non-constant flow velocity due to wobbles in the flow pump causing vibrations on the vessel wall and hence non-stationary clutter. Additionally, it should be noted that Field II does not model shadowing, reverberation, sample timing jitter, or the big bang portion of the echo signal.

The PRCF has the potential, in future work, to adapt to non-stationary clutter by pre-multiplying the time-ordered signal by $e^{j\omega_c t}$ where ω_c is the central frequency of the clutter and may be estimated by the following two-step procedure:

- For multiple values of angular frequency ω, multiply the time-ordered signal by $e^{j\omega t}$, angle-order the multiplied signal, apply the mean filter defined in Eq. (3.6), and compute the output signal's energy.

- Choose the value of ω with the maximum output energy.

3.5 Conclusion

A stationary clutter filter for spread-spectrum beamforming methods is proposed, and it has been shown to significantly improve wall and tissue clutter rejection as compared to the original method. Field II simulations showed excellent clutter rejection using the proposed method. Flow phantom experiments showed improved performance over the original RCF method, but indicate the need for more advancements to address possible hardware limitations that are not accounted for. We hypothesize that the hardware may have resulted in RF offset levels that differ depending on the sequence of the tilt angle sweep, thus causing echoes from the same stationary object to appear non-stationary and is thus not fully removed by the clutter filter.

The PRCF method may be extended to non-stationary clutter which will enhance its value for the anticipated clinical applications of spread-spectrum Doppler that demand high spatial resolution of high velocities such as heart chambers, aortic arch, or stenosis and turbulence detection in the carotid and other large vessels.

References

[1] J. Bercoff, G. Montaldo, T. Loupas, D. Savery, F. M'ezi'ere, M. Fink and M. Tanter, "Ultrafast compound Doppler imaging: Providing full blood flow characterization"," *IEEE Transactions on Ultrasonics, Ferroelectrics, and Frequency Control,* vol. 58, pp. 134-147, 2011.

[2] O. Mansour, T. L. Poepping and J. C. Lacefield, "Spread-Spectrum Beamforming and Clutter Filtering for Plane-Wave Color Doppler Imaging," *IEEE Transactions on Ultrasonics, Ferroelectrics, and Frequency Control,* vol. 63, no. 11, pp. 1865 - 1877, 2016.

[3] A. Heimdal and H. Torp, "Ultrasound Doppler measurements of low blood flow: Limitations due to clutter signals from vibrating muscles," *IEEE Transactions on Ultrasonics, Ferroelectrics, and Frequency Control,* vol. 44, no. 4, pp. 873-881, 1997.

[4] J. C. Willemetz, A. Nowicki, J. J. Meister, F. D. Palma and G. Pante, "Bias and variance in the estimate of the Doppler frequency induced by a wall motion filter," *Ultrasonic Imaging,* vol. 11, no. 3, pp. 215-225, 1989.

[5] C. Tysoe and D. H. Evans, "Bias in mean frequency estimation of Doppler signals due to wall clutter filters," *Ultrasound in Medicine and Biology,* vol. 21, no. 5, pp. 671-677, 1995.

[6] E. S. .. Chornoboy, "Initialization for Improved IIR Filter Performance," *IEEE TRANSACTIONS ON SIGNAL PROCESSING. VOL 40. NO 3. MARCH 1992,* vol. 40, no. 3, pp. 543-550, 1992.

[7] A. P. Kadi and T. Loupas, "On the Performance of Regression and Step-Initialized IIR Clutter Filters for Color Doppler Systems in Diagnostic Medical Ultrasound," *IEEE TRANSACTIONS ON ULTRASONICS, FERROELECTRICS, AND FREQUENCY CONTROL,* vol. 42, no. 5, pp. 927-937, 1995.

[8] L. Thomas and A. Hall, "An Improved Wall Filter for Flow Imaging of Low Velocity Flow," in *Ultrasonics symposium*, 1994.

[9] S. Bjærum, H. Torp and K. Kristoffersen, "Clutter Filters Adapted to Tissue Motion in Ultrasound Color Flow Imaging," *ieee transactions on ultrasonics, ferroelectrics, and frequency control,* vol. 49, no. 6, pp. 693-704, 2002.

[10] A. C. H. Yu and R. S. C. Cobbold, "Single-Ensemble-Based Eigen-Processing Methods for Color Flow Imaging—Part I. The Hankel-SVD Filter," *ieee transactions on ultrasonics, ferroelectrics, and frequency control,* vol. 55, no. 3, pp. 559-572, 2008.

[11] L. A. F. Ledoux, P. J. Brands and A. P. G. Hoeks, "Reduction of the clutter component in doppler ultrasound signals based on singular value decomposition: A simulation study," *Ultrasonic Imaging,* vol. 19, no. 1, pp. 1-18, 1997.

[12] C. Demené, T. Deffieux, M. Pernot, B.-F. Osmanski, V. Biran, J.-L. Gennisson, L.-A. Sieu, A. Bergel, S. Franqui, J.-M. Correas, I. Cohen, O. Baud and M. Tanter, "Spatiotemporal Clutter Filtering of Ultrafast Ultrasound Data Highly Increases Doppler Ultrasound Sensitivity," *IEEE TRANSACTIONS ON MEDICAL IMAGING,* vol. 34, no. 11, pp. 2271-2285, 2015.

[13] J. Jensen and N. Svendsen, "Calculation of pressure fields from arbitrarily shaped , apodized, and excited Ultrasound transducers," *IEEE Transactions on Ultrasonics, Ferroelectrics and Frequency Control,* vol. 39, pp. 262-267, 1992.

[14] J. Jensen, "FIeld: A program for simulating Ultrasound systems," *Medical and Biological Engineering and Computing,* vol. 34, pp. 351-353, 1996.

[15] G. Montaldo, M. Tanter, J. Bercoff, N. Benech and M. Fink, "Coherent Plane-Wave Compounding for Very High Frame Rate Ultrasonography and Transient Elastography," *IEEE Transactions on Ultrasonics, Ferroelectrics, and Frequency*

Control, vol. 56, no. 3, pp. 489-506, March 2009.

[16] R. L. Peterson, R. E. Ziemer and D. E. Borth, Introduction to Spread-spectrum Communications, Prentice Hall, 1995.

[17] T. L. Poepping, H. N. Nikolov, M. L. Thorne and D. W. Holdsworth, "A thin-walled carotid vessel phantom for Doppler ultrasound flow studies," *Ultrasound in Medicine and Biology,* vol. 30, pp. 1067-1078, 2004.

[18] K. V. Ramnarine, T. Anderson and P. R. Hoskins, "Construction and geometric stability of physiological flow rate wall-less stenosis phantoms," *Ultrasound in Medecine and Biology ,* vol. 27, no. 2, p. 245–250, 2001.

[19] K. V. Ramnarine, N. D. K., P. R. Hoskins and J. Lubbers, "Validation of a new blood-mimicking fluid for use in Doppler flow test objects," *Ultrasound in Medicine and Biology,* vol. 24, pp. 451-459, 1998.

Chapter 4

4   Chirp based methods for velocity estimation of non-stationary flow in plane-wave color Doppler imaging

The content of this chapter is in early preparation for submission to IEEE Transactions in Ultrasonics, Ferreoelectrics, and Frequency Control, with author list Omar Mansour and James C. Lacefield.

4.1   Introduction

Recent advances in high-frame-rate imaging has enabled continuous and fast acquisition of Doppler slow time samples [1], [2], thereby allowing continuous velocity estimation for color imaging, and simultaneous spectral estimation for spectrogram analysis.

The commonly used intensity-weighted mean frequency (IWMF) method [3] uses short Doppler ensembles representing 2-60 ms time windows for average velocity estimation. The window is then slid with overlap in order to provide high update rates.

Due to the complex nature of ultrasound scattering, ultrasound signals and their corresponding Fourier transforms, which is used in estimating mean velocities, may be modeled as stochastic. Artefacts that increase the spectral bandwidth, such as windowing, intrinsic, and non-stationarity broadenings [4] may thus increase the variance of the estimated mean frequency [3], [5]. Short Doppler ensembles provides high temporal resolution, but may result in higher broadening, and lower signal-to-noise ratio (SNR), whereas long ensembles provide less broadening (and hence less variance) and higher SNR at the expense temporal resolution.

To reduce the effect of short data windows on spectral broadening, parametric spectral estimation methods such as the auto-regressive model [6], and the maximum likelihood (ML) or Capon estimator, were studied by various authors with some degree of success. A good review of those methods was reported in [7] and [8]. Several authors have worked on reducing non-stationarity broadening; an adaptive autoregressive model was

proposed in [9], while a Kalman filter in conjunction with ML estimator was suggested in [10], whereas a stationarizing technique was presented in [11].

Parametric estimation methods attempt to estimate the Doppler spectrum using a predefined model in order to overcome the ultrasound signal's stochastic behavior, and reduce the variance in mean velocity estimates. However, the model order has a large impact on the performance of such methods, and serious issues with the model order selection were reported in [12] and [13].

Our goal is to find a compact frequency representation for the short time windowed, and non-stationary Doppler signal, thereby increasing the frequency resolution and reducing the variance of the mean Doppler velocity estimates. The Fourier transform (FT) is not suitable for time windowed signals since it seeks representation using infinite duration complex sinusoids, whereas the discrete Fourier transform (DFT) uses an orthogonal set of complex sinusoids of limited duration, and hence it best matches sinusoidal signals whose period is integer divisible by the window length. In this paper we propose using chirps for producing compact frequency representations of Doppler signals with the goal of reducing non-stationarity and finite-time-window spectral broadenings, and thus reducing the variance of mean velocity estimates.

In section II-A, we shall use a Doppler signal model based on the one developed by Bastos *et al*. [4] and adapt it for conditions of short time durations and show that under the assumption of constant acceleration within a short time window, the Doppler signal can be represented with a finite number of linearly chirped complex sinusoids. In section 4.2-B, we propose using the chirped Fourier transform (CFT) [14] to overcome the non-stationarity broadening. In section 4.2-C, we expand on this approach and propose the use of a variant of the adaptive Chirplet decomposition [15], [16] using the method of Matching Pursuits [17] to reduce window and non-stationarity broadening. In sections 4.2-D and 4.2-E we present our Field II [18], [19] simulation and experimental setups. In section 4.3, we present Field II simulations and carotid phantom experimental results, followed by a discussion in section 4.4. We expected the method of matching pursuits to do better than the IWMF and CFT based estimates, but instead its velocity estimates had

significantly higher variance. We hypothesize the reason for the higher variance is that the method of matching pursuits uses non-orthogonal functions for decomposing the Doppler ensemble, as opposed to DFT based methods (e.g. IWMF, CFT) that use orthogonal frequency components to compute a weighted. The CFT method however seems to outperform the conventional IWMF in reducing the variance, especially at high acceleration areas of pulsatile flow waveforms. We conclude with a brief review of possible applications, and future improvements in section 4.5.

4.2   Methods

4.2.1   The Doppler signal model

We adopted the signal model proposed by Bastos *et al.* [4] as shown in Fig. 4.1, and then we added the additional constraint of constant acceleration. The following assumptions are used:

- Cardiac pulse wave propagation is fast enough that the velocity is constant over all elemental voxels at any given time snapshot.

- Uniform laminar flow, with no turbulence.

- Beam angle intrinsic broadening is ignored.

- Scatterers are moving in a uniform direction, parallel to the vessel wall.

- Constant acceleration throughout the Doppler ensemble.
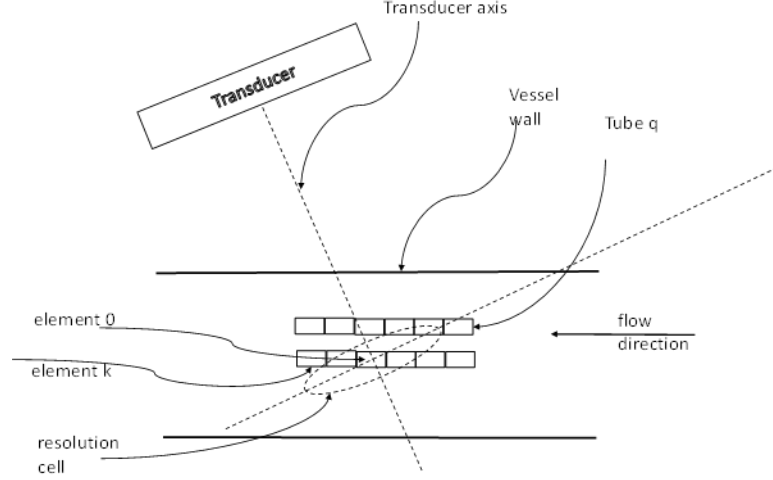
Fig. 4.1: Imaging scene

We visualize the overall fluid volume as a multitude of small elements, each containing a number of red blood cells (RBCs) and moving through the vessel as a single unit throughout the Doppler ensemble time, i.e. velocity and transducer sensitivity do not fluctuate between scatterers of the same element. Also, following Bastos *et al.*, we define an elementary tube as a number of elements with similar velocity as shown in Fig. 4.1.

If at time *t=0*, an element was located at the center of the resolution cell, then the demodulated I/Q signal received from that element may be written as:

$$S_0 = A_0 e^{j\phi_0} g_0(t) e^{j(\omega_0 t + ct^2)} \tag{4.1}$$

where $A_0 e^{j\phi_0}$ is the echo received at *t=0* from that element and is the sum of contributions from all RBCs within the element's volume, ω_0 is the angular frequency, c_0 is half the chirp rate, and the beamforming function $g(x, y, z)$ may be written as a function of time $g_0(t)$ since position x is a function of time $x(t) = v_0t + 0.5at^2$ where v_0 is the velocity at time *t=0* and a is the constant acceleration. Note that in this setup, the y and z coordinates do not change for any of the elements. Additionally, note that if we take a time snapshot, we find that elements within the same elementary tube q shall have the same velocity, since they all have the same radius.

If an element k located at a distance x_k from the center of the cell, then it would reach the cell at time $t = \tau_k$, and by the same token, the demodulated I/Q signal received from that element may be written as:

$$S_k = A_k e^{j\phi_k} g_k(t - \tau_k) e^{j[\omega_k(t-\tau_k) + c(t-\tau_k)^2]} \tag{4.2}$$

where $g_k(t) = g(v_k t + 0.5 a t^2, y, z)$ is the beamforming function at $t = \tau_k$, and v_k and ω_k are the velocity and angular frequency of element k at time $t = \tau_k$ respectively. Under constant acceleration conditions, we can state that

$$v_k = v_0 + a\tau_k, \text{ and} \tag{4.3}$$

$$w_k = w_0 + c\tau_k, \tag{4.4}$$

Eq. (4.2) then becomes:

$$S_k = A_k e^{j\phi_k} e^{-j(\omega_k \tau_k + c\tau_k^2)} g_k(t - \tau_k) e^{j[(\omega_0 - c\tau_k)t + ct^2]}$$

$$= D_k g_k(t - \tau_k) e^{j[(\omega_0 - c\tau_k)t + ct^2]} \tag{4.5}$$

where $D_k = A_k e^{j\phi_k} e^{-\omega_k \tau_k + c\tau_k^2}$. The signal from an elementary tube q can be computed as:

$$S_q = e^{jct^2} \sum_k D_k g_k(t - \tau_k) e^{j(\omega_0 - c\tau_k)t} \tag{4.6}$$

The overall signal will then be the sum of signals from all elementary tubes within the imaging scene. If we adapt Eq. (4.6) to accommodate for variations of velocity and chirp rates between different tubes, then the overall signal from all elementary tubes is:

$$S = \sum_q e^{jc_q t^2} \sum_k D_{qk} g_{qk}(t - \tau_{qk}) e^{j(\omega_{0q} - c\tau_{kq})t} \tag{4.7}$$

Note that if we have a stationary Doppler signal, we can set $c=0$ in Eq. (4.2), and hence Eq. (4.6) becomes:

$$S_q = \sum_k A_k e^{j\phi_k} g_{0q}(t - \tau_k) e^{j\omega_0(t-\tau_k)} \tag{4.8}$$

which is a convolution operation, and the signal represents filtered white random Gaussian noise if we assume the scatterers within elements are totally uncorrelated.

It should be noted that the size of each elementary units will determine the number of components inside the summations in Eqs. (4.6) and (4.7). The size of each element is dictated by the maximum dimensions under which the amplitude and velocity fluctuations within the element are negligible to ensure that scatterers within an elements provide constant relative contributions to A_{qk} as they traverse the beamforming curve, and hence A_{qk} remains constant throughout the observation window. The element size that best models the Doppler signal with the smallest number components is thus expected to vary depending on whether focused or plane-wave excitations are used. Mo and Cobbold [20] hypothesized that an element size of $\lambda/20$ dimensions would properly model the Doppler signal, however their model had the additional constraint of constant phase for scatterers within the elements.

4.2.2 Velocity estimation using the chirped Fourier transform

In plane-wave Doppler imaging (except for the method suggested in [2]), it is common to use a small number of compounding angles [1], in order to keep frame rates high and avoid aliasing. In some cases, a single plane-wave angle is used [21] resulting in low directivity in the transducer's lateral direction. In cases of high beam-to-flow angles, the resolution is high in the z-direction, but low in the x-direction, and hence we expect the Doppler signal to be represented by a small number of tubes and we also expect a small number of elements within each tube q since the sensitivity variation along the x-direction is expected to be low. In those cases, we expect Eq. (4.6) to be a reasonable approximation of the Doppler signal. Additionally, in parabolic flow profiles, the areas close to the middle of the vessel exhibit the highest velocities and slow velocity gradients, whereas the areas close to the vessel wall exhibit low velocities but steep gradients, and are generally weak due to wall filtering, which further strengthens the argument that Eq. (4.6) should generally be a valid approximation under constant acceleration conditions.

In Eq. (4.6), the Doppler signal is formed of multiple discrete windowed frequency components, all multiplied by a single chirp, and hence exhibiting non-stationarity broadening.

In this method, we propose using the chirped Fourier transform (CFT) [14] to reduce the spectral broadening. The CFT is a variant of the Fractional Fourier Transform and is computed by applying the Fourier Transform (FT) after multiplying the signal by a chirp with a chirp-rate $2c$. The CFT does not change the central frequency nor the total power of a signal. The CFT of a Doppler signal $x(n)$ of length N is defined as:

$$X_c(f) = \sum_{n=-N/2}^{N/2-1} x(n)e^{-j2\pi(ft+ct^2)} \qquad (4.9)$$

where f is the frequency, $2c$ is the chirp-rate, $t=nT_s=n/FR$ and FR is the frame rate, which is also the Doppler sampling rate. Eq. (4.9) indicates that to compute signal's CFT, we pre-multiply by a chirp $e^{-j2\pi ct^2}$ and then compute the FT as usual. We search for the best chirp-rate parameter c using an optimization algorithm that minimizes the CFT's bandwidth, which we measure as the second moment of the signal's power spectral density. After determining the optimized chirp-rate, we use it for computing the central frequency using the first moment of the CFT. Our actual implementation uses the Kasai method [22] for computing both the bandwidth and the central frequency of the chirped signal. The chirp rate is searched in two steps:

- In the first step, the maximum and minimum values of c are determined such that:

$$c = [-C_{min}, C_{max}] = [-\frac{FR}{T}, \frac{FR}{T}] \qquad (4.10)$$

where $T=NT_s$, hence the maximum chirp-rate is chosen such that the chirp is not aliased within the ensemble window as in [16]. A discrete set of chirps are constructed, with chirp rates equally spaced within the range determined in Eq. (4.10). The number of chirps was empirically chosen to be 64 in our implementation. The input Doppler signal is multiplied by each chirp in the set forming a chirped signal, and the bandwidth is computed as in [22]:

$$BW(c) = \frac{FR}{2\pi} \sqrt{1 - \frac{|R_1|}{R_0}} \qquad (4.11)$$

where R_0 and R_1 are the lag-0 and lag-1 autocorrelation functions of the chirped Doppler signal respectively. The chirp-rate parameter yielding the minimum bandwidth C_1 is chosen.

- Constrained optimization is performed using the interior-point algorithm, with C_1 as the starting point, its adjacent entries in the set chosen as the upper and lower bounds, and the objective function as defined in Eq. (4.11).

After determining the optimized chirp-rate parameter C_{opt}, the Doppler ensemble is multiplied by the corresponding chirp, i.e. $e^{-j2\pi c_{opt}t^2}$, and the average frequency is computed as in [22] as:

$$f_{mean} = \frac{FR}{2\pi} \cdot phase(R_1) \qquad (4.12)$$

It has been shown by [14] that the CFT does not change the central frequency of the power of the signal.

4.2.3   Velocity estimation using Chirplet pursuits

As described in the introduction, a compact frequency representation of the Doppler signal improves frequency estimation accuracy and reduces the estimate's variance. It can be achieved using longer observation time window, at the expense of temporal resolution. This is true when Fourier Transform (FT) based methods are used, but other means such as parametric estimation have been developed to counter this compromise.

If the signal's time duration is T, and the Discrete Fourier Transform (DFT) is computed using the same duration, then the resulting frequency bins are separated by $1/T$, and if the signal's frequency is a multiple of $1/T$, then it will be represented by a single DFT coefficient. However, if the signal's frequency lies between two DFT bins, its DFT coefficients will be spread over multiple bins. Attempting to increase the DFT's duration via zero-padding will not help since the basis functions are now longer than the signal's

duration, and it will take many such sinusoids to compensate for the duration mismatch. In the extreme case, the FT seeks to use sinusoidal bases of infinite duration.

The Doppler signal in Eq. (4.7) may exhibit a large number of components, each with a random magnitude, depending on the slope of the beamforming function and the flow profile, but one would expect a discrete number of chirp-rates and central frequencies, and to have a compact representation of such signal, decomposition into a dictionary of normalized functions that match the signal components in frequency and chirp rates needs to be used. Since the signal components may not be orthogonal, then we would expect these normalized functions not to be orthogonal either, and the same can be stated for linear independence. Hence, unlike the DFT, the set of these functions doesn't constitute a basis. Such normalized elementary functions are referred to as atoms and the set of all atoms used is referred to as a dictionary [17].

A solution to this time-frequency resolution problem has been previously proposed by Mann and Haykin with the aid of an adaptive Chirplet decomposition [15] utilizing eight Chirplet parameters, and an Expectation-Maximization technique for finding the best fitting atoms. Bultan [16] used four parameters and the method of matching pursuits for decomposing similar signals.

For Adaptive decomposition to be efficient and converge in a few number of iterations, it is required that the signal of interest have a few dominant components, but due to the possibility of large number of chirped and time shifted components existing in Eq. (4.7), we took the approach of lumping all components of the same frequency/chirp-rate pair into a single atom that has the full duration of the Doppler ensemble. As a result, our proposed method employs Chirplet decompositions with two parameters; the central frequency and chirp-rate.

The dictionary of Chirplet atoms is constructed such that each atom has the full duration of the Doppler ensemble, NT_s, where N is the number of samples and T_s is the Doppler sampling period. All atoms have zero time shift and hence are all centered around $t=0$ time. Hence each atom is of the form:

$$g(f, c) = e^{j2\pi(ft + ct^2)} \tag{4.13}$$

where f is the frequency, and c is half the chirp-rate, $t=nT_s$, and n is the sample number within the Doppler ensemble and spans the range *[-N/2, N/2-1]*. Note that f and c are allowed to assume any Real value.

Decomposing the signal ensemble into the proposed dictionary is achieved using the method of Matching Pursuits [17]. Multiple iterations are performed such that at each iteration k, the best matching atom g_k is selected as the one atom that resulted in maximizing the correlation with the residual signal at that iteration. The residue is thus computed as

$$R^{k+1} = R^k - < R^k, g_k > g_k \tag{4.14}$$

where R^k is the residue from iteration k, R^0 is the original Doppler ensemble and $< >$ denotes the inner product. The next iteration proceeds using the residue from the previous iteration, and process ends either after a predefined number of iterations, or when the remaining residue's power is a certain fraction of the initial signal power.

At each iteration, the optimum selection atom g_k is performed in two steps just as in the previous section; First, a smaller, discrete subset of the dictionary is constructed (i.e. hence f and c are limited to discrete values), the correlation between each of the atoms and the Doppler ensemble is computed and tabulated and the maximum atom g_{1k} producing the maximum correlation with the residue is chosen. The selection of the discrete dictionary is derived in [16]

In the second step, constrained optimization is performed using the interior-point algorithm, with $g_{1k}'s$ index parameters f and c used as the starting point, its adjacent indices in the discrete dictionary subset chosen as the upper and lower bounds, and the objective function being the value of the correlation of a normalized chirp with the residue.

After decomposing the Doppler ensemble, the velocity is estimated as the power weighted sum of the component atoms' velocities. Since the atoms are normalized to unit

power, then the square of the coefficients represents the power in each component. In a way this is similar to the FFT based methods (e.g. the Kasai implementation) that use the first moment in the power spectral density domain, which is essentially a power weighted averaging of each sinusoidal component's frequency.

4.2.4   Field II Simulations

We produced synthetic images using Field II [18], [19] with the parameters shown in Table 4.1. We have simulated a very narrow wall-less vessel, with no surrounding tissue to save on simulation time and to serve a simple case for proof of concept. Additionally, we only simulated with a single plane-wave angle, since this is a common setup with plane-wave imaging of high flow rates, and also to save on the simulation time. The Scatterers were initially randomly placed and then moved according to the pulsatile flow waveform. The simulation used the matlab parallel processing toolbox.

Receive beamforming was applied to the RF lines resulting from the field simulations, and the resulting frames were quadrature demodulated to produce I/Q samples forming the Doppler ensembles. No wall filtering was performed.

For statistical analysis, we used samples corresponding to the same vessel radius to compute the mean and standard deviation of velocity, bandwidth, and chirp-rate. This was repeated for each Doppler ensemble with the ensemble's central time point displayed for each metric.

Table 4.1: Field II simulation parameters

Number of Scatterers per resolution cell	10	Element Pitch	0.472 mm
Frame rate	3 kHz	Element kerf	0.025 mm
Excitation frequency	5 MHz	Element height	4 mm
Number of cycles per pulse	2	Velocity waveform	Sinusoidal

Number of compounded plane waves	1	Waveform frequency	5 and 10 Hz
Total number of firings	1024	Flow profile	plug
Transducer type	Linear	Maximum velocity v_0	400 mm/s
Number of elements	64	Vessel diameter	1 mm

4.2.5   Flow Phantom Experiments

Experiments were performed using a custom carotid artery flow phantom [23]. The common carotid segment, which was imaged in this study, consisted of an 8-mm inner diameter and a 1-mm thick polydimethylsiloxane vessel wall surrounded by tissue-mimicking material [24]. Pulsatile flow of the blood-mimicking fluid [25], prepared in house, was controlled using a Compuflow1000 precision pump (Shelley Medical Imaging Technologies, London, ON) programmed with a carotid artery waveform with update rate of 2 ms. A Sonix RP scanner (Ultrasonix Inc., Richmond, BC), equipped with a Sonix DAQ data acquisition module and a 60-mm, 128-element linear-array transducer (L14-5W/60) was used to acquire pre-beamformed channel data sampled at 40 MHz with 12-bit quantization.

A longitudinal view of the phantom's common carotid artery was imaged using a 5 MHz center frequency, 2-cycle transmit pulse, and a 15 kHz PRF. The transducer was oriented so the long axis of the vessel formed a 19.5° angle with the lateral dimension of the image. Post processing was performed using MATLAB (version R2015b, The MathWorks, Inc., Natick, MA).

Seventeen plane-wave tilt angles were used to acquire low-resolution RF image frames, by stepping through the transmit steering angles in ascending order. Receive beamforming was applied to those frames, and the resulting images were compounded to produce a high-resolution image (HRI) frame. Multiple HRI frames were constructed by repeating this procedure. The HRI image frames were quadrature demodulated to produce I/Q samples forming the Doppler ensembles, and then wall filtering was applied.

For statistical analysis, we used samples corresponding to the same vessel radius to compute the mean and standard deviation of velocity, bandwidth, and chirp-rate. This was repeated for each Doppler ensemble with the ensemble's central time point displayed for each metric.

4.3 Results

The goal of the Field II simulations was a proof of concept, and hence a simple setup was used to eliminate all the unknown variables. Fig. 4.2 shows Field II simulations results for the three different methods; The Kasai, the chirped Kasai, and the Chirplet pursuits methods. The 15 Hz sinusoidal velocity waveform had a corresponding peak Doppler frequency of 450 Hz. Fig. 4.2a and Fig. 4.2b which is a zoom-in version of Fig. 4.2a, demonstrate improved velocity accuracy of Chirplet pursuits method. Fig. 4.2c and Fig. 4.2d which is a zoomed-in version of Fig. 4.2c demonstrate the improved standard deviation in the chirped Kasai and the Chirplet pursuits methods. Using Fig. 4.2b and Fig. 4.2d, it can be observed that the velocity standard deviations of the Kasai method is highest at the fast edges, while the standard deviation in the chirped Kasai method is highest at the waveform's peaks. Fig. 4.2e demonstrates how the bandwidth is reduced when using the chirped Kasai method as compared to the standard Kasai. Fig. 4.2f demonstrates the feasibility of measuring the chirp-rate using Chirplet pursuits and the chirped Kasai methods. It can be observed how the measured chirp-rate is also sinusoidal, but phase shifted from the actual velocity waveform. Also it can be seen in Fig. 4.2f that the chirped Kasai provides a less noisy chirp-rate estimate.

A carotid phantom experiment was conducted to evaluate the performance of the three methods under low velocity slope conditions. Fig. 4.3 shows the data acquired using a 5

Hz sinusoidal waveform with a peak flow of 5 mL/s, which corresponds to a peak Doppler frequency shift of 433 Hz. A 30 Hz wall filter was applied in this experiment. Fig. 4.3(a-d) demonstrates that the Kasai and chirped Kasai perform in an equal manner under low acceleration conditions, with the exception of a few glitches on the chirped Kasai method, which we have identified to be due to actual glitches on the signal. Fig. 4.3e shows that under low acceleration conditions, the bandwidth is not reduced in the chirped Kasai method. Fig. 4.3f demonstrates the feasibility of properly measuring the acceleration, albeit with high noise in the Chirplet pursuits method.

In Fig. 4.4, the same phantom was driven with pulsatile carotid waveform [26] with 10 mL/s flow peak flow rate. Since the frame rate used was 888 Hz, velocity wrapping has been performed. A 100 Hz wall filter was deployed, which reduced the maximum and minimum measurable velocities. As compared to the previous test, this experiment demonstrates the behavior under high acceleration. Fig. 4.4a and Fig. 4.4b show the measured velocity waveforms for the three methods for Doppler ensemble sizes of 54.4 ms and 74.5 ms respectively. Fig. 4.4c and Fig. 4.4d show the standard deviation in the estimated velocities. The important point to note is the much reduced standard deviation at the high slope area in the curve in the chirped Kasai as compared to the Kasai method. This is in line with our expectations since the method shows the most value at areas of high acceleration. At other areas of the waveform, the chirped Kasai and the Kasai look similar, with the exception of a couple of outliers that were due to strong glitches on the actual Doppler time domain waveform. This indicates the chirped Kasai method might be more susceptible to artefacts. Alternatively, one may argue that it is more sensitive to fast changing events. Fig. 4.4 (a) and (b) demonstrate the improved accuracy of the Chirplet pursuits method, however the authors believe its high variance renders it unusable.
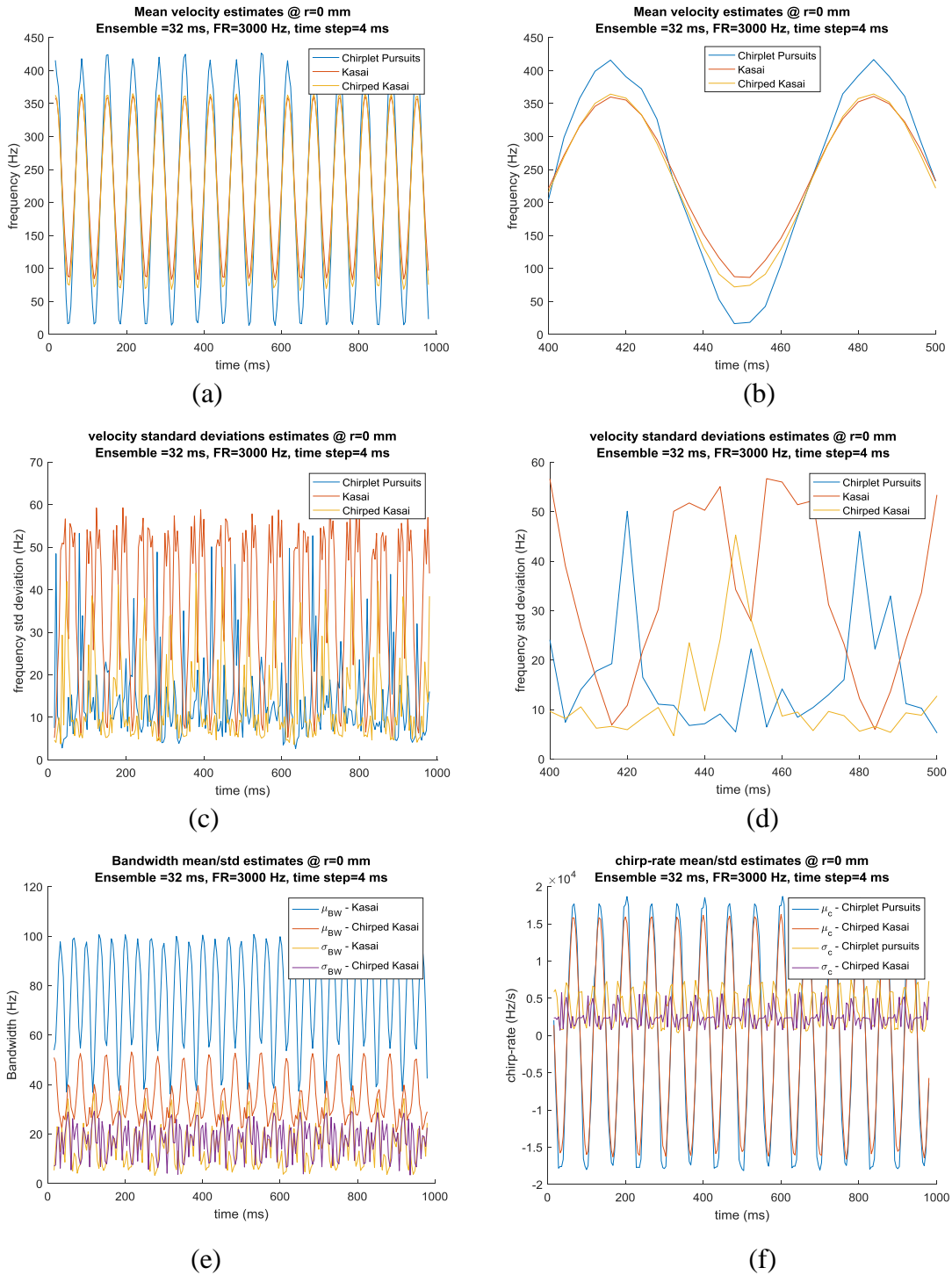
Fig. 4.2: Field II simulations: sinusoidal wave-form with peak velocity corresponding to 450 Hz. (a) and (b) demonstrate the mean velocity accuracy for three different methods; Kasai, chirped Kasai, and Chirplet pursuits, (c) and (d) demonstrate the standard deviation in velocity measurements, (e) demonstrates the measured bandwidth, and (f) demonstrates the measured chirp-rate.

Fig. 4.3: Carotid phantom experiment - vessel diameter=8 mm, 19.5^0 inclination, sinusoidal wave-form with peak velocity corresponding to 433 Hz. (a) and (b) demonstrate the mean velocity accuracy for three different methods; Kasai, chirped Kasai, and Chirplet pursuits, (c) and (d) demonstrate the standard deviation in velocity measurements, (e) demonstrates the measured bandwidth, and (f) demonstrates the measured chirp-rate.
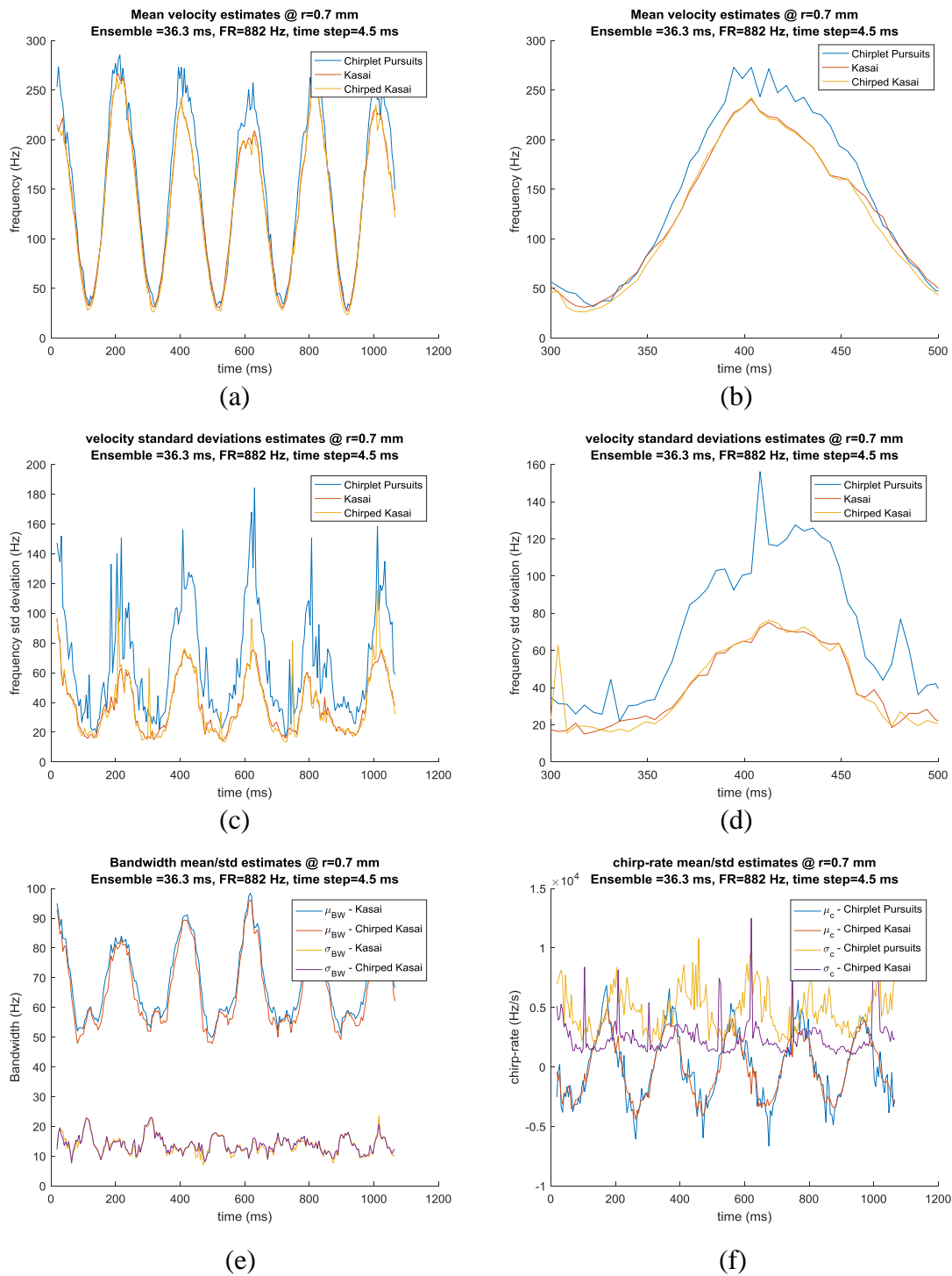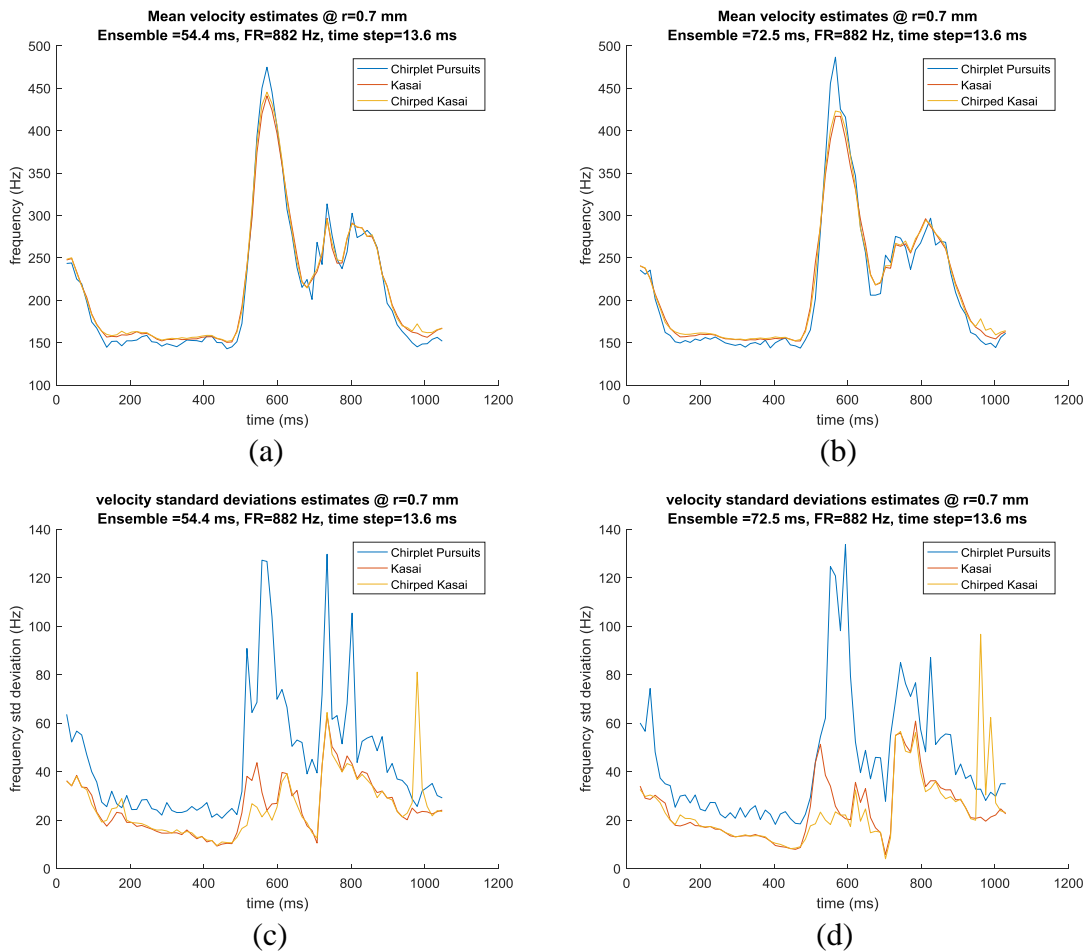
Fig. 4.4: Carotid phantom experiment - vessel diameter=8 mm, 19.5^0 inclination, carotid wave-form with peak velocity corresponding to 866 Hz. (a) and (b) demonstrate the mean velocity accuracy for three different methods; Kasai, chirped Kasai, and Chirplet pursuits, (c) and (d) demonstrate the standard deviation in velocity measurements.

4.4 Discussion

Our initial intuition was that since the Chirplet pursuits method decomposes the Doppler signal compactly, the velocity variance would be reduced, particularly at the high acceleration area of a pulsatile waveform, and this was supported by the Field II study. In lab experiments however, this was proven not to be true and the variance was actually significantly worse. We hypothesize that this is due to the fact that the MP method is nonlinear and its components are not orthogonal which may negatively affect the performance of power weighted velocity averaging. As a consequence, we developed the CFT method, which is similar to FFT based techniques in the sense that an orthogonal

basis is used in computing the weighted average velocity, but it performed better than FFT methods (Kasai) at areas of high acceleration in a pulsatile flow waveforms, particularly when the length of the Doppler ensemble and chirp-rates are large enough to cause non-stationarity broadening.

The CFT method may be visualized as a de-stationarizing technique, but it differs from the one proposed in [11] in that it acts globally on an entire Doppler ensemble and applies to it a single chirp-rate.

An area where the CFT method does not provide the full benefit is at the peaks of the carotid velocity waveform, when there is a rapid rate of acceleration since a linear chirp then becomes inadequate. For this, we believe a quadratic chirp should allow the detection of the waveform peak while using long Doppler ensembles, and hence lower variance. This however will require a two parameters optimization for finding the best chirp and rate of chirping.

The CFT method can be used in combination with other high resolution methods such parametric estimation (e.g. AR, MA, and ARMA models), or variance reduction methods (e.g. Welsh method) since it does not shift the central frequency, and since the CFT has all the properties of the FT.

A benefit in the CFT method is availability of acceleration measurements, which opens the door to well behaved Kalman filtering thereby reducing velocity estimation variance, a benefit that was not previously possible.

4.5 Conclusions

Two chirp based methods have been presented, with one, the CFT, having excellent potential for future development. Experimental data showed that the CFT method reduces variance at the high acceleration phase in the carotid waveform. We acknowledge however that only a few experiments were performed, and more experiments to statistically validate the method under different test conditions such as flow rates, vessel-to-beam angles, transmit frequency, vessel diameters, etc.

The CFT method can benefit from further development to allow the use of quadratic chirps.

The availability of estimated acceleration opens the door to Kalman filtering, which should reduce velocity measurement errors even further.

References

[1]   J. Bercoff, G. Montaldo, T. Loupas, D. Savery, F. M'ezi'ere, M. Fink and M. Tanter, "Ultrafast compound Doppler imaging: Providing full blood flow characterization"," *IEEE Transactions on Ultrasonics, Ferroelectrics, and Frequency Control,* vol. 58, pp. 134-147, 2011.

[2]   O. Mansour, T. L. Poepping and J. C. Lacefield, "Spread-Spectrum Beamforming and Clutter Filtering for Plane-Wave Color Doppler Imaging," *IEEE Transactions on Ultrasonics, Ferroelectrics, and Frequency Control,* vol. 63, no. 11, pp. 1865 - 1877, 2016.

[3]   B. Angelsen, "Instantaneous frequency, mean frequency, and variance of mean frequency estimators for ultrasound blood velocity Doppler signals," *IEEE Transcations on Biomedical Engineering,* vol. 28, pp. 733-741, 1981.

[4]   C. A. C. Bastos, P. J. Fish and F. Vaz, "Spectrum of Doppler Ultrasound Signals from Nonstationary Blood Flow," *ieee transactions on ultrasonics, ferroelectrics, and frequency control,,* vol. vol. 46, no. 5, pp. 1201-1217, 1999.

[5]   R. Willink and D. H. Evans, "Statistical bias and variance in blood flow estimatin by spectral analysis of Doppler signals," *Ultrasound in Medicine and Biology,* vol. 21, pp. 919-935, 1995.

[6]   S. M. Kay and S. L. Marple, "Spectrum analysis - a modern perspective," *Proceedings of the IEEE,* vol. 69, no. 11, pp. 1380-1419, 1981.

[7]   P. Vaitkus and R. Cobbold, "A Comparative study and assessment of Doppler ultrasound spectral estimation techniques Part I: Estimation methods.," *Ultrasound in Medicine and Biology,* vol. 14, pp. 661-672, 1988.

[8]   P. Vaitkus and R. Cobbold, "A comparative study and assessment of Doppler ultrasound spectral estimation techniques. Part II: Methods and results.," *Ultrasound in Medicine and Biology,* vol. 14, pp. 673-688, 1988.

[9]   A. Herment and J. Giovannelli, "An adaptive approach to computing the spectrum and mean frequency of Doppler signals," *Ultrasonics Imaging,* vol. 17, pp. 1-26, 1995.

[10] H. Talhami and K. R.I., "Maximum likelihood frequency tracking of audio pulsed Doppler ultrasound signal using a kalman filter," *Ultrasound in Medicine and Biology,* vol. 14, pp. 599-609, 1988.

[11] Y. Wang and P. J. Fish, "Correction for Nonstationarity and Window Broadening in Doppler Spectrum Estimation," *IEEE SIGNAL PROCESSING LETTERS,* vol. 4, no. 1, pp. 18-20, 1997.

[12] K. Kaluzynski, "Order selection in Doppler blood flow signal spectral analysis using autoregressive modelling.," *Med. Biol. Eng. Comput.,* vol. 27, pp. 89-92, 1989.

[13] F. Shlindwein and D. Evans, "Selection of the order of autoregressive models for spectral analysis of Doppler ultrasound signals," *Ultrasound in medicie and biology,* vol. 16, pp. 81-91, 1990.

[14] P. White and J. Locke, "Performance of Methods based on the fractional Fourier transform for the detection of linear frequency modulated signals," *IET Signal Processing,* vol. 6, no. 5, pp. 478-483, 2012.

[15] S. Mann and S. Haykin, "Adaptive "chirplet" transform: an adaptive generalization

of the wavelet transform," *Optical Engineering,* vol. 31, no. 6, pp. 1243-1256, 1992.

[16] A. Bultan, "A four-parameter atomic decomposition of chirplets," *IEEE Transactions on Signal Processing,* vol. 47, no. 3, pp. 731-745, 1999.

[17] S. G. Mallat and Z. Zhang, "Matching Pursuits With Time-Frequency Dictionaries," *IEEE Transactions on Signal Processing,* vol. 41, no. 12, pp. 3397-3415, 1993.

[18] J. Jensen, "FIeld: A program for simulating Ultrasound systems," *Medical and Biological Engineering and Computing,* vol. 34, pp. 351-353, 1996.

[19] J. Jensen and N. Svendsen, "Calculation of pressure fields from arbitrarily shaped , apodized, and excited Ultrasound transducers," *IEEE Transactions on Ultrasonics, Ferroelectrics and Frequency Control,* vol. 39, pp. 262-267, 1992.

[20] L. Y. L. Mo and R. S. C. Cobbold, "A unified approach to modeling the backscattered Doppler ultrasound from blood," *IEEE Transactions on Biomedical Engineering,* vol. 39, no. 5, pp. 450-461, 1992.

[21] B.-F. Osmanski, D. Maresca, E. Messas, M. Tanter and M. Pernot, "Transthoracic Ultrafast Doppler Imaging of Human Left Ventricular Hemodynamic Function," *IEEE TransacTIons on Ultrasound, Ferroelectrics, and Frequency Control,* vol. 61, no. 8, pp. 1268-1275, 2014.

[22] C. Kasai, K. Namekawa, A. Koyano and R. Omoto, "Real-time two-dimensional blood flow imaging using an autocorrelation technique," *IEEE Transactions on Sonics and Ultrasonics,* Vols. SU-32, no. 3, pp. 458-464, 1985.

[23] T. L. Poepping, H. N. Nikolov, M. L. Thorne and D. W. Holdsworth, "A thin-walled carotid vessel phantom for Doppler ultrasound flow studies," *Ultrasound in Medicine and Biology,* vol. 30, pp. 1067-1078, 2004.

[24] K. V. Ramnarine, T. Anderson and P. R. Hoskins, "Construction and geometric

stability of physiological flow rate wall-less stenosis phantoms," *Ultrasound in Medecine and Biology ,* vol. 27, no. 2, p. 245–250, 2001.

[25] K. V. Ramnarine, N. D. K., P. R. Hoskins and J. Lubbers, "Validation of a new blood-mimicking fluid for use in Doppler flow test objects," *Ultrasound in Medicine and Biology,* vol. 24, pp. 451-459, 1998.

[26] D. Holdsworth, C. Norley, R. Frayne, D. Steinman and B. Rutt, "Characterization of common carotid artery blood-flow waveforms in normal human subjects," *Physiol. Meas.,* vol. 20, pp. 219-240, 1999.

Chapter 5

5   Conclusions and future directions

5.1   Summary

In chapter 2, we presented the spread-spectrum method for high-frame-rate color Doppler imaging. The method is capable of producing high-spatial-resolution images that also have high unaliased Doppler frequency limit. The proposed method employs a random sequence of plane-wave transmit steering angles, which was shown to distribute the out-of-cell clutter signal power across the entire Doppler spectrum, thereby suppressing it and alleviating the need for compounding. Experimental results obtained from a carotid artery flow phantom demonstrate that the spread-spectrum method eliminates the tradeoff between beam quality, Doppler aliasing, and frame rate that is encountered in current plane-wave Doppler methods. The spread-spectrum method is expected to be valuable for applications that demand imaging of high velocities at high temporal resolution and may also be applicable to synthetic aperture imaging methods.

The spread-spectrum method sufficiently suppresses out-of-cell blood echoes to achieve high spatial resolution, but spread-spectrum suppression is not adequate for wall clutter which may be 60 dB above blood echoes [1]. Thus we implemented the RCF filter, which was based on reordering data samples to convert the acquired signals from a time-ordered sequence into a tilt angle-ordered signal, thereby spectrally compacting the clutter echoes and spreading the in-cell echoes. The RCF method then used thresholds in the frequency domain of the angle-ordered signal to remove large compact spectral lines, thereby suppressing clutter, and finally re-ordering the samples back to form the time-ordered, clutter-filtered Doppler ensemble.

The RCF method performed well with wall clutter, which manifested itself in the angle-ordered Fourier spectrum as discrete peaks and was easy to remove with thresholding, but did not fully suppress tissue clutter since it was spread over the angle-ordered spectrum.

In chapter 3, an improved stationary clutter filter for the spread-spectrum Doppler method is proposed, and it has been shown to significantly improve wall and tissue clutter rejection as compared to the original method. The method uses a segmented plane-wave tilt angle sweep plan for spread-spectrum Doppler beamforming, and a periodic reshuffling clutter filter (PRCF) for suppressing all types of stationary echoes such as vessel wall or tissue clutter. The PRCF method used a random sequence of plane-wave tilt angles to form a Doppler ensemble, but it divides the sequence into smaller segments, all using the same set of tilt angles, but each with its own unique random sub-sequence. As a result, the angle-ordered ensemble of stationary signals is periodic and occupies discrete spectral components at well-defined locations, which can be cleared without the need for thresholds or threshold calibration. The suppression of discrete spectral components minimally affects the in-cell or blood Doppler signal since it is spread over the entire angle-ordered spectrum.

Field II simulations showed excellent clutter rejection. Flow phantom experiments showed improved performance over the original RCF method, but indicate the need to address possible hardware limitations that are not accounted for.

Due to the complex nature of ultrasound scattering, ultrasound signals and their corresponding Fourier transforms, which is used in estimating mean velocities, may be modeled as stochastic. Artefacts that increase the spectral bandwidth, such as windowing, intrinsic, and non-stationarity broadenings may thus increase the variance of the estimated mean frequency [2], [3]. In chapter 4, two chirp based methods have been presented to reduce the windowing and non-stationarity broadening in Doppler signals, with one, the CFT, having excellent potential for future development. Experimental data showed that the CFT method was capable of reducing the mean velocity variance at the high acceleration phase in a typical carotid waveform [4].

5.1.1   Limitations of the spread-spectrum method

Even though Field II simulations showed excellent clutter performance for the second version of the spread-spectrum method, which uses the periodic reshuffling clutter filter presented in chapter 3, lab experiments showed clutter rejection performance that is not

in par with conventional linear sweep techniques that uses frame compounding. In chapter 3, we hypothesized that this may be due to the hardware causing some RF offset levels that differ depending on the sequence of the tilt angle sweep, thus causing echoes from the same stationary object to appear non-stationary and hence not fully removed by the clutter filter. Further work needs to be performed to pin-point the root cause of this issue.

The spread-spectrum method is not designed to address non-stationary tissue or vessel-wall clutter in its current implementation, and further work needs to be done to address this issue, as outlined in section 5.2.1.

The lack of real-time implementation is partly due to the low data rates supported by the USB2.0 uplink between the data acquisition module (Ultrasonix DAQ) and the PC. Availability of a high-speed uplink, as well as high performance computing resources such as graphics processing units (GPU) or field programmable gate-arrays (FPGA) should allow real-time implementation of the spread-spectrum method, since the only major overheads added by the method are the 512-point fast Fourier transforms and inverse fast Fourier transforms processed for each pixel.

In vivo studies, which the method currently lacks, may be enabled by the real-time implementation, and may facilitate the method's wide adoption.

5.1.2   Limitations of the chirp-based methods

The chirp-based mean velocity estimation methods presented in chapter 4 may benefit from adapting the constant acceleration model to a constant jerk model, which shall allow reduction in non-stationarity broadening at the peaks of the velocity waveform, where the slope (acceleration) changes from positive to negative. This addition shall allow the method to reduce non-stationarity broadenings throughout the entire cardiac waveform or cycle.

In addition, the method only addresses spectral broadening due to non-stationarity, i.e. change in Doppler frequency resulting from non-constant flow velocity, but does not address finite observation time or intrinsic spectral broadenings.

Although the proposed methods reduced the spectral non-stationarity broadening, occasional glitches in estimated velocities have been seen and need to be addressed in future work.

5.2 Future directions

Extending the PRCF method to address non-stationary clutter shall enhance its value for the anticipated clinical applications of spread-spectrum Doppler that demand high spatial resolution of high velocities such as heart chambers, aortic arch, or stenosis and turbulence detection in the carotid and other large vessels as stated in section 3.4. The CFT method may benefit from expanding the linear chirp/constant acceleration model to a quadratic chirp/constant jerk model that is capable of reducing spectral broadening at the peak velocity region within the cardiac waveform. The following are a few possibilities for future research;

5.2.1 Real-time implementation of the spread-spectrum method for clinical evaluation

As previously mentioned, the spread-spectrum method has been demonstrated in phantom experiments, but for the method to be widely adopted, its diagnostic value needs to be demonstrated in a clinical setup. This requires that the current implementation of the clutter filter be adapted to address non-stationary clutter, and for the system to process images in real-time in order to provide immediate feedback to the sonographer and allow storage of large number of cardiac cycles for further statistical evaluation. Adapting the clutter filter to non-stationary clutter may be achieved by using a method similar to the down-mixing filter [5], whereas real-time implementation may be achieved by using standard data acquisition modules, combined with a generic FPGA board for pulse generation and acquisition control. Further downstream processing may be implemented using high performance GPUs.

5.2.2 Adapting the spread-spectrum method for high-frame-rate Doppler cardiac imaging using synthetic transmit aperture

Synthetic transmit aperture (STA) imaging [6] has been gaining popularity recently due to its higher field of view which makes it suitable for cardiac Doppler imaging. One

downside in STA is the compromise that exists between beam resolution, frame-rate, and maximum unaliased Velocity limit, which limits its applicability to cardiac Doppler imaging where high flows exist at high frame-rates. Adapting the spread-spectrum method to synthetic transmit aperture imaging shall allow Doppler frame-rates as high as the PRF without sacrificing spatial resolution. Another issue in cardiac imaging is the low PRF rates allowed due to the increased imaging depth, which may thus cause Doppler aliasing. For example; a 15 cm imaging depth requires a PRF smaller than 5 kHz, which results in a maximum unaliased Doppler velocity of 37 cm/s, whereas blood velocities may exceed that range in many locations within the heart (e.g. 100 cm/s within the mitral valve [7]). Overcoming both aforementioned limitations may require combining the spread-spectrum method with a de-aliasing technique such as that proposed by posada et al [8], thus enabling the acquisition of spectral Doppler waveforms at every pixel within the field of view, in parallel with tissue Doppler and b-mode acquisitions. This is in contrast with conventional spectral Doppler methods which are only capable of acquiring spectral Doppler waveforms from one small region at a time. Spectral Doppler has been widely used in assessing abnormalities in mitral valve inflow, pulmonary vein inflow, intra-ventricular flow , etc [7], and simultaneously evaluating multiple locations shortens the exam time, reduces the Doppler region selection overhead, and reduces user variability and errors.

References

[1] A. Heimdal and H. Torp, "Ultrasound Doppler measurements of low blood flow: Limitations due to clutter signals from vibrating muscles," *IEEE Transactions on Ultrasonics, Ferroelectrics, and Frequency Control,* vol. 44, no. 4, pp. 873-881, 1997.

[2] B. Angelsen, "Instantaneous frequency, mean frequency, and variance of mean frequency estimators for ultrasound blood velocity Doppler signals," *IEEE Transcations on Biomedical Engineering,* vol. 28, pp. 733-741, 1981.

[3] R. Willink and D. H. Evans, "Statistical bias and variance in blood flow estimatin by spectral analysis of Doppler signals," *Ultrasound in Medicine and Biology,* vol. 21, pp. 919-935, 1995.

[4] D. Holdsworth, C. Norley, R. Frayne, D. Steinman and B. Rutt, "Characterization of common carotid artery blood-flow waveforms in normal human subjects," *Physiol. Meas.,* vol. 20, pp. 219-240, 1999.

[5] S. Bjærum, H. Torp, and K. Kristoffersen, "Clutter Filters Adapted to Tissue Motion in Ultrasound Color Flow Imaging", *IEEE Transaction on Ultrasonics, Ferroelectrics and Frequency Control*, vol. 49, no. 6, pp. 693-704, 2002.

[6] A. Jensen, S. I. Nikolov, K. L. Gammelmark and M. H. Pedersen, "Synthetic aperture ultrasound imaging," *Ultrasonics,* vol. 44, pp. e5-e15, 2006.

[7] S. F. Nagueh, C. P. Appleton, T. C. Gillebert, P. N. Marino, J. K. Oh, O. A. Smiseth, A. D. Waggoner, F. A. Flachskampf, P. A. Pellikka and A. Evangelisa, "Recommendations for the evaluation of left ventricular diastolic function by echocardiography," *European journal of echocardiography,* vol. 10, pp. 165-193, 2009.

[8] D. Posada, J. Porée, A. Pellissier, B. Chayer, F. Tournoux, G. Cloutier and D. Garcia, "Staggered multiple-PRF ultrafast color Doppler," *IEEE Transactions on Medical Imaging,* vol. 35, no. 6, pp. 1510-1521, 2016.

Appendices

Appendix A: IEEE Copyright Agreements

The IEEE does not require individuals working on a thesis to obtain a formal reuse license however, you must follow the requirements listed below:

Textual Material

Using short quotes or referring to the work within these papers) users must give full credit to the original source (author, paper, publication) followed by the IEEE copyright line c [Year of publication] IEEE.

In the case of illustrations or tabular material, we require that the copyright line © [Year of original publication] IEEE appear prominently with each reprinted figure and/or table. If a substantial portion of the original paper is to be used, and if you are not the senior author, also obtain the senior author's approval.

Full-Text Article

If you are using the entire IEEE copyright owned article, the following IEEE copyright/ credit notice should be placed prominently in the references: © [year of original publication] IEEE. Reprinted, with permission, from [author names, paper title, IEEE publication title, and month/year of publication]

Only the accepted version of an IEEE copyrighted paper can be used when posting the paper or your thesis on-line. You may not use the final published version

In placing the thesis on the author's university website, please display the following message in a prominent place on the website: In reference to IEEE copyrighted material which is used with permission in this thesis, the IEEE does not endorse any of [university/educational entity's name goes here]'s products or services. Internal or personal use of this material is permitted. If interested in reprinting/republishing IEEE copyrighted material for advertising or promotional purposes or for creating new collective works for resale or redistribution, please go to

http://www.ieee.org/publications_standards/publications/ rights/rights_link.html to learn how to obtain a License from RightsLink.

If applicable, University Microfilms and/or ProQuest Library, or the Archives of Canada may supply single copies of the dissertation.

Curriculum Vitae

Name: **Omar Mansour**

Post-secondary Education and Degrees:

Ain Shams University
Cairo, Egypt
1989-1993 B.Sc.

University of South Florida
Tampa, FL, USA
1997-1999 M.Sc.

University of Southern California
Los Angeles, CA, USA
2010-2012 M.Sc.

Honours and Awards:

Outstanding presentation in graduate symposium award
Western University
2016

Province of Ontario Graduate Scholarship
2014-2015, 2015-2016

Canadian Institute of Health Research (CIHR) strategic training fellowship in vascular research
2013-2014, 2014-2015

Graduate Research Scholarship
Western University
2012-2013, 2013-2014

Graduate Research Scholarship
University of South Florida
1998-1999

Related Work Experience

Principal Software Engineer
Autoliv Electronics (Radar systems)
2002-2012

Principal Software Engineer
Lucent Technologies (Core routers)
2000-2002

Senior Software Engineer
Intersil Semiconductors
1998-2000

Refereed Publications:

Omar Mansour, Tamie L. Poepping and James C. Lacefield, "Spread-Spectrum Beamforming and Clutter Filtering for Plane-Wave Color Doppler Imaging," *IEEE Transactions on Ultrasonics, Ferroelectrics, and Frequency Control,* vol. 63, no. 11, pp. 1865 - 1877, 2016.

Omar Mansour, Tamie L. Poepping, and James C. Lacefield (2016), "A beamforming method for plane-wave Doppler imaging of high flow velocities", *SPIE medical imaging symposium 2016*, August, 2015, paper no. 9790-90

Omar Mansour and Michael Paradie (2007), "An Active Phase-Shifting Technique for Estimating I/Q Imbalance using Radar Target Returns, " *M/A-COM Engineering Conference*, session G, p.1:13.